

國立臺灣大學 理學院物理學研究所

碩士學位論文

Graduate Institute of Physics

College of Science

National Taiwan University

Master Thesis

在KOTO實驗中尋找無質量暗光子： $K_L^0 \rightarrow \gamma\bar{\gamma}$

Search for a massless dark photon in  $K_L^0 \rightarrow \gamma\bar{\gamma}$  at the  
KOTO Experiment

吳桐

Tong Wu

指導教授：熊怡 教授

Advisor: Yee Bob Hsiung, Ph.D.

中華民國113年8月

August 2024



NATIONAL TAIWAN UNIVERSITY

MASTER THESIS

---

**Search for a massless dark photon in  
 $K_L^0 \rightarrow \gamma\bar{\gamma}$  at the KOTO Experiment**

---

*Author:*

Tong Wu

*Supervisor:*

Dr. Yee Bob HSIUNG



August 6, 2024

© 2024, by Tong Wu  
tong@hep1.phys.ntu.edu.tw



ALL RIGHTS RESERVED





# Acknowledgements

First and foremost, I would like to express my profound gratitude to my advisor, Professor Yee Bob Hsiung. His guidance was indispensable in the completion of this thesis. His deep expertise and extensive research experience have enriched my studies and my writing immensely. It was his encouragement that propelled me to graduation. I am deeply appreciative of the time and effort he invested in guiding my research and writing, as well as for providing me with invaluable opportunities to participate in international conferences. These experiences significantly enhanced my ability to engage with international physicists. I am grateful for his guidance and support throughout these years.

I also extend my thanks to my thesis committee members, Professors Guey-Lin Lin, Rong-Shyang Lu, Kai-Feng Chen, and Paganis. Their insightful suggestions greatly improved my thesis, and I am thankful for their guidance and advice.

In my research, I am indebted to Yu-Chen Tung, who provided substantial assistance and valuable advice during my data analysis. His support was crucial in helping me overcome the challenges I encountered, enabling me to complete my research successfully. I am also thankful to my senior colleague Chieh Lin (Jay), whose support was instrumental when I first joined the laboratory. He helped me quickly adapt to the lab environment and provided extensive advice and assistance with analysis and programming. Without their help and support, my master's life would have been much more painful.

I would like to thank all the members of the KOTO collaboration for their support and encouragement. Working with such a talented and dedicated group has been a privilege. Special thanks to Koji Shiomi, Tadashi Nomura, Hajime Nanjo, Taku Yamanaka, and Yau W. Wah for their advice and feedback on my analysis. Additionally, I enjoyed the trip to ICHEP 2024 in Prague with Joseph Redeker, Mario Gonzalez, Keita Ono, and Xiang-Chen Li. I am also grateful to the KOTO members and the J-PARC staff for their help and support during the challenging times of the COVID-19 pandemic when I was stranded in Japan.

I am fortunate to have been a part of the NTU High Energy Physics group, where I not only advanced my academic career but also formed lasting friendships. I am grateful to my friends from various experiments who shared countless hours with me in the lab, enriching my research experience and providing much-needed support. Special thanks go to my peers who studied under the same supervisor: Po-An Chen, Yu-Chin Cheng, and Yi-Ting Su. Your camaraderie and shared insights have been invaluable throughout

my journey. I would also like to acknowledge Yu-Wei Kao, Lin Shih, and Pu-Sheng Chen. Our time playing PlayStation and Switch in room 306 brought much-needed relaxation and fun, creating fond memories I will cherish. Gratitude is also extended to You-Ying Li, Xing-Fu Su, Lian-Sheng Tsai, Yi-An Chen, Zheng-Gang Chen, Chin Zhe Tee, Bo-Fu Chen, Hong-Yi Xie, and Bing-Ling Du. The moments we spent together in rooms 306 and 922 were filled with both serious discussions and lighthearted breaks, all of which contributed greatly to my time at NTU. Lastly, I cannot forget my undergraduate colleagues Chin-Hao Chang, Hong-Yi Yang, Link Liu, Roger Li, and Yi-Hao Zhuang. Even though they sometimes traveled to Taipei, their visits were always a highlight, bringing joy and a sense of home to my life here.

Finally, I am profoundly grateful to my parents Bo Wu and Lan Zhang, for their unwavering support, patience, and understanding throughout my academic pursuits. This accomplishment would not have been possible without them.

## 中文摘要

本論文展示了在J-PARC KOTO實驗中尋找質量為零的暗光子 ( $\bar{\gamma}$ ) 於  $K_L^0 \rightarrow \gamma\bar{\gamma}$  衰變的研究，此研究基於2020年特殊運行數據所收集的數據。

與有質量的暗光子不同，質量為零的暗光子不會直接與普通光子混合，但可以通過直接與夸克耦合來與標準模型 (SM) 粒子互動。一些理論模型提出  $K_L^0 \rightarrow \gamma\bar{\gamma}$  衰變的分支比 ( $BR$ ) 可能達到  $\mathcal{O}(10^{-3})$ 。

在特殊運行中收集的  $K_L^0$  衰變數量估計為  $(1.29 \pm 0.02) \times 10^{10}$ 。單一事件的靈敏度計算為  $(2.91 \pm 0.02_{stat.} \pm 0.30_{syst.}) \times 10^{-8}$ 。總背景水平的預測為  $(12.66 \pm 4.42_{stat.} \pm 2.13_{syst.})$ ，並與邊帶區域的數據相符。我們揭開了盲區並觀測到13個事件。使用Feldman-Cousins方法計算  $K_L^0 \rightarrow \gamma\bar{\gamma}$  衰變的分支比上限為  $< 3.47 \times 10^{-7}$  (90%C.L.)。

關鍵詞：暗光子、超越標準模型。



# Abstract

This thesis presents the search for the massless dark photon ( $\bar{\gamma}$ ) in the  $K_L^0 \rightarrow \gamma\bar{\gamma}$  decay at the J-PARC KOTO experiment, based on the special run data collected in 2020.

Distinguished from the massive dark photon, the massless one does not directly mix with the ordinary photon but could interact with Standard Model (SM) particles through direct coupling to quarks. Some theoretical models propose that the branching ratio ( $\mathcal{BR}$ ) of the  $K_L^0 \rightarrow \gamma\bar{\gamma}$  decay could reach up to  $\mathcal{O}(10^{-3})$ .

The number of  $K_L^0$  decays that had been collected in the special run is estimated to be  $(1.29 \pm 0.02) \times 10^{10}$ . The single event sensitivity is calculated to be  $(2.91 \pm 0.02_{stat.} \pm 0.30_{syst.}) \times 10^{-8}$ . The total background level prediction is  $(12.66 \pm 4.42_{stat.} \pm 2.13_{syst.})$  with the agreement from the side-band region. We uncovered the blind region and observed 13 events. The Feldman-Cousins method is used to calculate the upper limit of the  $K_L^0 \rightarrow \gamma\bar{\gamma}$  branching ratio to be  $< 3.47 \times 10^{-7}$ (90%C.L.).

**Keywords:** Dark Photon, beyond Standard Model.



# Contents

<b>Approval</b>	<b>i</b>
<b>Acknowledgements</b>	<b>iii</b>
中文摘要	v
<b>Abstract</b>	<b>vii</b>
<b>Contents</b>	<b>ix</b>
<b>List of Figures</b>	<b>xi</b>
<b>List of Tables</b>	<b>xv</b>
<b>1 Introduction</b>	<b>1</b>
1.1 Dark Matter and Dark Photons . . . . .	1
1.2 Theoretical Predictions . . . . .	1
1.3 Basic Strategy of the $K_L^0 \rightarrow \gamma\bar{\gamma}$ Search . . . . .	2
1.3.1 Signal Identification . . . . .	2
1.3.2 Major Background Sources . . . . .	3
1.4 Thesis Overview . . . . .	4
<b>2 KOTO Experiment</b>	<b>5</b>
2.1 J-PARC and Proton Beamline . . . . .	5
2.2 $K_L^0$ Beamline . . . . .	6
2.3 Detectors . . . . .	7
2.3.1 CsI . . . . .	8
2.3.2 Charge Veto Counter . . . . .	10
2.3.3 Barrel Veto Counter . . . . .	10
2.4 Data Acquisition System . . . . .	12
<b>3 Event Reconstruction</b>	<b>13</b>
3.1 Photon Cluster Finding . . . . .	13
3.2 Reconstruction of $\pi^0$ . . . . .	15
3.3 Reconstruction of Decays . . . . .	16
3.3.1 Reconstruction of $K_L^0 \rightarrow 3\pi^0$ . . . . .	17
3.3.2 Reconstruction of $K_L^0 \rightarrow \gamma\bar{\gamma}$ . . . . .	18
3.3.3 Correction for Energy and Position of Photon Clusters . . . . .	18
3.4 Veto Hit Reconstruction . . . . .	20
3.4.1 Barrel Veto Counters . . . . .	21

3.4.2	CsI Calorimeter . . . . .	22
<b>4</b>	<b>Monte Carlo Simulation</b>	<b>25</b>
4.1	GEANT4 toolkit . . . . .	25
4.2	Detector Response . . . . .	26
4.3	Pulse Simulation . . . . .	26
4.4	$K_L^0$ Generation . . . . .	26
4.4.1	Beamline Simulation . . . . .	26
4.4.2	Empirical $K_L^0$ Spectrum Simulation . . . . .	27
4.5	Fast Simulation . . . . .	28
4.6	Accidental Overlay . . . . .	29
4.7	Neutron background Simulation . . . . .	30
<b>5</b>	<b><math>K_L^0</math> Yield Estimation</b>	<b>31</b>
5.1	Data Set . . . . .	31
5.2	Event Selections . . . . .	32
5.2.1	Trigger Cut . . . . .	32
5.2.2	Photon Selection . . . . .	32
5.2.3	$K_L^0$ Selection . . . . .	34
5.2.4	Veto Cut . . . . .	36
5.3	Yield Estimation . . . . .	37
5.3.1	Estimation by $K_L^0 \rightarrow 3\pi^0$ Decays . . . . .	38
5.4	Summary of $K_L^0$ Yield Estimation . . . . .	38
<b>6</b>	<b>Analysis of <math>K_L \rightarrow \gamma\bar{\gamma}</math></b>	<b>43</b>
6.1	Data Set . . . . .	44
6.2	Single Cluster Event Selection . . . . .	45
6.2.1	Trigger Selection . . . . .	45
6.2.2	Kinematic Cuts . . . . .	46
6.2.3	Veto Cuts . . . . .	47
6.3	Background Suppression . . . . .	49
6.3.1	$K_L$ Decay Background . . . . .	49
6.3.2	Neutron Background . . . . .	52
6.4	Single Event Sensitivity . . . . .	58
6.4.1	Systematic Uncertainty of SES . . . . .	58
6.5	Additional Background Source Study . . . . .	58
6.6	Background Level Estimation . . . . .	63
6.7	Unbind the Signal Region . . . . .	64
<b>7</b>	<b>Conclusion and Discussion</b>	<b>67</b>
7.1	Discussion for Next Step . . . . .	68
7.2	Massive Dark Photon Search . . . . .	68
<b>Bibliography</b>		<b>69</b>

# List of Figures

1.1 A schematic diagram of the CsI and an event of $K_L^0 \rightarrow \gamma\bar{\gamma}$ decay . . . . .	3
2.1 The entire view of J-PARC. [5] . . . . .	5
2.2 Illustration of the Hadron Experimental Facility (HEF) at J-PARC.[9] The KL in the Figure indicated the KOTO detector . . . . .	6
2.3 Structural drawings of the T1 production target [10]. One bar is used for production and the other is a spare. . . . .	7
2.4 Schematic diagram of the $K_L^0$ beamline.[11] . . . . .	7
2.5 Beamline layout . . . . .	8
2.6 Schematic diagram of CsI layout. . . . .	9
2.7 KOTO detector layout . . . . .	10
2.8 The Schematic Diagram of Charge Veto Structure. . . . .	11
2.9 The Schematic Diagram of Barrel Veto Structure. Figure courtesy of [15]. . . . .	11
2.10 The architecture of the KOTO DAQ system. [16] . . . . .	12
3.1 The illustration of the cluster finding process. All the color crystals are the seed crystals, and the crystals with the same color belong to the same cluster. The black crystal is the isolated crystal hit. . . . .	14
3.2 Timing boundary for a cluster seed based on the scattered plot of crystal timing versus energy deposit. A Gaussian function is fitted at each energy bin and the boundary is defined by $\mu \pm 5\sigma$ , where $\mu$ and $\sigma$ are the Gaussian mean and standard deviation. The orange points indicate the boundary at the associated energy bin. The red curve connects all the points for the interpolation of the boundary value between the points. (Figure courtesy of [15]) . . . . .	15
3.3 The schematic diagram of the $\pi^0 \rightarrow 2\gamma$ decay process. . . . .	16
3.4 The schematic diagram of the $K_L^0$ travel and decay process and geometry relationships . . . . .	18
3.5 The schematic diagram of the correction of the photon cluster position. . . . .	19
3.6 Schematic view of the timings used in the module-veto-timing calculation. . . . .	21
3.7 The Schematic diagram of a photon hit with the generated scintillation lights propagating to both directions and captured by PMTs. Figure courtesy of [15] . . . . .	22
3.8 The Schematic diagram of geometry relationships of the Barrel veto counter.	22

4.1	Beam content at the KOTO detector entrance based on the beamline simulation. Figure courtesy of [15] . . . . .	27
4.2	The $K_L^0$ momentum spectrum at the exit of the second collimator. Figure courtesy of [15] . . . . .	28
4.3	Comparison of $K_L^0$ beam profile at the exit of the second collimator between the beamline simulation and the empirical model. Figure courtesy of [15] . . . . .	28
4.4	An example of the accidental overlay on a simulated pulse, subtracting the pedestal. Figure courtesy of [15] . . . . .	30
5.1	Distribution of the photon selection variables for the $K_L^0 \rightarrow 3\pi^0$ decay. The photon selection cuts are applied except for the variable shown in the plot. The black point shows the data, and the fill histogram shows the Monte Carlo simulation. The red arrow indicates the cut-off value of the variable.	33
5.2	Distribution of the $K_L^0$ selection variables for the $K_L^0 \rightarrow 3\pi^0$ decay. The photon and $K_L^0$ selection cuts are applied except for the variable shown in the plot. The black point shows the data, and the fill histogram shows the Monte Carlo simulation. The red arrow indicates the cut-off value of the variable.	34
5.3	Distribution of the $K_L^0$ selection variables for the $K_L^0 \rightarrow 3\pi^0$ decay. The photon and $K_L^0$ selection cuts are applied except for the variable shown in the plot. The black point shows the data, and the fill histogram shows the Monte Carlo simulation. The red arrow indicates the cut-off value of the variable.	35
5.4	Distribution of isolated crystal hit energy(E) vs. its distance(D) from the nearest cluster. The red line shows the cut based on Equation 5.2. The sample was obtained from the $K_L^0 \rightarrow \pi^0\nu\bar{\nu}$ Monte Carlo simulation.[23]	38
5.5	Beam profile at the exit of the second collimator via the $K_L^0 \rightarrow 3\pi^0$ decay analysis. All the selection cuts are imposed. Filled histograms are predicted by the Monte Carlo simulation.	39
5.6	Distribution of the kinematic variables for the $K_L^0 \rightarrow 3\pi^0$ decay. All the selections are applied except the variable shown in the plot. The black point shows the data, and the fill histogram shows the Monte Carlo simulation. The red arrow indicates the cut-off value of the variable.	40
5.7	Distribution of the kinematic variables for the $K_L^0 \rightarrow 3\pi^0$ decay. All the selections are applied except the variable shown in the plot. The black point shows the data, and the fill histogram shows the Monte Carlo simulation. The red arrow indicates the cut-off value of the variable.	41
6.1	The mechanism of the 2-cluster neutron event in the Z0 run.	45

6.2	Distribution of cluster timing after relative timing correction. The dot is from real physics data, and the filled histogram is the MC simulation. The red arrow is the cut-off region. . . . .	46
6.3	Distribution of total energy from Monte Carlo simulation. The histogram area is normalized to 1. The red arrow is the cut-off region. . . . .	46
6.4	An upstream view of the CsI calorimeter. The red region is the outermost boundary, while the blue region is the innermost boundary. . . . .	47
6.5	Distribution of veto timing of CC06. . . . .	48
6.6	Temporary plots of FBAR and NCC . . . . .	50
6.7	The schematic geometry diagram of the mechanism of the upstream decay background. . . . .	51
6.8	$E_\gamma - H_{XY}$ distributions of scattered $K_L^0 \rightarrow 2\gamma$ decays with various cut. The red frame indicates the signal region. The red number indicates the background level in each region. . . . .	51
6.9	The schematic geometry diagram of the mechanism of the fusion cluster background. . . . .	52
6.10	$E_\gamma - H_{XY}$ distributions of various background sources after applying all selection cuts. Left-hand side plots exclude the neutron cuts and the right-hand side plots include it. The red frame indicates the signal region. The red number indicates the background level in each region. (Region A indicates the Signal Region and Region B indicates the Blind Region excluding the signal region.) . . . . .	53
6.11	Example of the energy and timing shapes of photon cluster from the Monte Carlo simulation and neutron cluster from data. The color code represents the deposited energy in MeV and the timing in nanoseconds for each crystal in the cluster. [24] . . . . .	54
6.12	The architecture of CSD neural network training process. . . . .	55
6.13	The ROC curve of the training model. The x-axis is the photon acceptance, and the y-axis is the neutron rejection. . . . .	56
6.14	Average pulse shape of the neutron sample (blue dots) and photon sample (red dots) from one CsI crystal.[24] . . . . .	56
6.15	Distribution of the likelihood ratio for hadronic cluster events (red) and photon cluster events (blue). The photon cluster events are obtained through the $K_L^0 \rightarrow 3\pi^0$ decay analysis of data. The neutron sample is obtained from neutron data. . . . .	57
6.16	Illustration of shower depth means. An MPPC is installed on the upstream side. The time difference between the photon arriving upstream and downstream ( $\Delta T = T_{MPPC} - T_{PMT}$ ) is used to measure the depth of the reaction and distinguish between photon events (up) and neutron events (down). . . . .	57

6.17 Distribution of the $\Delta T$ for neutron events and photon events. The photon cluster events are obtained through the $K_L^0 \rightarrow 3\pi^0$ decay analysis of data. The neutron sample is obtained by scattering neutrons in the beam with an Al plate. . . . .	58
6.18 The $H_{XY}$ distribution of the region 2. The red line and arrow indicated the cutoff region . . . . .	59
6.19 The schematic geometry diagram of the mechanism of the very upstream decay from the 2nd collimator. . . . .	60
6.20 $E_\gamma - H_{XY}$ distributions of $K_L^0 \rightarrow 2\gamma$ and $K_L^0 \rightarrow 3\pi^0$ decays after applying all selection cuts except $H_{XY} > 175$ . Left-hand side plots decay at $z=-1507$ mm and the right-hand side plots decay at $z=-5507$ mm. . . . .	61
6.21 A schematic diagram of the mechanism of the NCC background. . . . .	61
6.22 $P_T - z_{vtx}$ distribution of the NCC background with $K_L^0 \rightarrow \pi^0\nu\bar{\nu}$ reconstruction. The left plot is from the data the right plot is the MC of the NCC background. The red frame indicates the NCC region. . . . .	62
6.23 $E_\gamma - H_{XY}$ distribution of the NCC background after applying all selection cuts. . . . .	62
6.24 $E_\gamma - H_{XY}$ distribution of the charge Kaon decay after applying all selection cuts. . . . .	63
6.25 Event display of the charge Kaon decay. . . . .	63
6.26 $E_\gamma - H_{XY}$ distribution of physics data after applying all the selection cuts. The black box is the blind region the red frame is the signal region. The black (red) number is the observed (expected) number of events. . . . .	64
6.27 $E_\gamma - H_{XY}$ distribution of physics data after open the blind box. The black (red) number is the observed (expected) number of events. . . . .	65
7.1 Upper limit (left) and signal acceptance (right) for each mass dark photon from 0 MeV to 250 MeV . . . . .	68

# List of Tables

1.1	Theoretical predictions for the branching fractions of the Kaon decays involving massless dark photons. [3] . . . . .	2
1.2	Main $K_L^0$ decay background modes and their branching ratios. . . . .	4
5.1	Branching ratio of $K_L$ decays . . . . .	31
5.2	Summary of the veto cut . . . . .	37
6.1	Summary of Systematic Uncertainty for SES . . . . .	59
6.2	Geometry calculation of the maximum $H_{XY}$ of the cluster of the upstream decay background . . . . .	60
6.3	Background Level predicted for each source inside the signal region . . .	64



# <sup>1</sup> Chapter 1

## <sup>2</sup> Introduction

### <sup>3</sup> 1.1 Dark Matter and Dark Photons

<sup>4</sup> Dark matter (DM) is posited to constitute approximately 26.4% of the universe's critical  
<sup>5</sup> density, according to cosmological observations [1]. At this moment the fundamental na-  
<sup>6</sup> ture of dark matter remains one of the most profound mysteries in physics. The Standard  
<sup>7</sup> Model (SM) of particle physics provides no viable explanation for dark matter, prompt-  
<sup>8</sup> ing the motivation to explore physics beyond the Standard Model (BSM). Recent years  
<sup>9</sup> have seen a surge in research aimed at probing the dark sector, with numerous astrophys-  
<sup>10</sup> ical and high-energy physics (HEP) experiments making intensified efforts to explore the  
<sup>11</sup> dark matter.

<sup>12</sup> The dark photon is one of the most promising candidates in the dark sector, it is a new  
<sup>13</sup> type of gauge boson. Theoretically, there are two kinds of dark photons, the massive dark  
<sup>14</sup> photon and the massless dark photon. The massive dark photon ( $A'$ ) could mix coupling  
<sup>15</sup> with visible photons, to interact with the ordinary particles [1], which means the massive  
<sup>16</sup> dark photon is possible to be detected in the experiments. Consequently, the massive  
<sup>17</sup> dark photon gets most of the attention in the experimental search for dark photons [2].  
<sup>18</sup> However, the massive dark photon has been searched by several experiments, and no  
<sup>19</sup> evidence has been observed so far, the parameter space for the massive dark photon  
<sup>20</sup> has been increasingly constrained. Therefore, our investigation shifts focus towards the  
<sup>21</sup> search for the massless dark photon.

<sup>22</sup> The massless dark photon, denoted as  $\bar{\gamma}$  in this thesis, is different from the massive  
<sup>23</sup> dark photon, it will not directly couple with the Standard Model(SM) particles, and only  
<sup>24</sup> interact with the SM particles by coupling to the quark. [2] Therefore the massless dark  
<sup>25</sup> photon is more challenging to be searched in the experiments because it is undetectable.

### <sup>26</sup> 1.2 Theoretical Predictions

<sup>27</sup> There are some theoretical calculations predict that the existence of massless dark pho-  
<sup>28</sup> tons in the Kaon decay [3]. Assuming the flavor-changing neutral current (FCNC) cou-  
<sup>29</sup> pling to the  $d$  and  $s$  quarks, the Kaon meson can decay with missing energy by a massless  
<sup>30</sup> dark photon. The theories consider the neutral Kaon decay and the charge Kaon channels  
<sup>31</sup> shown in the below Table 1.1.

TABLE 1.1: Theoretical predictions for the branching fractions of the Kaon decays involving massless dark photons. [3]

Decay Channel	Branching Fraction
$K_L \rightarrow \gamma\bar{\gamma}$	$< 1.2 \times 10^{-3}$
$K_S \rightarrow \gamma\bar{\gamma}$	$< 2.1 \times 10^{-6}$
$K_L \rightarrow \pi^0\gamma\bar{\gamma}$	$< 1.0 \times 10^{-6}$
$K_S \rightarrow \pi^0\gamma\bar{\gamma}$	$< 1.8 \times 10^{-9}$
$K_L \rightarrow \pi^+\pi^-\bar{\gamma}$	$< 9.8 \times 10^{-6}$
$K_S \rightarrow \pi^+\pi^-\bar{\gamma}$	$< 1.7 \times 10^{-8}$
$K^+ \rightarrow \pi^+\gamma\bar{\gamma}$	$< 5.6 \times 10^{-7}$
$K^+ \rightarrow \pi^+\pi^0\bar{\gamma}$	$< 2.4 \times 10^{-6}$

Some decay channels in  $K_L^0$  decay can potentially be searched in the KOTO experiment. KOTO Experiment is a rare kaon decay experiment, it is designed to search for the  $K_L^0 \rightarrow \pi^0\nu\bar{\nu}$  decay, which is a rare long-lived neutral kaon decay that can provide valuable insights into the CP violation in the Standard Model.  $K_L^0 \rightarrow \pi^0\nu\bar{\nu}$  decay has neutrinos in the final state, which become missing energy in the detector because it is undetectable. To probe the missing energy of the neutrino pair, a hermetic veto system was designed to enclose the kaon decay volume. This design can avoid the energy missing from the detectable particle as much as possible, which is beneficial to the search for the missing energy decay channel.

### 1.3 Basic Strategy of the $K_L^0 \rightarrow \gamma\bar{\gamma}$ Search

From the theoretical perspective shown above, the massless dark photon can be produced in the  $K_L^0 \rightarrow \gamma\bar{\gamma}$  decay with the branching fraction of this model up to  $10^{-3}$ . This is well within the sensitivity of the KOTO experiment and is the search Objective of this thesis.

In the  $K_L^0 \rightarrow \gamma\bar{\gamma}$  decay, the final state is a photon and a massless dark photon, the photon is detectable in the detector, and the massless dark photon is undetectable.

#### 1.3.1 Signal Identification

The decay  $K_L^0 \rightarrow \gamma\bar{\gamma}$  necessitates that only a single photon cluster strikes the CsI calorimeter, with no concurrent hits elsewhere in the detector. Such a single cluster yields solely energy and position data, presenting a significant analytical challenge due to the absence of additional kinematic constraints. Furthermore, the simplicity of single cluster events makes them susceptible to mimicry by unidentified backgrounds. To mitigate this, imposing stringent requirements on both the energy of the photon  $E_\gamma$  and its position radius  $H_{XY}$  on the CsI can effectively reduce background interference from accidental hits.

To mitigate potential biases in evaluating event candidates, a blind analysis strategy is implemented. A "blind region" is delineated on the reconstructed  $(E_\gamma - H_{XY})$  plane, as depicted in Figure 1.1. Within this blind region, a signal box is established, which is

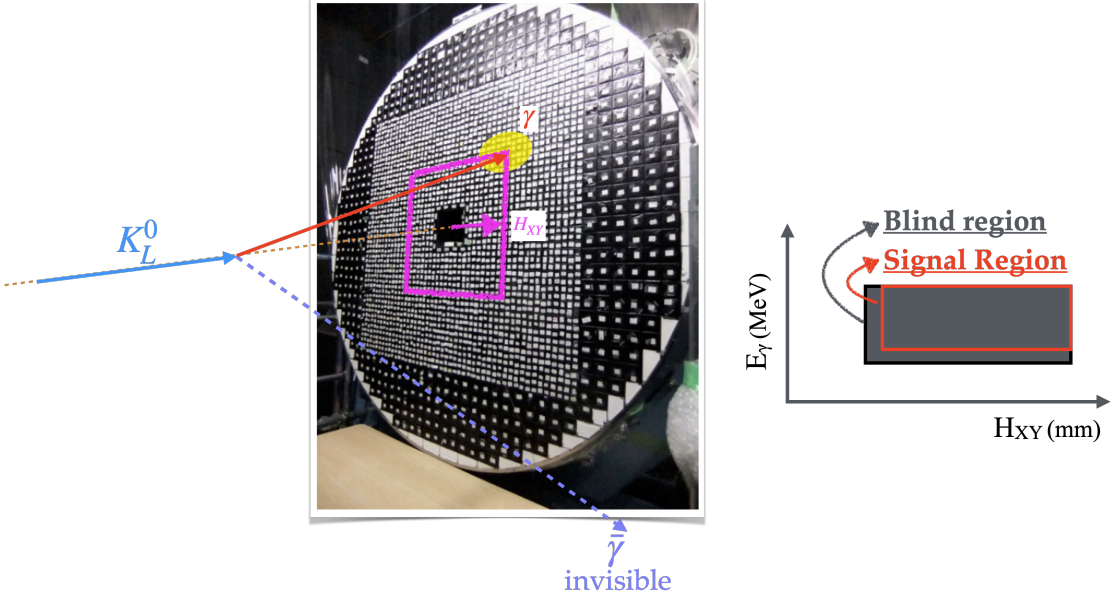


FIGURE 1.1: A schematic diagram of the CsI and an event of  $K_L^0 \rightarrow \gamma\bar{\gamma}$  decay.

58 optimized based on the background-to-signal ratio as predicted by simulations. Only  
 59 events that fall within this signal box are considered viable signal event candidates. The  
 60 side-band region, adjacent to the signal box, serves to model the expected event distribu-  
 61 tion within the signal region. Comprehensive analysis and understanding of the data's  
 62 characteristics are prerequisites before accessing the events in the blind region, a process  
 63 referred to as "unblinding" or "opening the box."

#### 64 1.3.2 Major Background Sources

65 The major background sources are  $K_L^0$  decay background and neutron-like background.

##### 66 $K_L^0$ decay background

67 Table 1.2 shows the main  $K_L^0$  decay backgrounds. Other decay channels are unneces-  
 68 sary to be considered because of the low branching ratio. Only  $K_L^0 \rightarrow \pi^\pm e^\mp \nu_e$  and  
 69  $K_L^0 \rightarrow \pi^\pm \mu^\mp \nu_\mu$  are considered for the decay channel of charged particles in the final  
 70 state, due to the high branching ratio. To suppress the  $K_L^0$  decay background, study-  
 71 ing these decay channels and understanding their characteristics are important. All of  
 72 these decay channels produce more than one photon in the final state. Therefore, it is  
 73 easy to suppress these decay channels with the KOTO detector. Except for the decay of  
 74  $K_L^0 \rightarrow 2\gamma$ , whose final state is similar to the signal signature and may be a potentially  
 75 non-eliminable source of background.

##### 76 Neutron-like background

77 The neutron originating from the beamline poses a significant background challenge.  
 78 Accurately simulating the in-beam neutron background is nearly impossible, especially

TABLE 1.2: Main  $K_L^0$  decay background modes and their branching ratios.

Decay mode	Branching Ratio
$K_L \rightarrow \pi^\pm e^\mp \nu_e$	$(40.55 \pm 0.11)\%$
$K_L \rightarrow \pi^\pm \mu^\mp \nu_\mu$	$(27.04 \pm 0.07)\%$
$K_L \rightarrow 3\pi^0$	$(19.52 \pm 0.12)\%$
$K_L \rightarrow \pi^+ \pi^- \pi^0$	$(12.54 \pm 0.05)\%$
$K_L \rightarrow 2\pi^0$	$(8.64 \pm 0.06) \times 10^{-4}$
$K_L \rightarrow 2\gamma$	$(5.47 \pm 0.04) \times 10^{-4}$

<sup>79</sup> without a defined mechanism to avoid it. The primary method to mitigate this back-  
<sup>80</sup> ground involves distinguishing the cluster from the photon event.

## <sup>81</sup> 1.4 Thesis Overview

<sup>82</sup> This thesis presents a detailed study of the  $K_L^0 \rightarrow \gamma\bar{\gamma}$  decay in the KOTO experiment.  
<sup>83</sup> We begin with an overview of the KOTO experiment, describing its detector components  
<sup>84</sup> and data acquisition (DAQ) system. The analysis section follows, where we elucidate  
<sup>85</sup> the event reconstruction methods and Monte Carlo simulation techniques employed in  
<sup>86</sup> the KOTO experiment. Special attention is given to the unique approaches developed  
<sup>87</sup> for this particular analysis. Subsequently, we delve into the crucial process of Kaon yield  
<sup>88</sup> estimation and provide an in-depth exploration of the  $K_L^0 \rightarrow \gamma\bar{\gamma}$  analysis. This includes  
<sup>89</sup> background estimation and systematic uncertainty evaluation. In conclusion, we sum-  
<sup>90</sup> marize our findings and discuss their implications. The thesis culminates with an out-  
<sup>91</sup> look on the prospects of the  $K_L^0 \rightarrow \gamma\bar{\gamma}$  search within the KOTO experiment, considering  
<sup>92</sup> potential improvements and challenges.

<sup>93</sup> **Chapter 2**

<sup>94</sup> **KOTO Experiment**

<sup>95</sup> The KOTO Experiment is a rare decay experiment. The main goal of this experiment is  
<sup>96</sup> to search for the  $K_L \rightarrow \pi^0 \nu \bar{\nu}$  decay. The branching ratio of this decay is predicted to be  
<sup>97</sup>  $(3.00 \pm 0.30) \times 10^{-11}$  by the Standard Model (SM) [4]. The branching ratio of this decay  
<sup>98</sup> is sensitive to the new physics beyond the SM because of the accuracy. Therefore, the  
<sup>99</sup> KOTO experiment is a good place to search for new physics.

<sup>100</sup> This chapter will introduce the KOTO detector, outlining the sequence from proton  
<sup>101</sup> generation through to data capture within the detector.

<sup>102</sup> **2.1 J-PARC and Proton Beamlne**

<sup>103</sup> The KOTO experiment is located at the Japan Proton Accelerator Research Complex (J-  
<sup>104</sup> PARC)[5] Hadron Experimental Facility (HEF) in Tokai, Japan. Figure 2.1 shows the flow  
<sup>105</sup> of proton beam acceleration, HEF (Hadron Beam Facility) is one of the delivered exper-  
<sup>106</sup> iment facilities. The proton beam has been generated at the end of the linear particle  
<sup>107</sup> accelerator (LINAC)[6], then into a 3 GeV rapid cycling synchrotron (RCS)[7], and finally  
<sup>108</sup> into the main ring synchrotron (MR) to accelerate to 30 GeV[8]. At the end extracted from  
<sup>109</sup> the synchrotron and directed to the HEF, as shown in Figure 2.2.

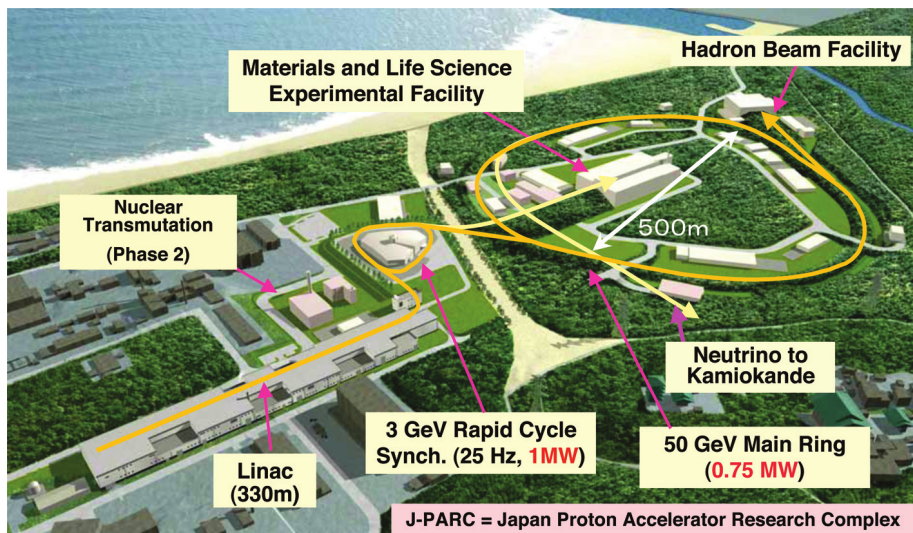


FIGURE 2.1: The entire view of J-PARC. [5]

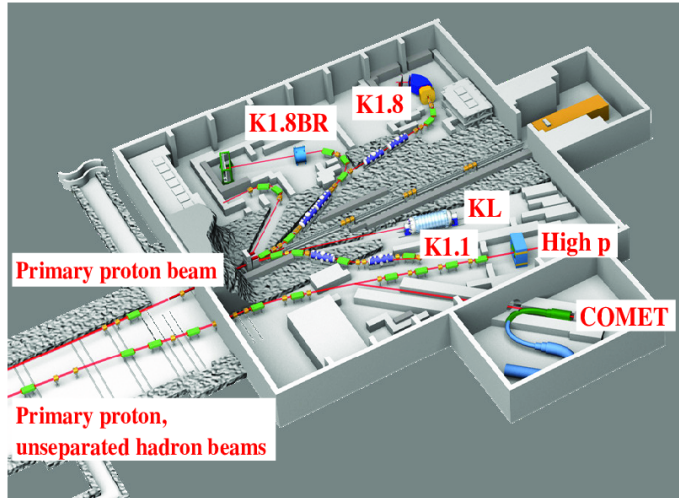


FIGURE 2.2: Illustration of the Hadron Experimental Facility (HEF) at J-PARC.[9] The KL in the Figure indicated the KOTO detector

To reduce the instantaneous rate of particles coming into detectors to prevent the event pileup, a slow-extraction (SX) technique is used. The proton beam was extracted for 2 seconds as a "spill" every 4.22 seconds in 2024 for the beam power of 82 kW. The beam power is calculated by

$$\text{Beam Power} = E_{\text{proton}} F_{\text{proton}}, \quad (2.1)$$

$$F_{\text{proton}} = N_{\text{spill}}^{\text{proton}} / s_{\text{spill}} \quad (2.2)$$

where  $E_{\text{proton}}$  is the extracted energy of the proton beam,  $F_{\text{proton}}$  is the protons flux,  $N_{\text{spill}}^{\text{proton}}$  is the number of protons per spill, and  $s_{\text{spill}}$  is the spill duration.

In HEF, the extracted proton beam collides with the T1 target to produce secondary particles. As shown in Figure 2.3, the T1 target consists of two 66 mm long gold bars with dimensions of  $15 \times 11$  mm in cross-section. One bar is used for production and the other one is a spare. The secondary particles are then directed to the KOTO detector at a  $16^\circ$  to the beamline.

## 2.2 $K_L^0$ Beamline

After the p-gold collides, a  $16^\circ$  to the beamline was chosen to direct the Kaon beamline for KOTO. Figure 2.4 shows the schematic diagram of the  $K_L^0$  beamline. To reduce the photon in the beamline, a 7 cm thick lead photon absorber was installed after the T1 target. Two collimators follow that to narrow the beamline and make it pencil-like. A sweeping magnet with a 1.2 T magnetic field was installed between the two collimators to reduce the charged particles in the beamline. A rotatable beam plug is placed between the sweeping magnet and the 2nd collimator, it is made of brass that could stop the beamline with most particles. The total length of the beamline is 20 m, which is long enough to allow the short-lived particles, such as the  $K_s$  and hyperons, to decay before reaching the KOTO detector. Figure 4.1 shows the possible remaining particle at the end of the

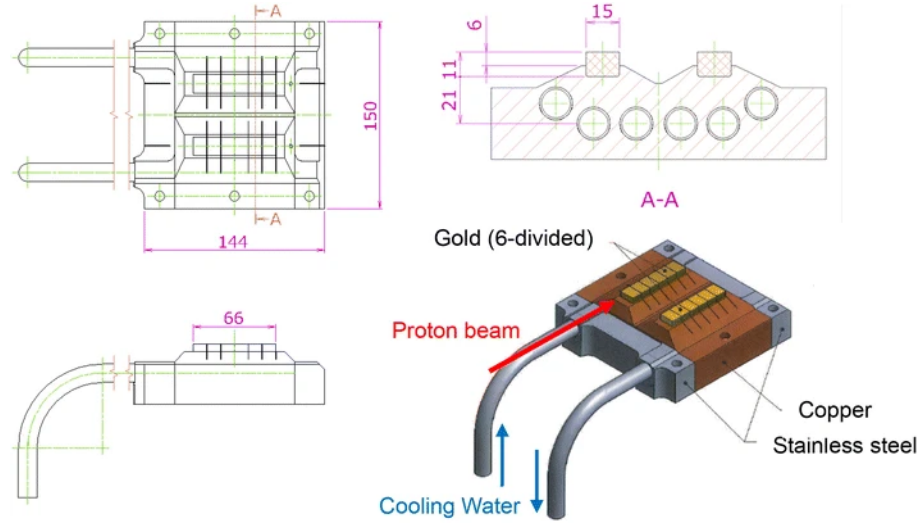


FIGURE 2.3: Structural drawings of the T1 production target [10]. One bar is used for production and the other is a spare.

132 2nd collimator in the beamline which is estimated by the beamline simulation. These  
133 particles will enter the KOTO detector.

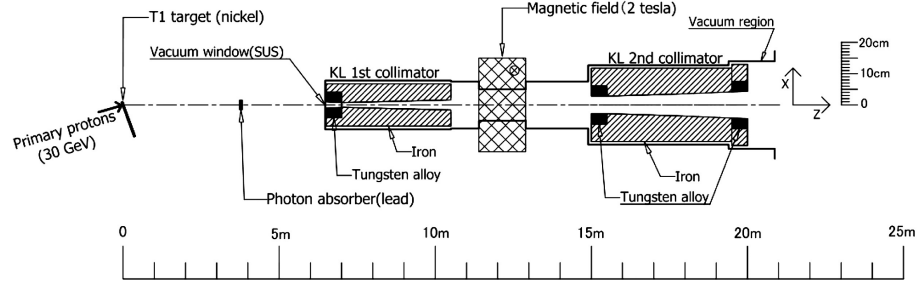


FIGURE 2.4: Schematic diagram of the  $K_L^0$  beamline.[11]

## 134 2.3 Detectors

135 The KOTO detector is designed to study the decay of  $K_L^0$  particles. Its main components  
136 are an electromagnetic calorimeter and a hermetic veto system. As  $K_L^0$  particles enter the  
137 detector, they decay within a highly evacuated volume maintained at  $5 \times 10^{-5}$  Pa. The  
138 resulting decay products are then detected by various subdetectors. The electromagnetic  
139 calorimeter, positioned perpendicular to the beamline, serves primarily as a photon de-  
140 tector. Surrounding the decay volume, the hermetic veto system comprises multiple veto  
141 counters, including barrel vetoes, charge vetoes, and additional specialized veto coun-  
142 ters. This comprehensive veto system ensures efficient detection and differentiation of  
143 particle interactions. Figure 2.7 provides a schematic overview of the KOTO detector's  
144 layout and components. In this section, the Calorimeter and some important veto coun-  
145 ters will be introduced in detail.

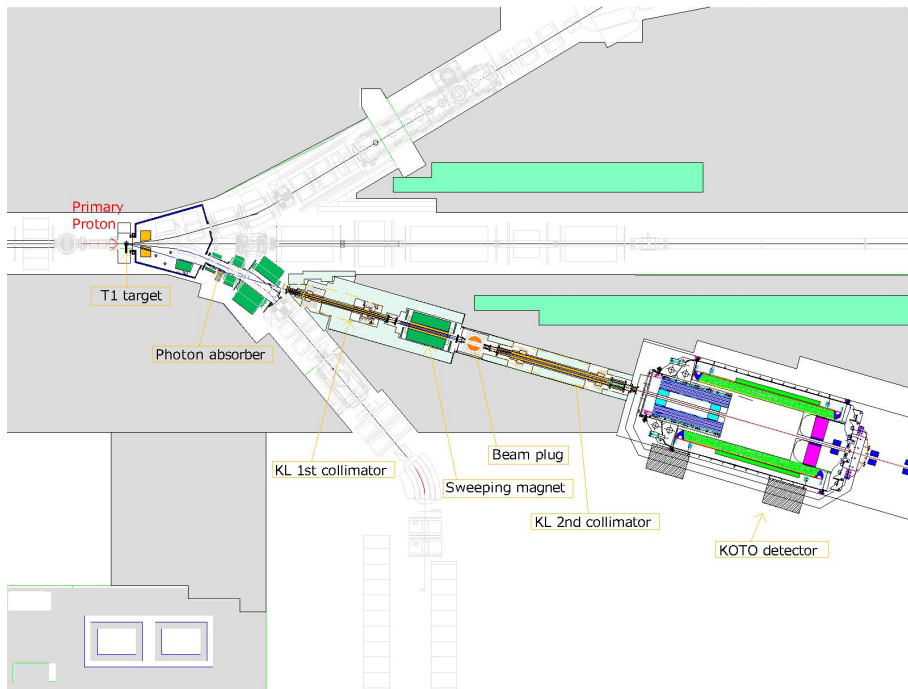


FIGURE 2.5: Beamlne layout

### <sup>146</sup> 2.3.1 CsI

<sup>147</sup> The electromagnetic calorimeter is the main detector of the KOTO experiment. It is used  
<sup>148</sup> to detect the photon from the  $K_L$  decay. The electromagnetic calorimeter consists of 2716  
<sup>149</sup> undoped cesium iodide crystals (CsI). The cross-section of crystals has 2 types of units:  
<sup>150</sup> the small crystal is  $25 \times 25$  mm with 2240 crystals, and the large one is  $50 \times 50$  mm with  
<sup>151</sup> 476 crystals. The arrangement of those crystals is shown in Figure 2.6. The depth of the  
<sup>152</sup> crystal is 500 mm corresponding to 27 radiation lengths( $X_0$ ), in which the  $X_0$  of CsI is  
<sup>153</sup> 18.5 mm. The large crystal depth can contain all the photon energy that can allow us to  
<sup>154</sup> ignore the detection inefficiency of the photon. The small crystal size is smaller than the  
<sup>155</sup> Molère radius of 35.7 mm, which provides a good resolution of position and the cluster  
<sup>156</sup> shape in the x-y plant. That allows us to use the shower shape to distinguish the different  
<sup>157</sup> types of clusters on CsI.

<sup>158</sup> A both-end readout system was used in the CsI calorimeter. A photon multiplier tube  
<sup>159</sup> (PMT) was connected to the end of each CsI crystal. When a photon hits the CsI, the EM  
<sup>160</sup> shower will be induced and the PMT can observe the deposited energy on each crystal.  
<sup>161</sup> In front of the CsI crystal, 4096 Multi-pixel photon counters (MPPC) were glued. It could  
<sup>162</sup> detect the signal of the photon hit from the front end. This readout system can be used to  
<sup>163</sup> measure the shower depth in the calorimeter, by evaluating the time difference between  
<sup>164</sup> both ends of the crystal. Which is potentially useful for discriminating the photon cluster  
<sup>165</sup> and hadronic-like cluster. Because a hadronic shower is generally deeper than an EM  
<sup>166</sup> shower cluster.

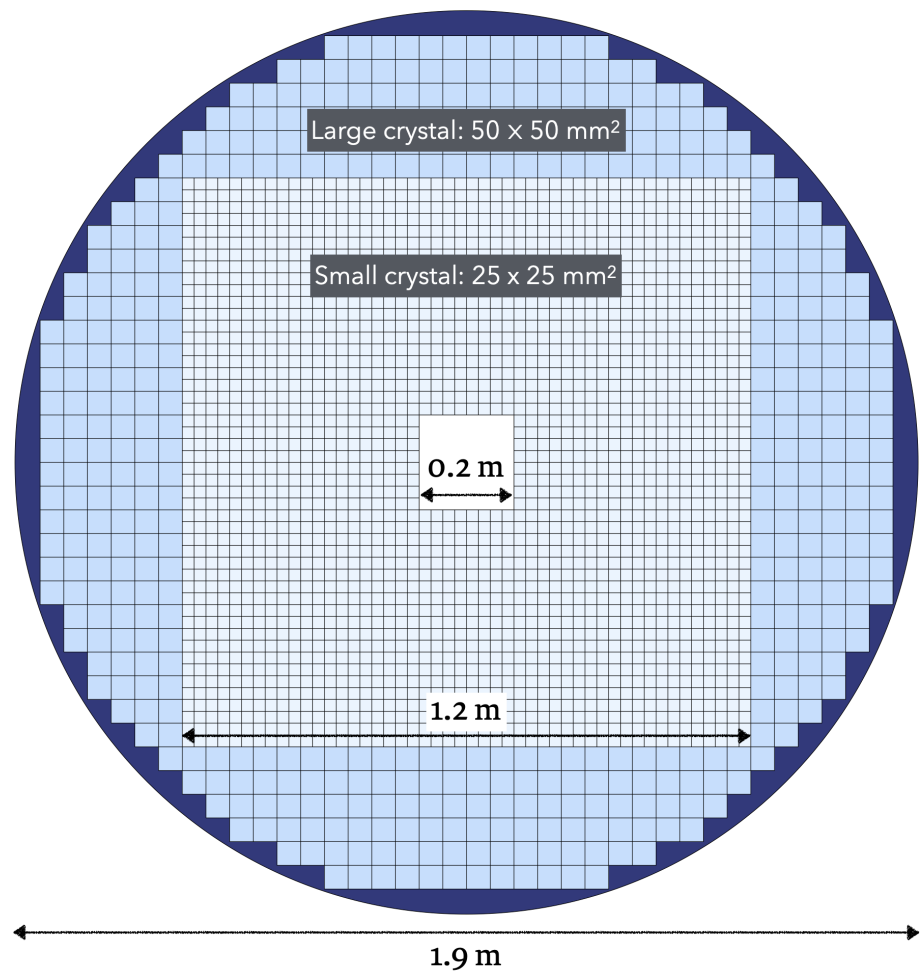


FIGURE 2.6: Schematic diagram of CsI layout.

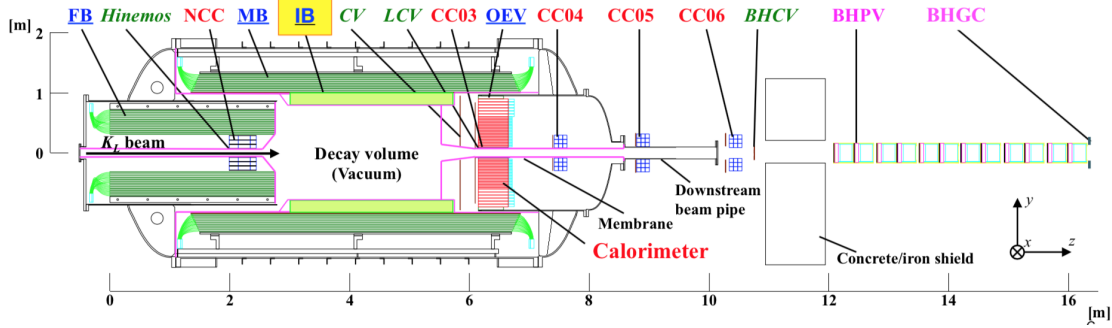


FIGURE 2.7: KOTO detector layout

### 167 2.3.2 Charge Veto Counter

168 The Charge Veto Counter (CV) is placed in front of the CsI [12, 13, 14]. It is a plant com-  
 169 posed of plastic scintillator strips, the arrangement of the strips is shown in Figure 2.8.  
 170 Because the CV plant is also perpendicular to the beamline, a square hole was made in  
 171 the center of the CV to allow the beamline to pass through. The CV consists of two layers  
 172 of 3-mm thick scintillator strips and wavelength-shifting (WLS) fibers, the direction of  
 173 the two layers' strips is perpendicular to each other. The front CV is placed 30 cm up-  
 174 stream of the CsI, and the Rare CV is placed 5 cm upstream. An MPPC was attached to  
 175 both ends of the strip to detect the light emitted by the scintillator.

176 This veto counter was used to detect the charged particle that could hit the CsI calorime-  
 177 ter. Because the  $K_L^0 \rightarrow \pi^\pm e^\mp \nu_e$  and  $K_L^0 \rightarrow \pi^\pm \mu^\mp \nu_\mu$  have a very large branching ratio, the  
 178 charged particle could hit the CsI calorimeter and produce a fake photon cluster. The  
 179 main purpose of the CV is to veto the charged particle and reduce these two decay chan-  
 180 nels. The inefficiency of the CV to a single charge particle is  $1.5 \times 10^{-5}$ .

### 181 2.3.3 Barrel Veto Counter

182 The Barrel veto counters surround the decay volume which is the main body of the her-  
 183 metic veto system to ensure all the photons will not escape from the detector. There are  
 184 3 Barrel Veto Counters in the KOTO detector, Front Barrel(FB), Main Barrel(MB), and In-  
 185 ner Barrel(IB). The place relation of the three barrel veto counters was shown in Figure  
 186 2.9. The MB covered the decay volume, and the IB was placed in the center of the MB,  
 187 these two veto counters are used to detect the photon hit escape from the CsI calorime-  
 188 ter. The front barrel covers the upstream of the decay region to veto the event decay in  
 189 the upstream region. All the barrel veto counters are composed of the lead-scintillator  
 190 sandwich structure, as shown in Figure 2.9. The lead was used to absorb the photon and  
 191 the scintillator was used to emit the light when the photon hit. After the light emitted by  
 192 the scintillator, it will be transferred to the PMT attached to the end of the barrel by WSL  
 193 fiber. At the innermost of the MB and IB, a 10 mm thick Charge Veto is attached, which is  
 194 called MBCV and IBCV. The MBCV and IBCV consisted of the scintillator and WLS fiber,  
 195 which was used to veto the charged particle.

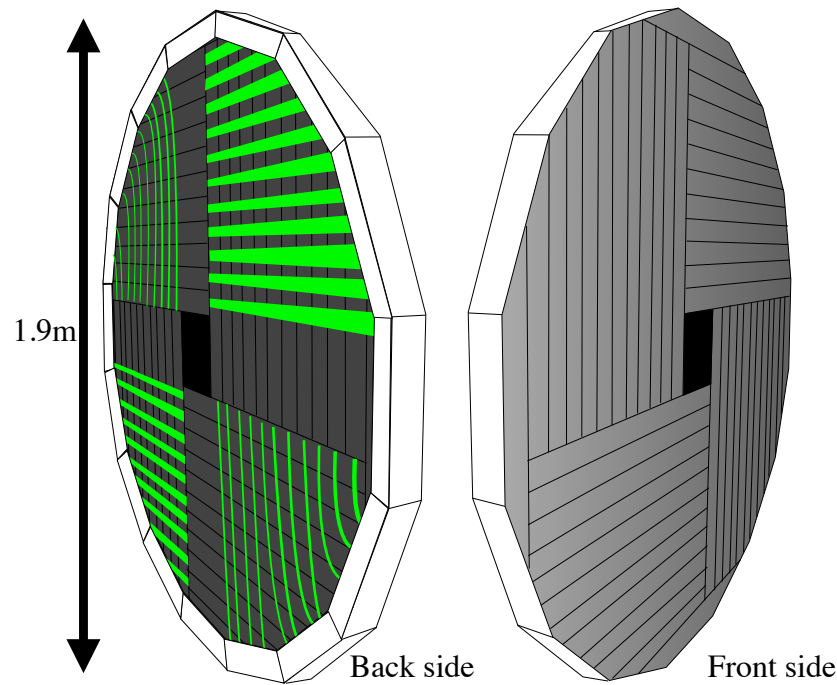


FIGURE 2.8: The Schematic Diagram of Charge Veto Structure.

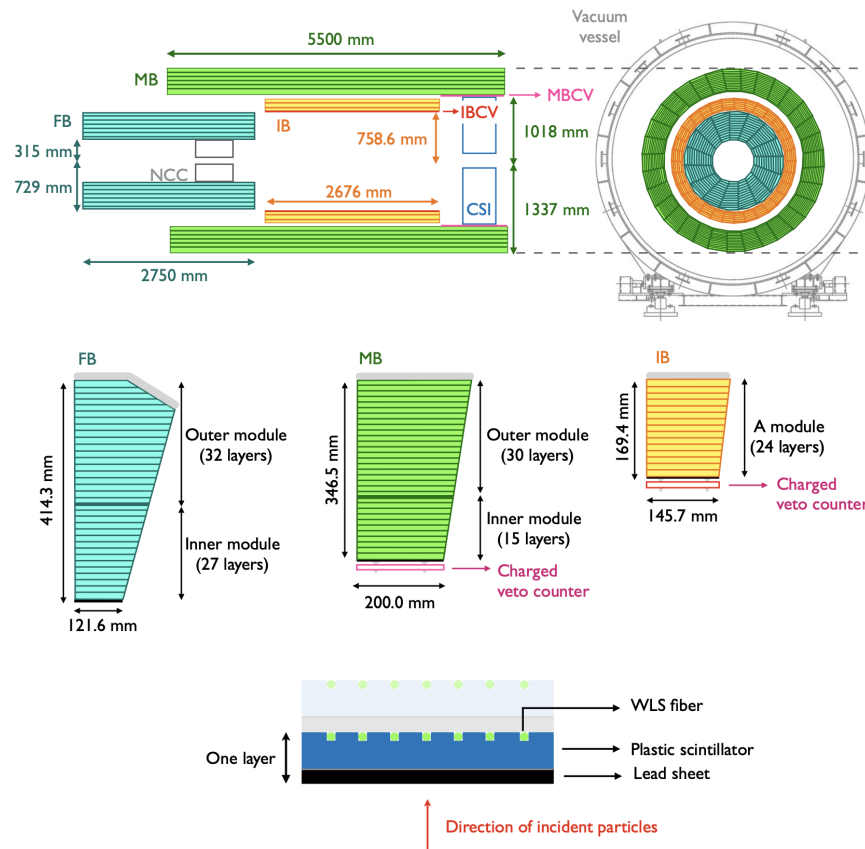


FIGURE 2.9: The Schematic Diagram of Barrel Veto Structure. Figure courtesy of [15].

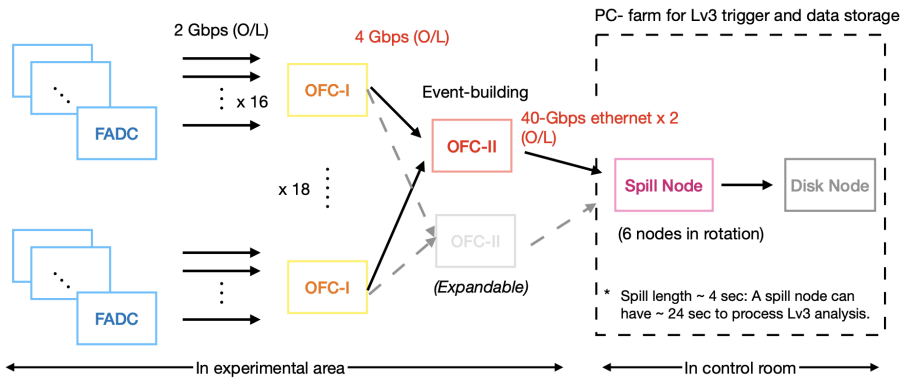


FIGURE 2.10: The architecture of the KOTO DAQ system. [16]

## 196 2.4 Data Acquisition System

197 When a particle hits the detectors, the electronic signal will be generated. To determine  
 198 whether this signal is interesting, a trigger system is used to decide the candidate events.  
 199 If an event passes any trigger criteria, the data acquisition system (DAQ) will collect and  
 200 store the data.

201 The DAQ system of the KOTO experiment consists of 3 levels: the first-level (L1) and  
 202 second-level (L2) trigger placed in the experiment area, and the third-level trigger (L3) at  
 203 the PC farm. The architecture of the DAQ system is shown in Figure 2.10.

204 KOTO detector has nearly 4000 channels in total, all these channels are connected to  
 205 the flash analog-to-digital converter (FADC) board to digitize the signal. There are two  
 206 types of FADC boards in the KOTO detector, with 125 MHz and 500 MHz sampling rates.  
 207 We have a total of 288 FADC boards and separate them into 18 crates with 16 boards in  
 208 each crate.

209 For the 125 MHz FADC, 16 channels are connected to each board, and the 500 MHz  
 210 FADC has 4 channels on each board.

<sup>211</sup> **Chapter 3**

<sup>212</sup> **Event Reconstruction**

<sup>213</sup> Event reconstruction is a crucial step in the analysis of decay events. After the reconstruction,  
<sup>214</sup> the kinematic variable of the  $K_L^0$ , such as the decay vertex, energy, and momentum,  
<sup>215</sup> can be obtained. With kinematic information, precise event selection can be achieved and  
<sup>216</sup> the performance of physical analysis can be improved.

<sup>217</sup> To reconstruct a  $K_L^0$  decay event, it is necessary to accurately model the decay process.  
<sup>218</sup> The primary strategy involves initially identifying photon clusters. Subsequently, the  
<sup>219</sup> clusters' energy, timing, and position on the CsI are utilized to reconstruct the parent  
<sup>220</sup> particle. This includes determining kinematic properties such as the decay vertex, energy,  
<sup>221</sup> and momentum of the parent particle. The specific details of the reconstruction process  
<sup>222</sup> vary depending on the decay mode. For channels involving pions, such as  $K_L^0 \rightarrow 3\pi^0$  and  
<sup>223</sup>  $K_L^0 \rightarrow \pi^0\pi^0$ , the photon clusters are mapped to pions, which are then used to reconstruct  
<sup>224</sup> the Kaon. In simpler decay channels like  $K_L^0 \rightarrow 2\gamma$ , the  $K_L^0$  is directly reconstructed from  
<sup>225</sup> the photon data.

<sup>226</sup> **3.1 Photon Cluster Finding**

<sup>227</sup> In this step, we need to find the photon cluster and then reconstruct the energy, timing,  
<sup>228</sup> and the hit position of the cluster. This process is called "clustering".

<sup>229</sup> First, need to find the cluster. The crystal which has deposited energy larger than 3  
<sup>230</sup> MeV and the hit timing is within 150 ns is considered a "seed crystal". Then, scanning  
<sup>231</sup> the neighboring crystals in a 140 mm wide square box around the seed crystal. The  
<sup>232</sup> neighboring crystals will add to the same cluster if the neighboring crystal is also a seed  
<sup>233</sup> crystal. And do the same scanning process for the neighboring crystals of the neighboring  
<sup>234</sup> crystals, til there is not a neighboring friend that can be found. This process will be  
<sup>235</sup> applied to all the seed crystals that have not been assigned to any cluster yet. A seed  
<sup>236</sup> crystal without any neighboring friend will be defined as an "isolated crystal hit". The  
<sup>237</sup> isolated crystal hit will be used in the CsI veto. The algorithm is illustrated in Figure 3.1.

<sup>238</sup> Because of the wide 150 ns timing window, the cluster may contain the hits not belong  
<sup>239</sup> to the cluster shower. A seed crystal is assigned to a cluster, but it does not come from  
<sup>240</sup> the cluster shower will be defined as an "accidental hit" and should be removed from the

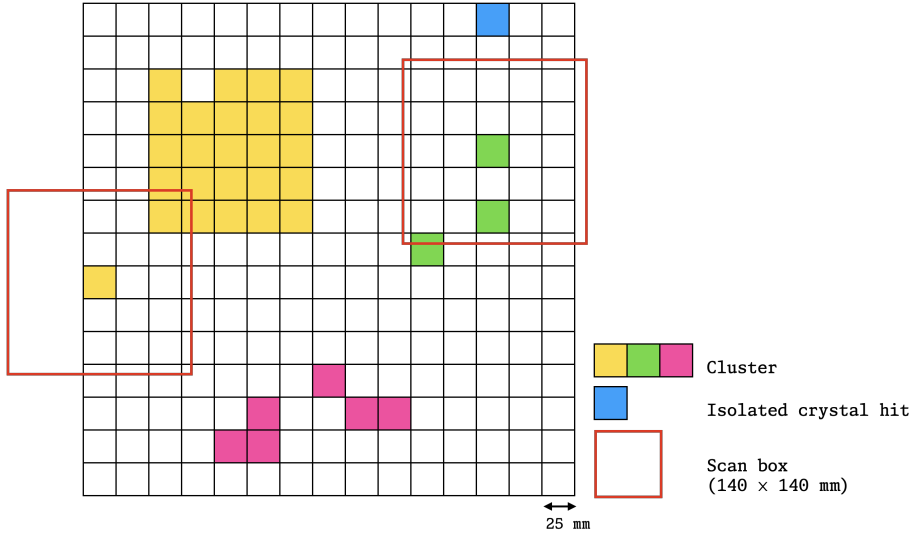


FIGURE 3.1: The illustration of the cluster finding process. All the color crystals are the seed crystals, and the crystals with the same color belong to the same cluster. The black crystal is the isolated crystal hit.

<sup>241</sup> cluster. To avoid the accidental hit, the cluster timing was used to do the selection. The  
<sup>242</sup> cluster timing ( $T_{cluster}$ ) is defined by the equation 3.1.

$$T_{cluster} = \frac{\sum_{n=1}^{i=1} T_i / \sigma_t^2}{\sum_{n=1}^{i=1} 1 / \sigma_t^2} \quad (3.1)$$

$$\sigma_t = 0.13 \oplus \frac{3.63}{\sqrt{E_i}} \oplus \frac{5}{E_i} \quad (3.2)$$

<sup>243</sup> Where  $n$  is the number of crystals in the cluster,  $i$  is the  $i$ -th crystal, and  $e$  is the energy  
<sup>244</sup> of the cluster. The  $\sigma_t$  is the timing uncertainty of each crystal, which is a function of  
<sup>245</sup> the energy of each crystal[17]. If a seed crystal from a cluster with timing outside the  
<sup>246</sup>  $\pm 5\sigma$  boundary of its cluster timing, it will be defined as an accidental hit and will be  
<sup>247</sup> removed. Figure 3.2 shows the timing boundary for a crystal seed after subtracting the  
<sup>248</sup> cluster timing. The cluster timing will recalculate after removing the accidental hit and  
<sup>249</sup> iterate this process until all accidental hits have been removed.

<sup>250</sup> Moreover, a timing selection will apply to the clusters. Because the cluster should be  
<sup>251</sup> produced by the same Kaon decay, the timing of the cluster should be within a certain  
<sup>252</sup> range. Therefore, the maximum timing difference between all clusters should be within  
<sup>253</sup> 30 ns. Otherwise, the cluster that has the largest timing difference with the average timing  
<sup>254</sup> of all clusters will be removed. This process will be repeated until all clusters satisfy the  
<sup>255</sup> timing selection.

<sup>256</sup> The cluster after the above process will be used in the next step of the reconstruction.  
<sup>257</sup> The below information on the cluster will be calculated and provided to the next step.

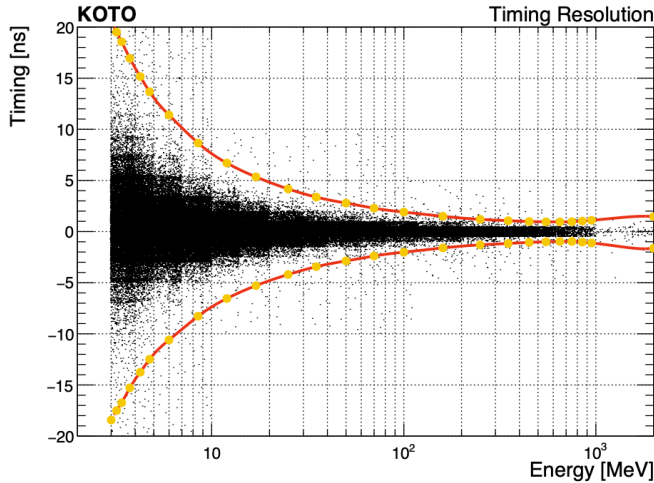


FIGURE 3.2: Timing boundary for a cluster seed based on the scattered plot of crystal timing versus energy deposit. A Gaussian function is fitted at each energy bin and the boundary is defined by  $\mu \pm 5\sigma$ , where  $\mu$  and  $\sigma$  are the Gaussian mean and standard deviation. The orange points indicate the boundary at the associated energy bin. The red curve connects all the points for the interpolation of the boundary value between the points. (Figure courtesy of [15])

258      **Cluster Energy ( $E_{cluster}$ )**

259      The energy of the cluster is the sum of the energy of all crystals in the cluster.

$$E_{cluster} = \sum_{i=1}^n E_i \quad (3.3)$$

260      **Cluster Position ( $x_{cluster}, y_{cluster}$ )**

261      The position of the cluster is defined by its center of energy, and the position is  
262      calculated by the equation below.

$$x_{cluster} = \frac{\sum_{i=1}^n E_i x_i}{E_{cluster}} \quad (3.4)$$

$$y_{cluster} = \frac{\sum_{i=1}^n E_i y_i}{E_{cluster}} \quad (3.5)$$

263      **3.2 Reconstruction of  $\pi^0$**

264      The  $\pi^0$  is reconstructed by two photon clusters. Figure 3.3 shows the schematic diagram  
265      of the  $\pi^0 \rightarrow 2\gamma$  decay process. First, the decay vertex needs to be determined, assum-  
266      ing the decay vertex is  $(0, 0, z_{vtx})$ . Therefore, the three momenta of the photon can be  
267      calculated by

$$\vec{P}_\gamma = k \cdot (x, y, \Delta z) \quad (3.6)$$

268      where the  $k$  is a constant does not determine yet. And the  $\Delta z$  is the difference between  
269      the z position of the cluster and the decay vertex.

$$\Delta z = z_{CsI} - z_{vtx} \quad (3.7)$$

270      Based on four-momentum conservation, the opening angle ( $\theta$ ) between two photons is  
271      calculated by

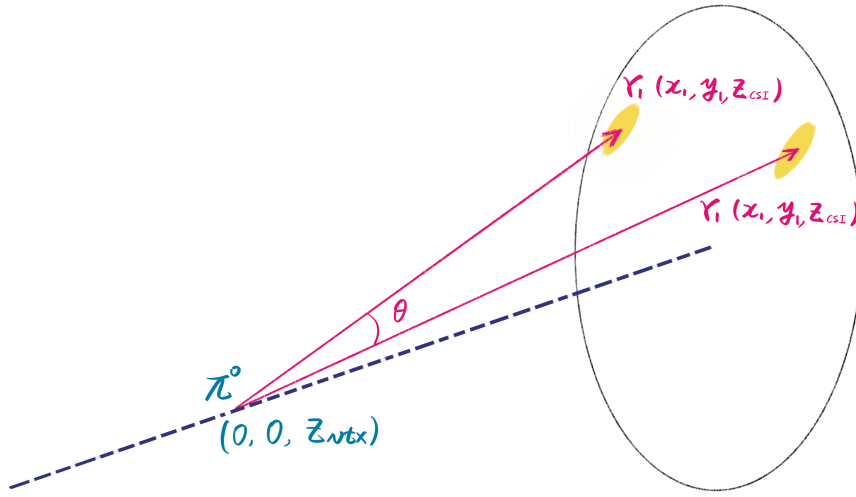


FIGURE 3.3: The schematic diagram of the  $\pi^0 \rightarrow 2\gamma$  decay process.

$$\cos(\theta) = 1 - \frac{M_{\pi^0}^2}{2 \cdot E_{\gamma 1} \cdot E_{\gamma 2}} \quad (3.8)$$

272 and combine with the inner product of two photons' momentum, the following equation  
273 can derive the  $z_{vtx}$ .

$$1 - \frac{M_{\pi^0}^2}{2 \cdot E_{\gamma 1} \cdot E_{\gamma 2}} = \frac{P_{\gamma 1} \cdot P_{\gamma 2}}{|P_{\gamma 1}| \cdot |P_{\gamma 2}|} \quad (3.9)$$

274 After determining the  $z_{vtx}$ , the momentum of the photon can be calculated by

$$|\vec{P}_\gamma| = E_\gamma \quad (3.10)$$

275 The energy and momentum of the  $\pi^0$  can be calculated by

$$E_{\pi^0} = E_{\gamma 1} + E_{\gamma 2} \quad (3.11)$$

$$\vec{P}_{\pi^0} = \vec{P}_{\gamma 1} + \vec{P}_{\gamma 2} \quad (3.12)$$

### 276 3.3 Reconstruction of Decays

277 In this section, the reconstruction algorithm for the  $K_L^0 \rightarrow 3\pi^0$  and  $K_L^0 \rightarrow \gamma\bar{\gamma}$  decay will  
278 be introduced. The  $K_L^0 \rightarrow 3\pi^0$  decay is used to evaluate the  $K_L^0$  yield, and the  $K_L^0 \rightarrow \gamma\bar{\gamma}$   
279 decay is for the physics analysis. In other KOTO experiment studies, the  $K_L^0 \rightarrow \pi^0\pi^0$  and  
280  $K_L^0 \rightarrow 2\gamma$  decay are also used in the yield estimation and are not covered in this section.  
281 Because the  $K_L^0 \rightarrow 3\pi^0$  is the only decay channel used for the yield estimation.

282 All the  $K_L^0$  decay reconstruction is based on the result from the clustering process. A  
283 minimal energy selection of 20 MeV is required for the photon cluster. Also, the number  
284 of photon cluster requirement need to be equal to the final state of the decay. For the

285  $K_L^0 \rightarrow 3\pi^0$  decay, the event needs to have exactly 6 photon clusters. For the  $K_L^0 \rightarrow \gamma\bar{\gamma}$   
 286 decay, the event should contain only 1 photon cluster.

287 After the  $K_L^0$  decay vertex reconstruction, then calculate the kinematic variables. The  
 288 kinematic variable will be utilized in the next step analysis.

289 **3.3.1 Reconstruction of  $K_L^0 \rightarrow 3\pi^0$**

290  $K_L^0 \rightarrow 3\pi^0$  decay has three  $\pi^0$  in the decay process, the reconstruction of  $\pi^0$  will use  
 291 the same algorithm as the previous section. The special situation is there are six photon  
 292 clusters on the CsI, and the  $\pi^0$  can be reconstructed in different combinations. All the  
 293 combinations will be considered because the true combination is unknown. The most  
 294 number of combinations for  $K_L^0 \rightarrow 3\pi^0$  is

$$\binom{6}{2} \binom{4}{2} \binom{2}{2} / 3! = 15$$

295 Because of the short lift time of the  $\pi^0$ , the decay vertex of the  $\pi^0$ 's should be very close.  
 296 Therefore, the  $\chi_z^2$  could be used to select the best combination.

$$\chi_z^2 = \sum_i^{N_{\pi^0}} \left( \frac{z_{vtx}^i - \bar{z}_{vtx}}{\sigma_i^2} \right)^2 \quad (3.13)$$

297 where  $N_{\pi^0}$  is the number of  $\pi^0$  in the decay,  $z_{vtx}^i$  is the decay vertex z of the  $i$ -th  $\pi^0$ ,  $\bar{z}_{vtx}$   
 298 is the average decay vertex z of all  $\pi^0$ , and  $\sigma_i$  is the uncertainty propagated from the  
 299 calorimeter of the  $i$ -th  $\pi^0$ . The best combination of  $\pi^0$  should have the smallest  $\chi_z^2$ . The  
 300 weighted average decay vertex z is also defined as the decay vertex z of  $K_L^0$ , calculated  
 301 by

$$\bar{z}_{vtx} = \frac{\sum_i^{N_{\pi^0}} z_{vtx}^i / \sigma_i^2}{\sum_i^{N_{\pi^0}} 1 / \sigma_i^2} \quad (3.14)$$

302 From the  $\pi^0$  reconstruction, the  $\pi^0$  decay vertex was assumed in the center of the CsI.  
 303 To determine the real decay vertex, a correction process was applied. As shown in Figure  
 304 3.4, the  $K_L^0$  travels start from the target and end at the decay vertex, then decay to the  $\pi^0$ s  
 305 and  $\gamma$ s hit on the CsI, and  $K_L^0$  project to the center of energy (COE). Therefore, the  $K_L^0$   
 306 decay vertex can be calculated based on the geometry, by the following equation.

$$x_{vtx} = x_{COE} \cdot \frac{z_{vtx} - z_{target}}{z_{CsI} - z_{target}} \quad (3.15)$$

$$y_{vtx} = y_{COE} \cdot \frac{z_{vtx} - z_{target}}{z_{CsI} - z_{target}} \quad (3.16)$$

307 where  $z_{target}$  is the z position of the target. The  $x_{COE}$  and  $y_{COE}$  can calculate by

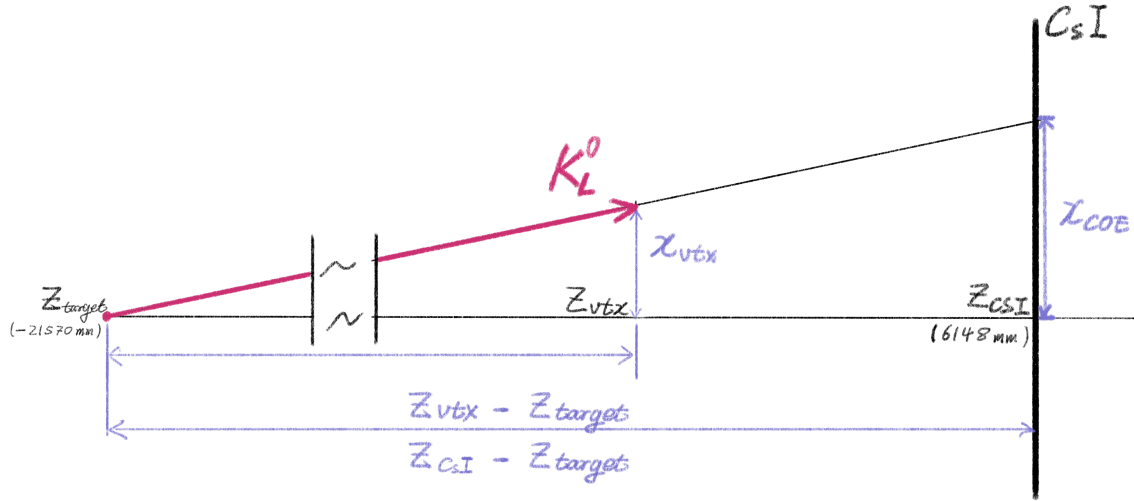


FIGURE 3.4: The schematic diagram of the  $K_L^0$  travel and decay process and geometry relationships

$$x_{\text{COE}} = \frac{\sum_{i=1}^{n_\gamma} E_i x_i}{\sum_{i=1}^{n_\gamma} E_i} \quad (3.17)$$

$$y_{\text{COE}} = \frac{\sum_{i=1}^{n_\gamma} E_i y_i}{\sum_{i=1}^{n_\gamma} E_i} \quad (3.18)$$

After obtaining the corrected decay vertex, the energy and momentum of the  $K_L^0$  can be obtained intuitively from the summation of all the  $\pi^0$ 's energy and momentum, as same as the Equation 3.11.

$$E_{K_L^0} = \sum_{i=1}^{N_{\pi^0}} E_{\pi^0} \quad (3.19)$$

$$\vec{P}_{K_L^0} = \sum_{i=1}^{N_{\pi^0}} \vec{P}_{\pi^0} \quad (3.20)$$

### 3.3.2 Reconstruction of $K_L^0 \rightarrow \gamma\bar{\gamma}$

$K_L^0 \rightarrow \gamma\bar{\gamma}$  Decay is the primary target of this analysis. The final state of  $K_L^0 \rightarrow \gamma\bar{\gamma}$  is similar to  $K_L^0 \rightarrow 2\gamma$ , but one photon is a dark photon. Due to the missing energy, the signature on CsI of  $K_L^0 \rightarrow \gamma\bar{\gamma}$  decay is only one photon cluster hit. Based on Section 3.1, the information that could be obtained from one photon cluster is only its energy, timing, and position on the CsI surface. With this limited information, it is impossible to reconstruct the  $K_L^0$  decay vertex. Therefore, the lack of kinematic information is the biggest challenge of the  $K_L^0 \rightarrow \gamma\bar{\gamma}$  decay search study.

### 3.3.3 Correction for Energy and Position of Photon Clusters

After the reconstruction of the  $K_L^0$  decay, and also obtaining the corrected decay vertex, the energy and position of the photon clusters will be possible to correct. Because this

322 correction process needs the incident angle of the photon, this process has to be done  
 323 after the  $K_L^0$  decay reconstruction. After the correction, we will use the new position to  
 324 recalculate the decay vertex.

325 **Position Correction**

326 The position of the photon cluster obtained from the clustering process is the position of  
 327 the center of energy of the cluster. As shown in the Figure 3.5. The  $z$  position for the  
 328 center of energy of the cluster is inside the crystal. However, the  $z$  position of the CsI  
 329 we used in the reconstruction is the position of the crystal surface. This difference will  
 330 introduce a bias for the reconstruction of the vertex position. To eliminate this bias, the  $x$   
 331 and  $y$  positions of the photon cluster need to be corrected to the real incident position.

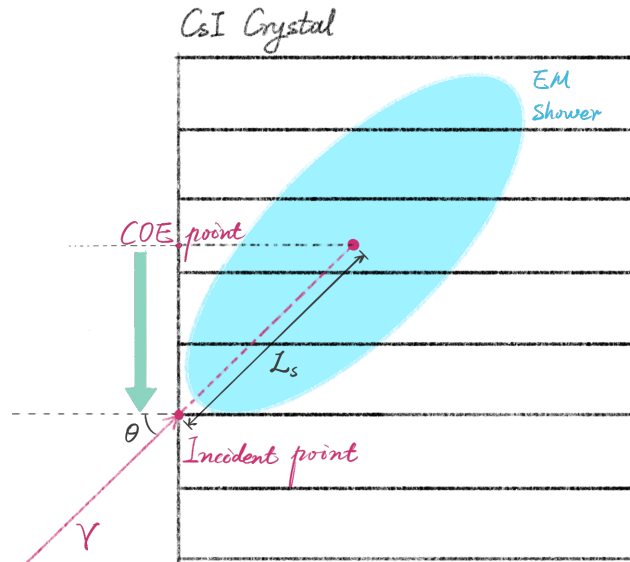


FIGURE 3.5: The schematic diagram of the correction of the photon cluster position.

332 From the decay vertex reconstruction, the incident angle ( $\theta$ ) of the photon was ob-  
 333 tained. And the corrected distance ( $L_c$ ) can be calculated by

$$L_c = L_s \cdot \sin(\theta) \quad (3.21)$$

334 where the  $L_s$  is the distance from the incident point to the cluster COE of the EM shower,  
 335 and the  $L_s$  can be calculated by

$$L_s/X_0 = p_0 + p_1 \ln(E[\text{GeV}]) \quad (3.22)$$

336 where the  $X_0 = 18.5$  is the radiation length of the CsI,  $E$  is the cluster energy in GeV, and  
 337 the  $p_0 = 6.490$  and  $p_1 = 0.993$  are the parameters obtains from the MC simulation.

338 **Energy Correction**

339 In the clustering process, a 3 MeV energy threshold was applied to the seed crystal. And  
 340 EM shower also possibly has leakage energy from the crystals and is not included in the  
 341 cluster. These factors will cause the energy lost from the measurement. To correct these  
 342 energy losses, a correction function dependence on energy was obtained from the MC  
 343 simulation.

$$E_{corr} = E \cdot (1 + w(E)) \quad (3.23)$$

344 where  $w(E)$  is the correction function.

345 After the correction of the energy and position of the photon cluster, the decay recon-  
 346 struction will be repeated. The final result will be used in the next step of the analysis.

347 **3.4 Veto Hit Reconstruction**

348 The veto counter is used in the background rejection. The rejection is based on the tim-  
 349 ing of the veto hit and the deposited energy. And that is the information we need to  
 350 reconstruct from the veto hit.

351 The reject criteria require an energy deposit over the energy threshold, which can dis-  
 352 tinguish the signal from the background noise, and a hit timing within the timing win-  
 353 dow to ensure the hit is from the same  $K_L^0$  decay event, this kind of hit is called an "on-  
 354 time" hit. Because the veto information is exclusively utilized for background rejection  
 355 criteria in this study, the hit timing was selected as the hit that was closest to the nominal  
 356 timing if there was more than one hit on the veto counter.

357 To do the timing criteria, a veto timing( $T_{veto}$ ) was defined, which is the difference  
 358 between the veto hit timing and the  $K_L^0$  decay timing. The veto timing is defined as

$$\begin{cases} T_{veto} &= T_{mod} - T_{vtx} - TOF \\ TOF &= D/c, \end{cases} \quad (3.24)$$

359 where the  $T_{mod}$  is the veto hit timing,  $T_{vtx}$  is the  $K_L^0$  decay timing,  $TOF$  is the time-of-  
 360 flight of the particle,  $D$  is the distance between the decay vertex and the veto hit position.  
 361 As shown in the Figure 3.6.

362 However, this equation has to involve the vertex information, which is not available  
 363 in the  $K_L^0 \rightarrow \gamma\bar{\gamma}$  analysis. Therefore, the  $T_{veto}$  needs to be modified to be independent of  
 364 the vertex information. The vertex timing  $T_{vtx}$  can be approximated by

$$T_{vtx} \approx T_{CsI} - \Delta z/c \quad (3.25)$$

365 where the  $T_{CsI}$  is the corrected average timing of the CsI clusters, and the  $\Delta z$  is the  
 366 difference between the z position of the CsI surface and the decay vertex. And with the

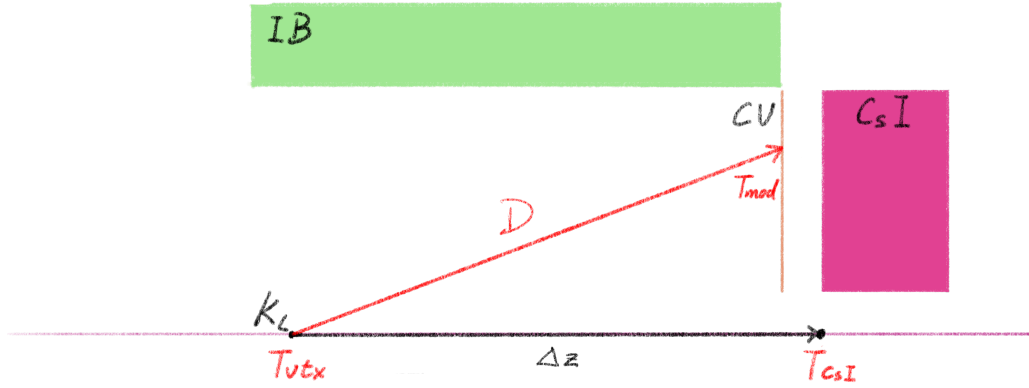


FIGURE 3.6: Schematic view of the timings used in the module-veto-timing calculation.

<sup>367</sup> Equation 3.24 the  $T_{veto}$  can be derived as

$$T_{veto} \approx T_{mod} - T_{CsI} + (\Delta z - D)/c \quad (3.26)$$

<sup>368</sup> The  $(\Delta z - D)$  is an uncontrolled variable because  $D$  still needs the vertex position information. Thankfully, most veto counters do not have a large scale along the z-axis, thus <sup>369</sup> <sup>370</sup> the variant of the  $(\Delta z - D)$  is small. Therefore,  $(\Delta z - D)$  can be treated as a constant in <sup>371</sup> most cases, and the  $T_{veto}$  can be equivalent to

$$T_{veto} \equiv T_{mod} - T_{CsI} \quad (3.27)$$

<sup>372</sup> This definition can be used in the all downstream veto count and also the FBAR and the <sup>373</sup> NCC veto counter. However, the Barrel veto counter does not satisfy the condition that <sup>374</sup> has a large scale along the z-axis, and the  $(\Delta z - D)$  is not negligible.

<sup>375</sup> In the following section, some special treatment of the veto hit will be explained,

### <sup>376</sup> 3.4.1 Barrel Veto Counters

<sup>377</sup> The Barrel veto counters contain the Main Barrel(MB) and the Inner Barrel(IB), which <sup>378</sup> have a Both-End Readout system. The mechanism of the both-end readout veto hit is <sup>379</sup> shown in Figure 3.7. And the  $T_{mod}$  could be calculated by the upstream and downstream <sup>380</sup> PMT timing.

$$\begin{cases} T_{mod} = T_u - L_u/v, \\ T_{mod} = T_d - L_d/v \end{cases} \quad (3.28)$$

<sup>381</sup> where the  $T_u$  and  $T_d$  are the timing of the upstream and downstream, and  $L_u(L_d)$  is the <sup>382</sup> distance between the hit position to the upstream (downstream) PMT,  $v$  is the propagated <sup>383</sup> velocity in the module. Therefore, the  $T_{mod}$  can be calculated by

$$T_{mod} = \frac{T_u + T_d}{2} - \frac{L}{2v} \quad (3.29)$$

<sup>384</sup> The hit position  $z_{hit}$  of the veto counter can be derived as

$$z_{hit} = z_{center} + \frac{v \cdot (T_u - T_d)}{2} \quad (3.30)$$

<sup>385</sup> where the  $z_{center}$  is the  $z$  position of the center of the barrel veto counter.

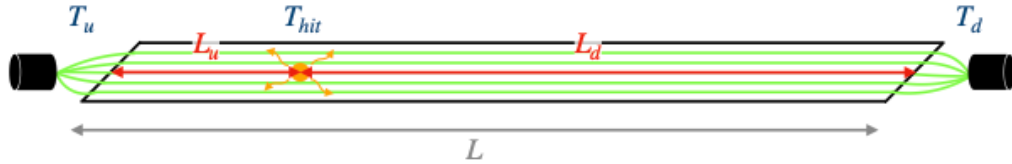


FIGURE 3.7: The Schematic diagram of a photon hit with the generated scintillation lights propagating to both directions and captured by PMTs. Figure courtesy of [15]

<sup>386</sup> The geometry relationships of the Barrel veto hit are shown in Figure 3.8. The  $(\Delta z - D)$   
<sup>387</sup> from Equation 3.26 can be approximated by

$$\Delta z - D \approx \Delta S, \quad (3.31)$$

$$\Delta S = \sqrt{R^2 + (z_{hit} - z_{CsI})^2} \quad (3.32)$$

<sup>388</sup> where  $R$  is the radius of the Barrel veto counter. And the  $T_{veto}$  can be derived as

$$T_{veto} = T_{mod} - T_{CsI} + \Delta S/c \quad (3.33)$$

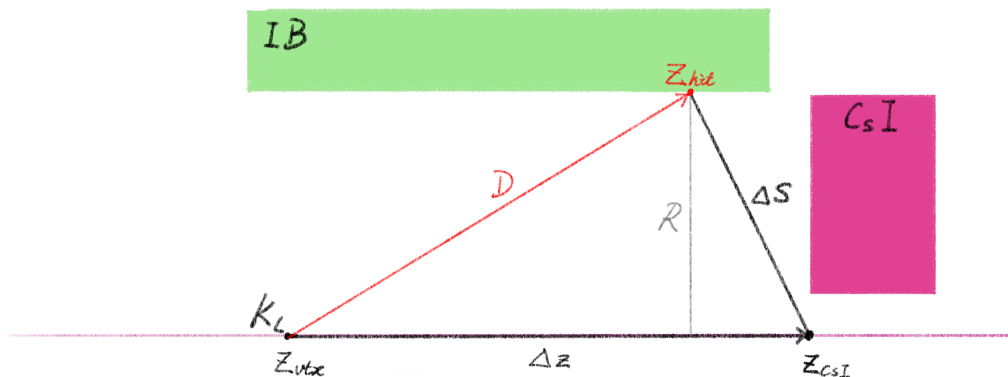


FIGURE 3.8: The Schematic diagram of geometry relationships of the Barrel veto counter.

### <sup>389</sup> 3.4.2 CsI Calorimeter

<sup>390</sup> As Section 3.1 mentioned, the CsI calorimeter is used to reconstruct the photon cluster.  
<sup>391</sup> All the crystal hits on the CsI Calorimeter will be used in the clustering process. How-  
<sup>392</sup> ever, some crystal hits cannot be assigned to any cluster, and these hits are defined as  
<sup>393</sup> "Isolated Crystal Hits". Even though a cluster has been constructed, if it does not satisfy

394 the  $\pi^0$  reconstruction criteria, it will not be assigned to any  $K_L^0$  or  $\pi^0$ , and these clusters  
 395 are defined as "Extra Clusters". The mechanism of these hits could come from a photo-  
 396 nuclear reaction in the shower propagation. These two types of hits will be used in the  
 397 veto rejection.

398 Because this detector is also the calorimeter, the veto timing definition needs to be  
 399 modified. For the "extra clusters" the timing of the decay vertex ( $T_{vtx}$ ) is not recalculated  
 400 for each cluster,

$$T_{vtx} = T_{cluster} - L/c \quad (3.34)$$

401 where  $L$  is the distance between the decay vertex and the cluster.

402 For the "isolated crystal hits", because it possibly split from the other cluster. To avoid  
 403 this situation, the selection criteria variables are correlated to the nearest cluster. The  
 404 variable that needs to be reconstructed is the distance ( $D$ ) and the timing difference ( $T$ )  
 405 between the isolated crystal hit and the nearest cluster.

$$T_{veto} = T_{crystal} - T_{cluster} \quad (3.35)$$

$$D = \sqrt{(x_{crystal} - x_{cluster})^2 + (y_{crystal} - y_{cluster})^2} \quad (3.36)$$



<sup>406</sup> **Chapter 4**

<sup>407</sup> **Monte Carlo Simulation**

<sup>408</sup> In this chapter, the Monte Carlo (MC) simulation of the KOTO experiment is described,  
<sup>409</sup> which is used for the  $K_L^0 \rightarrow \gamma\bar{\gamma}$  analysis. In the HEP analysis field, there are so many  
<sup>410</sup> physics mechanisms behind the physics data, to verify these mechanisms, the MC simu-  
<sup>411</sup> lation is used to simulate the physics process to help us understand the data behaviors.  
<sup>412</sup> The simulations were performed to reproduce real physics data and to estimate the  $K_L^0$   
<sup>413</sup> source background events. The MC simulation should reproduce the real data as much  
<sup>414</sup> as possible. Ideally, if all the background sources and mechanisms are well considered,  
<sup>415</sup> the MC simulation should reproduce the real data perfectly.

<sup>416</sup> The simulation procedure consists of the following steps. First, generate a set of  $K_L^0$   
<sup>417</sup> particles to enter the KOTO detector, simulate the decay of such particles in the detec-  
<sup>418</sup> tor, and simulate the detector response with the interaction of the decay products. The  
<sup>419</sup> simulation is performed using the GEANT4 toolkit [18, 19, 20]. Then convert the MC sim-  
<sup>420</sup> ulation result to the same format as the real data. To reproduce the same conditions of  
<sup>421</sup> the  $K_L^0$  as the real data run, a  $K_L^0$  momentum spectrum and beam structure are prepared  
<sup>422</sup> based on the real data. The MC simulation is performed with the same beam structure  
<sup>423</sup> and detector conditions as the real data. In addition, some other MC simulation is also  
<sup>424</sup> performed in this analysis to estimate the background events, such as the beamline sim-  
<sup>425</sup> ulation, upstream  $\pi^0$  background.

<sup>426</sup> **4.1 GEANT4 toolkit**

<sup>427</sup> GEANT4 (GEometry ANd Tracking) is a comprehensive software toolkit, which is pop-  
<sup>428</sup> ular in high energy physics, used for the simulation of the passage of particles through  
<sup>429</sup> matter. In the GEANT4 simulation, the simulation is performed step by step. In each  
<sup>430</sup> step, the particle interacts with the detector material, and the energy deposits and the  
<sup>431</sup> direction change of the particle are calculated. The particle quantities are all stored in the  
<sup>432</sup> simulation output, thus it is easy to analyze the particle decay because its whole proce-  
<sup>433</sup> dure is traceable.

## 434 4.2 Detector Response

435 The GEANT4 simulation toolkit can provide the timing, energy deposit, and position of  
 436 the particle interaction, but it is the ideal information, called "true information", which  
 437 cannot be directly compared with the real data. The kinematic information is recon-  
 438 structed from the data detected by sensors. Therefore, simulations are necessary to repli-  
 439 cate the information given by the detector readout.

440 The KOTO detector contains several sub-detectors with different detected principles.  
 441 The majority method uses the scintillation process, to detect the propagated light by PMT.  
 442 The Čerenkov radiation was used in the BHPV and BHGC, and the gas ionization was  
 443 used in the BHCV.

## 444 4.3 Pulse Simulation

445 The FADC digitized pulses can be described by an asymmetric Gaussian function  $f(t)$  as

$$446 f(t) = A \exp \left( - \left( \frac{t - \mu}{(\sigma_0 + a(t - \mu))} \right)^2 \right) \quad (4.1)$$

447 where  $t$  is the time of the pulse,  $\mu$  is the peak timing,  $\sigma_0$  and  $a$  are the parameters that  
 448 determine the shape of the pulse which are given for each detector channel.  $A$  is the  
 449 normalization factor determined by the integration of  $f(t)$  to energy.

## 450 4.4 $K_L^0$ Generation

451 In the Monte Carlo simulation, the  $K_L^0$  particles are generated at the  $K_L^0$  beam exit which  
 452 is 1507 mm upstream of the detector. Given the momentum and production position of  
 453 the  $K_L^0$  particles, the decay process can be simulated. There are two methods that can  
 454 obtain the momentum and position distribution, one is called beamline simulation and  
 455 the other is called the empirical  $K_L^0$  momentum spectrum.

### 456 4.4.1 Beamline Simulation

457 The  $K_L^0$  beam in the KOTO experiment is produced from the proton-gold fix target colli-  
 458 sions. The simulation that starts from the proton collisions is called the beamline simula-  
 459 tion. Because the beamline simulation simulates the whole beamline, the  $K_L^0$  momentum  
 460 and position can be obtained directly.

461 In the simulation, a 30 GeV proton beam hit the gold target was simulated. The beam-  
 462 line simulation simulates all the structures between the target and the 2nd collimator exit,  
 463 such as the photon absorber, sweeping magnet, and two collimators. If any particles re-  
 464 main at the 2nd collimator exit, the event will be recorded as an event seed. However,  
 465 the beamline simulation is inefficient to generate and cannot reproduce the  $K_L^0$  spectrum

perfectly. In the KOTO experiment, the empirical method is used to obtain the  $K_L^0$  momentum and position distribution.

Although the beamline simulation cannot be used to obtain the  $K_L^0$  spectrum, it is still useful to study the beam contents other than the  $K_L^0$  particles. Figure 4.1 shows the beam content population simulated by the beamline simulation under  $10^{12}$  POT.

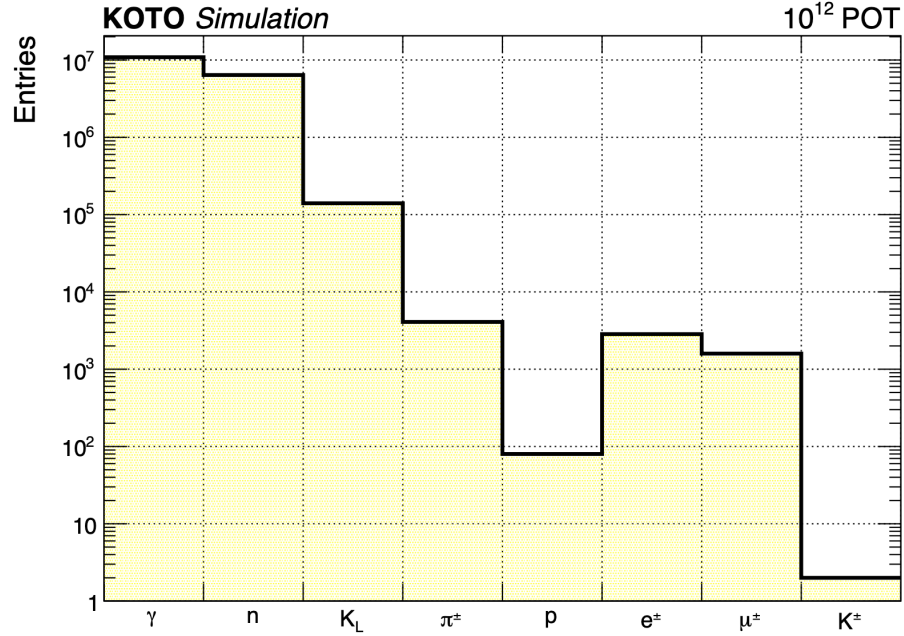


FIGURE 4.1: Beam content at the KOTO detector entrance based on the beamline simulation. Figure courtesy of [15]

In the KOTO experiment, the beamline simulation is used to study some background sources caused by the in-beam particle interaction, such as the NCC background, the halo  $K_L^0$  background, and the Charge Kaon background.

#### 4.4.2 Empirical $K_L^0$ Spectrum Simulation

The  $K_L^0$  momentum spectrum was obtained from the measurement result of the  $K_L^0 \rightarrow \pi^+ \pi^-$  and  $K_L^0 \rightarrow \pi^+ \pi^- \pi^0$  decays in 2012 engineering run [21]. Figure 4.2 shows the  $K_L^0$  momentum spectrum which is fitting by the asymmetry Gaussian function as

$$f(p) = \exp\left(-\frac{(p - \mu)^2}{2\sigma_0(1 - (A + Sp)(p - \mu))^2}\right) \quad (4.2)$$

where  $p$  is the momentum of the  $K_L^0$ ,  $\mu = 1.420$  GeV/c is the mean value of the momentum,  $\sigma_0 = 0.8102$  GeV/c is the width of the momentum,  $A = -0.3014$  and  $S = 0.01709$  (GeV/c) $^{-1}$  are the asymmetry parameters to be determined by fitting.

However, compared to the beamline simulation and empirical model, the  $K_L^0$  particles around the beam core (halo  $K_L^0$  particle) are not reproduced by the empirical model, as

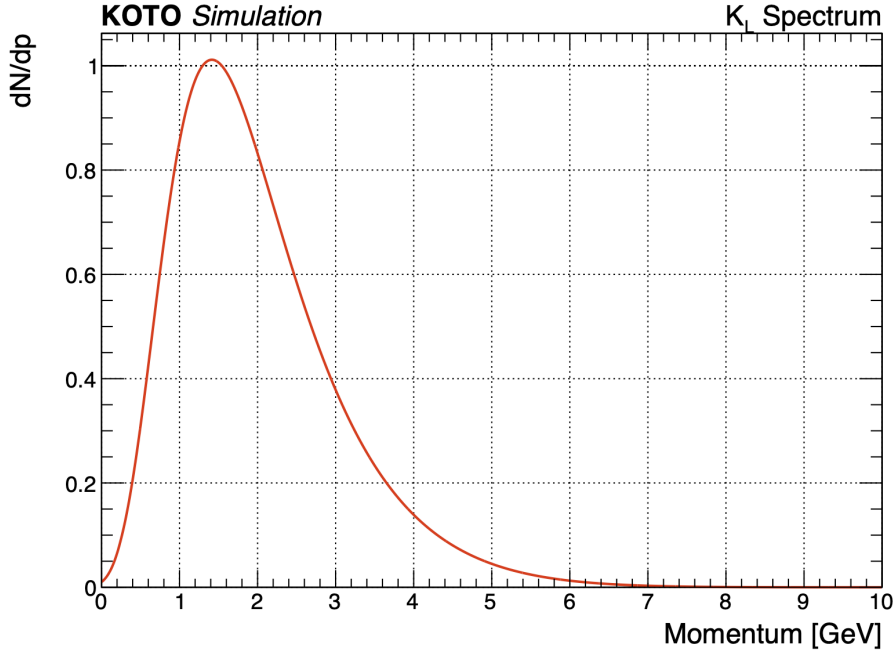


FIGURE 4.2: The  $K_L^0$  momentum spectrum at the exit of the second collimator. Figure courtesy of [15]

483 shown in Figure 4.3. This is because the empirical model does not consider the interac-  
 484 tions in the beamline. Therefore, the halo  $K_L^0$  may contribute to a background source and  
 485 need to be emulated by the beamline simulation.

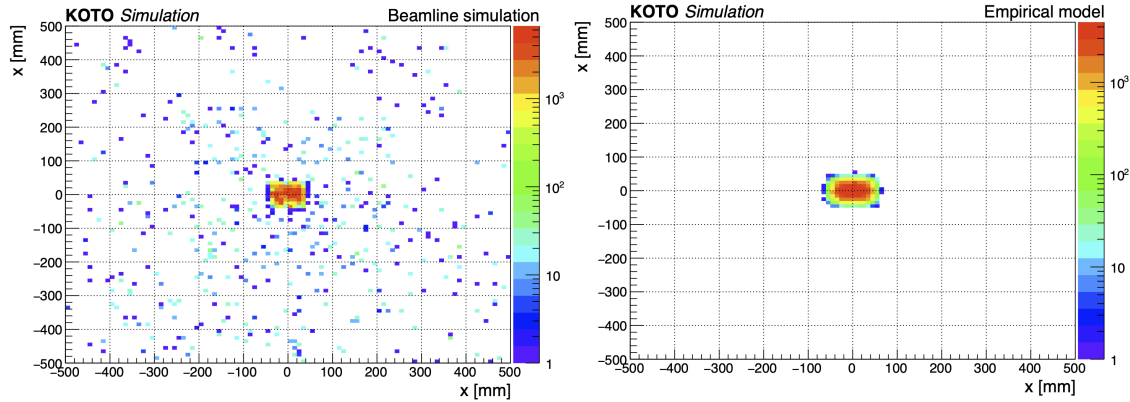


FIGURE 4.3: Comparison of  $K_L^0$  beam profile at the exit of the second collimator between the beamline simulation and the empirical model. Figure courtesy of [15]

## 486 4.5 Fast Simulation

487 Because the KOTO experiment has a large amount of data, the Monte Carlo simulation is  
 488 time-consuming. Especially for the large branching ratio  $K_L^0$  decay channels, such as the  
 489  $K_L^0 \rightarrow \pi^\pm e^\mp \nu_e$  and  $K_L^0 \rightarrow 3\pi^0$  decays. It not only takes a long time to simulate the decay  
 490 process but also occupies a large amount of disk space.

Take this study as an example, there are only 2-hour physics data with the protons on target (POT) of  $5.03 \times 10^{16}$ . A full MC simulation of a  $K_L^0 \rightarrow 3\pi^0$  decay would take approximately 3 days to generate the same decay statistics as data. In this study, we ended up generating 12 times as many  $K_L^0 \rightarrow 3\pi^0$  decays as the same amount of data. If we use the full MC simulation method, it would take around 30 days to generate the same statistics. The time consumption does not consider the priority of the batch job system, which consumes more time in real time. The branching ratio of  $K_L^0 \rightarrow \pi^\pm e^\mp \nu_e$  and  $K_L^0 \rightarrow \pi^\pm \mu^\mp \nu_\mu$  are even larger than the  $K_L^0 \rightarrow 3\pi^0$  decay. To prevent wasting the whole life being spent on the MC simulation, a fast simulation method is developed to speed up the MC simulation.

The fast simulation method is the same as the full simulation but breaks the generation process into three steps. In the first step, the  $K_L^0$  and its daughter particles are generated, and stop the simulation when they hit any detectors. Record the information that we are interested in. In the second step, make a simple selection of the events to reject the events that are not interested in. Take the  $K_L^0 \rightarrow 3\pi^0$  decay as an example, only the photon decay from the  $\pi^0$  was considered. The photon has to hit the CsI fiducial region and the decay vertex has to be before the CsI. Retention events pass the above selection, require a minimal number of photons which depends on the study, and require the total energy of the photon to be larger than the online trigger threshold. In the third step, based on the information of the retained events, restarted the simulation and simulated the detector response.

The fast simulation method is much faster than the full simulation. In the  $K_L^0 \rightarrow 3\pi^0$  decay case, the total MC simulation is done in 10 days which is 3 times faster than the full simulation. The enhancement of the speed depends on the selection criteria, if a more strict selection is applied, the enhancement of the speed will be more significant.

## 4.6 Accidental Overlay

Because the MC simulation is generated one by one  $K_L^0$  decays which is the ideal simulation. To reproduce the real data situation, the accidental activities need to be considered. For example, the triggered  $K_L^0$  decay event with another  $K_L^0$  decay coincidently, or the particle in the beam has some interaction and produces a cluster. To reproduce the accidental activities, the accidental activities were overlaid on the MC simulated events. The accidental activities' information was taken from the TMON-triggered data, which could reflect the accidental rate of the real data beam.

When doing the accidental overlay, an accidental event is randomly selected from the library, and superimposed to each channel of the event data. Figure 4.4 shows an example of an accidental overlay on a simulated pulse for a channel in the FBAR detector.

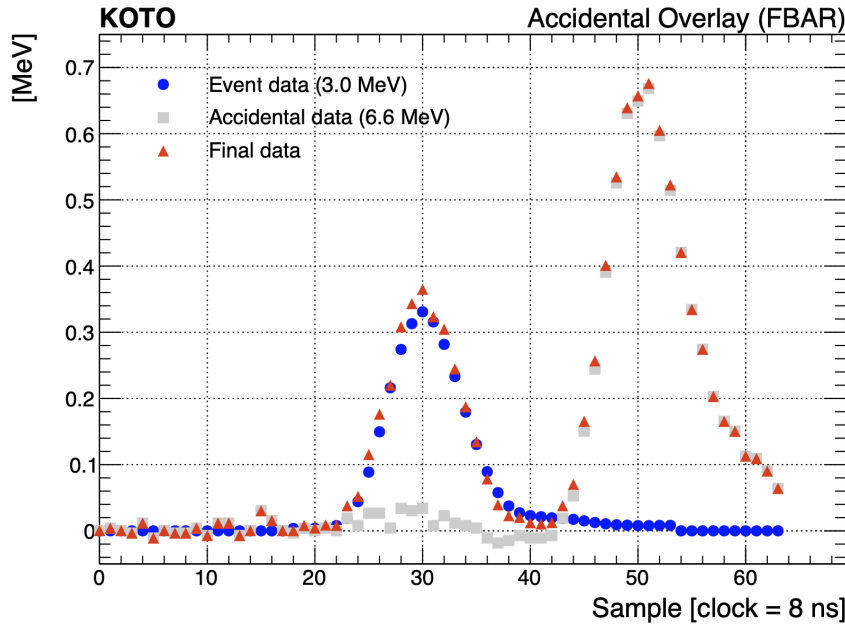


FIGURE 4.4: An example of the accidental overlay on a simulated pulse, subtracting the pedestal. Figure courtesy of [15]

## 527 4.7 Neutron background Simulation

528 Neutron background is one of the serious background sources in the KOTO experiment.  
 529 As shown in Figure 4.1, there is a large amount of neutron background in the beam.  
 530 The mechanism is simply neutron directly interacts with the CsI calorimeter. Because  
 531 the GEANT4 toolkit cannot generate a good reliable neutron interaction simulation, a  
 532 data-driven method is used to estimate the neutron background. An aluminum plate  
 533 target was inserted in front of the KOTO detector entrance perpendicularly to the beam  
 534 direction to enhance the neutron in the beam. This target is called the "Z0-Al target" and  
 535 the run with the Z0-Al target is called the "Z0-Al run". The Z0-Al run data is used to be  
 536 the neutron sample in the background suppression and the estimation study.

<sup>537</sup> **Chapter 5**

<sup>538</sup>  **$K_L^0$  Yield Estimation**

<sup>539</sup> The yield of  $K_L^0$  is an important parameter for most analyses in KOTO. To normalize  
<sup>540</sup> the Monte Carlo Simulation number of events to the real data, the yield of the  $K_L^0$  was  
<sup>541</sup> required. The  $K_L$  yield is usually estimated by well-known neutral decay channels with  
<sup>542</sup> large branching ratios, which are  $K_L^0 \rightarrow 3\pi^0$ ,  $K_L^0 \rightarrow \pi^0\pi^0$ , and  $K_L^0 \rightarrow 2\gamma$ . The branching  
<sup>543</sup> ratio of these three decays is shown in the Table 5.1. The background source of these three  
<sup>544</sup> channels is also limited.

TABLE 5.1: Branching ratio of  $K_L$  decays

Decay mode	Branching ratio
$K_L^0 \rightarrow 3\pi^0$	$(19.52 \pm 0.12)\%$
$K_L^0 \rightarrow \pi^0\pi^0$	$(8.64 \pm 0.06) \times 10^{-4}$
$K_L^0 \rightarrow 2\gamma$	$(5.47 \pm 0.04) \times 10^{-4}$

<sup>545</sup> The ideal decay channel for the normalization study is  $K_L^0 \rightarrow 2\gamma$  decay because the  
<sup>546</sup> two-photon final state is relatively similar to the  $K_L^0 \rightarrow \gamma\bar{\gamma}$  decay. However, due to insuffi-  
<sup>547</sup> cient time for collecting special run data, the statistics of  $K_L^0 \rightarrow \pi^0\pi^0$  and  $K_L^0 \rightarrow 2\gamma$  decay  
<sup>548</sup> are inadequate to estimate the  $K_L^0$  yield. The  $K_L^0 \rightarrow 3\pi^0$  decay is a good place to estimate  
<sup>549</sup> the  $K_L$  yield because its branching ratio is far greater than other neutral decay channels,  
<sup>550</sup> and a restrictive requirement of the signal signature. Therefore, the  $K_L^0 \rightarrow 3\pi^0$  decay  
<sup>551</sup> was accepted to estimate the  $K_L^0$  yield and do the normalization study in this search. On  
<sup>552</sup> further study of this search with better statistics, the normalization study could be based  
<sup>553</sup> on  $K_L^0 \rightarrow 2\gamma$  decay, and use the other two decays to do the cross-check.

<sup>554</sup> **5.1 Data Set**

<sup>555</sup> The data set for the normalization study was processed using the entire special run  
<sup>556</sup> physics data, along with the normalization trigger. The pre-scaling factor of 13 means  
<sup>557</sup> that for every 13 events triggered, only one event was stored. For the control sample,  
<sup>558</sup> we employed a Monte Carlo simulation of  $K_L^0 \rightarrow 3\pi^0$  decay that includes accidental  
<sup>559</sup> overlays. Approximately  $1 \times 10^9$   $K_L^0 \rightarrow 3\pi^0$  decay events were simulated for this con-  
<sup>560</sup> trol sample. Due to the distinct 6-cluster event signature characteristic of the  $K_L^0 \rightarrow 3\pi^0$   
<sup>561</sup> decay, the influence of other decay modes is negligible in the normalization study.

## 562 5.2 Event Selections

563 In the  $K_L^0$  Yield study, the objective of event selection is to isolate  $K_L^0 \rightarrow 3\pi^0$  decay events  
 564 while effectively rejecting background events. This selection process comprises two main  
 565 components: the veto cut and the kinematic cut. The veto cut is straightforward, requir-  
 566 ing an in-time hit in the veto counter. The kinematic cut, on the other hand, utilizes  
 567 photon data and the reconstructed physical quantities of  $K_L^0$  and  $\pi^0$ . This cut is further  
 568 divided into three categories: Trigger Cut, Photon Selection, and  $K_L^0$  Selection. A detailed  
 569 explanation of these cuts will be provided in the following section.

### 570 5.2.1 Trigger Cut

571 Due to the inability of the Monte Carlo simulation to accurately replicate the online Data  
 572 Acquisition (DAQ) system, it does not impose the same trigger conditions as those found  
 573 in the actual data. Consequently, the trigger cut was introduced to eliminate the effects  
 574 of the online triggers, thereby enhancing the comparability between simulated and real  
 575 data.

#### 576 Trigger Timing Window

577 In one 64-sample window, there may maybe more than one trigger hit. If there are sep-  
 578 arate events, it may cause a double counting of overlay events. To eliminate the bias  
 579 from this effect, an average photon timing window of  $\pm 15$  ns of the nominal timing was  
 580 required.

#### 581 Total Energy in CsI

582 The online Total energy in CsI (CSIET) threshold is set as 500 MeV in the special physics  
 583 run normalized trigger. To eliminate this online effect, a CSIET threshold offline was  
 584 required higher than the online threshold. In this study, an offline  $CSIET$  threshold of  
 585 650 MeV was required, which is the same as the  $K_L^0 \rightarrow \pi^0\nu\bar{\nu}$  study. The offline CSIET  
 586 threshold is determined by examining the ET efficiency curve, as explained in Section  
 587 6.3.1 of Jay's dissertation[15].

### 588 5.2.2 Photon Selection

589 Figure 5.1 shows the distribution of the photon selection variables for the  $K_L^0 \rightarrow 3\pi^0$   
 590 decay. The photon selection cuts include the photon energy, photon hit position, and  
 591 minimum cluster distance. These cuts are based on the photon information and are used  
 592 to select photons with good reconstruction reproducibility.

#### 593 Photon Energy ( $E_\gamma$ )

594 To improve the reconstruction quality of the photon, the ultra-soft photon with energy  
 595 less than 50 MeV was rejected.

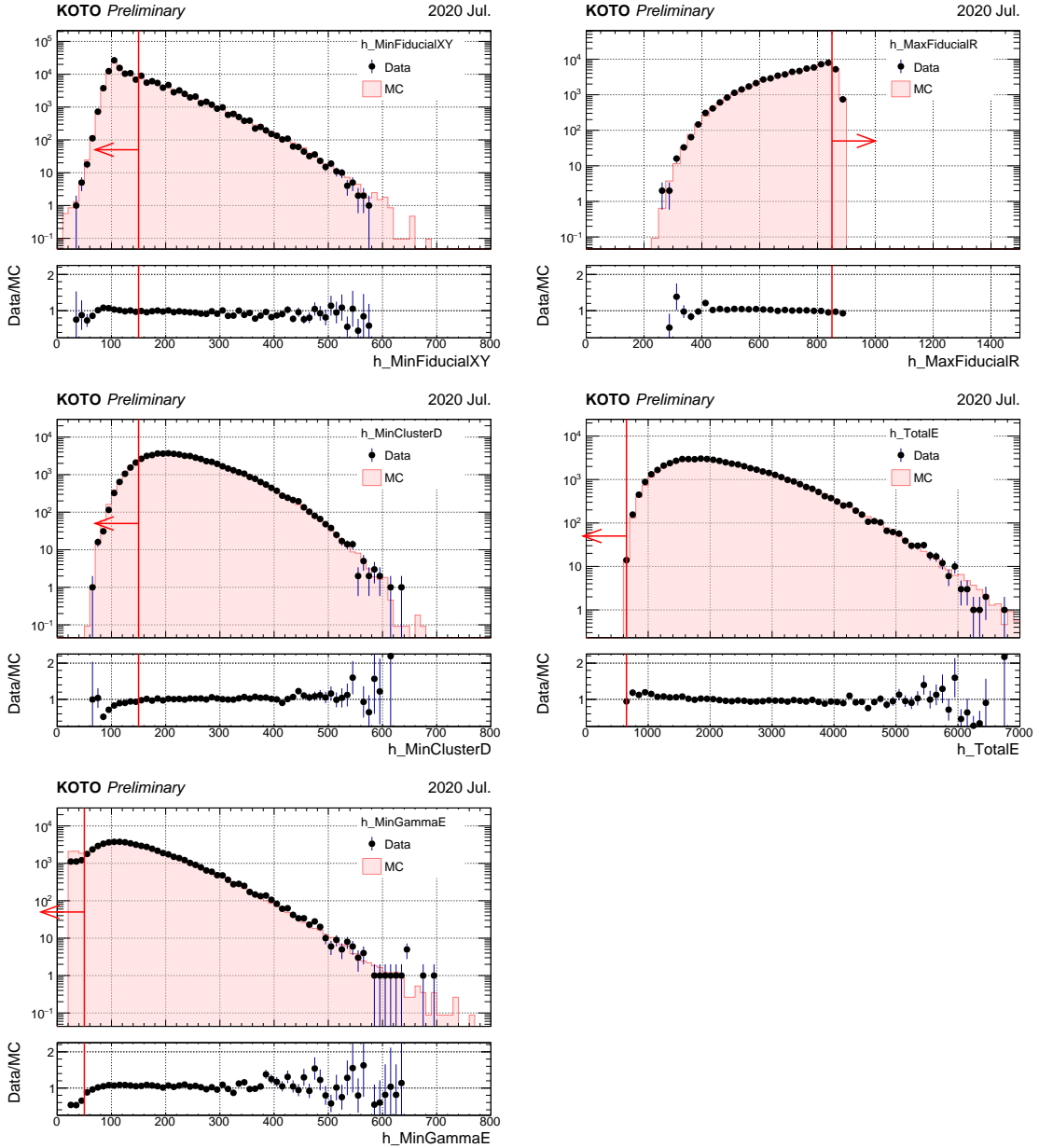


FIGURE 5.1: Distribution of the photon selection variables for the  $K_L^0 \rightarrow 3\pi^0$  decay. The photon selection cuts are applied except for the variable shown in the plot. The black point shows the data, and the fill histogram shows the Monte Carlo simulation. The red arrow indicates the cut-off value of the variable.

### 596 Photon Hit Position (Fiducial Cut)

597 To ensure the EM shower was well contained in the CsI calorimeter, a photon hit position  
 598 cut was applied. Any photon in an event that hit the outermost and innermost edge  
 599 of the CsI calorimeter was rejected. This cut is also called the Fiducial Cut. The outer  
 600 boundary requires the radius of the photon hit position within 850 mm,  $R_\gamma < 850$  mm,  
 601 while the inner boundary requires the photons 150 mm away from the square beam hold,  
 602  $\min\{|x_\gamma|, |y_\gamma|\} > 150$  mm.

603 **Minimum Cluster Distance**

604 If two-photon clusters are too close to each other, the EM shower may overlap, and the  
 605 energy reconstruction will be incorrect, or the two photons may be misidentified as one  
 606 photon. To avoid this situation, a minimum cluster distance of 150 mm was required.

607 **5.2.3  $K_L^0$  Selection**

608 Figure 5.2 and 5.3 show the distribution of the  $K_L^0$  selection variables for the  $K_L^0 \rightarrow 3\pi^0$   
 609 decay. The  $K_L^0$  selection cuts include the  $\chi^2$  of the decay Z,  $\Delta T$  of the vertex,  $K_L^0$  decay  
 610 vertex Z,  $K_L^0$  mass,  $K_L^0 P_T$ ,  $\Delta\pi^0$  mass, and  $K_L^0 \Delta Z_{vtx}$ .

611  $\chi_z^2$

612 To make sure the reconstructed  $\pi^0$  is good quality, the  $\chi_z^2$  cut was applied. The  $\chi_z^2$  could  
 613 indicate the goodness of the photon pair to the  $\pi^0$  reconstructed, defined in Equation

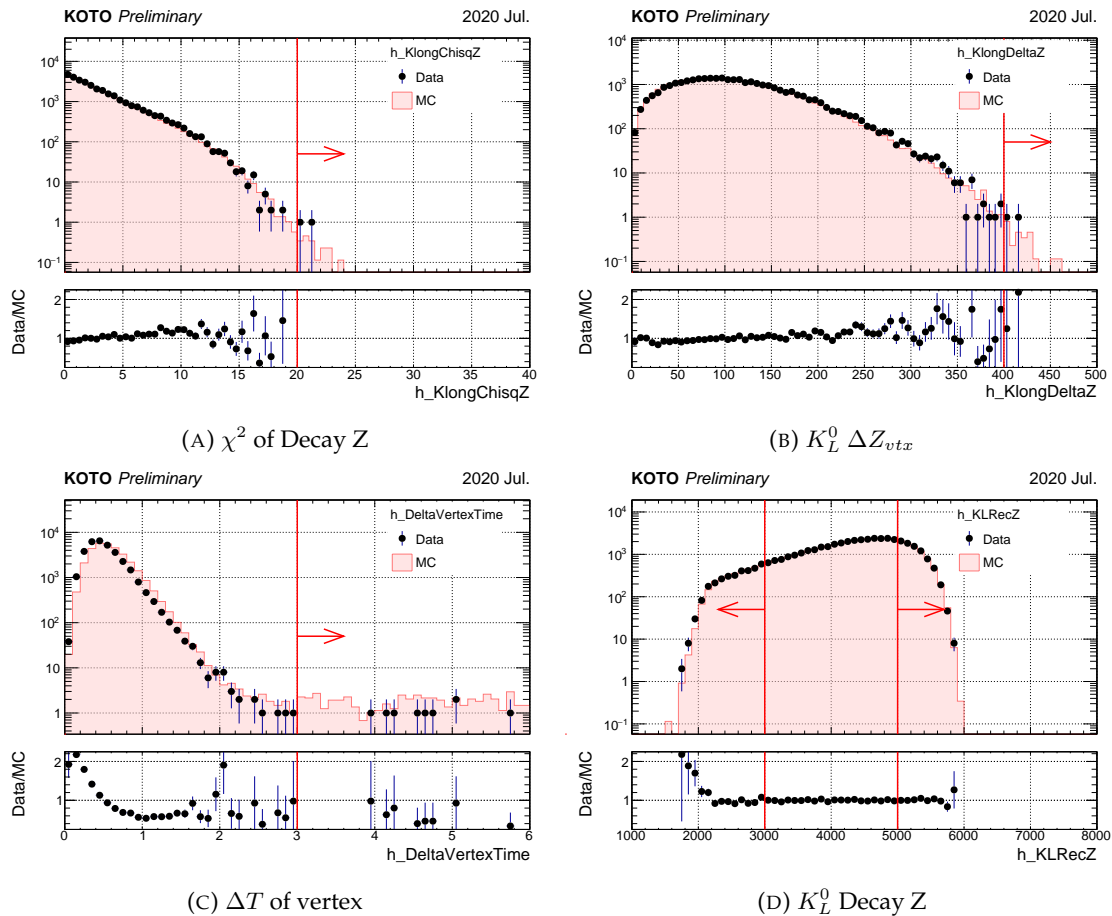


FIGURE 5.2: Distribution of the  $K_L^0$  selection variables for the  $K_L^0 \rightarrow 3\pi^0$  decay. The photon and  $K_L^0$  selection cuts are applied except for the variable shown in the plot. The black point shows the data, and the fill histogram shows the Monte Carlo simulation. The red arrow indicates the cut-off value of the variable.

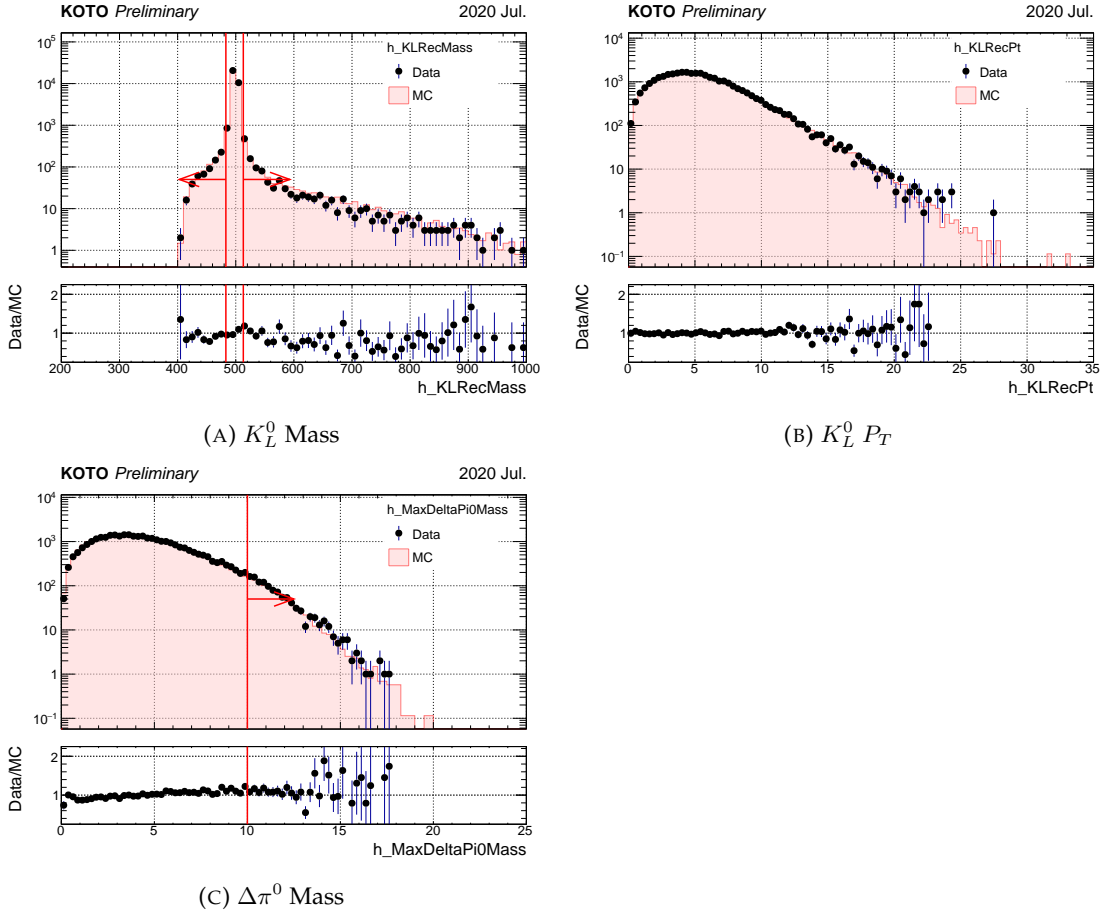


FIGURE 5.3: Distribution of the  $K_L^0$  selection variables for the  $K_L^0 \rightarrow 3\pi^0$  decay. The photon and  $K_L^0$  selection cuts are applied except for the variable shown in the plot. The black point shows the data, and the fill histogram shows the Monte Carlo simulation. The red arrow indicates the cut-off value of the variable.

614 3.13. This cut was used to ensure the consistency of the reconstructed  $\pi^0$  vertex, and the  
615  $\chi_z^2$  was required to be less than 20.

### 616 $K_L^0 \Delta Z_{vtx}$

617 The  $\Delta Z_{vtx}$  is defined as the maximum difference between the reconstructed  $\pi^0$ 's, as  
618 shown in Equation 5.1. This cut is also used to ensure the consistency of the reconstructed  
619  $\pi^0$  vertexes. The  $\Delta Z_{vtx}$  was required to be less than 400 mm.

$$\Delta Z_{vtx} = \max \left( |Z_{vtx}^i - Z_{vtx}^j| \right) \quad (5.1)$$

### 620 Maximum Difference of Vertex Timing ( $\Delta T_{vtx}$ )

621 The vertex timing of each photon cluster that belongs to the same event should be con-  
622 sistent with each other. The maximum vertex timing difference between reconstruc-  
623  $K_L^0$  and each photon cluster was required to be less than 3 ns.

624  **$K_L^0$  Decay Vertex Z ( $Z_{vtx}$ )**

625 The Decay vertex of the  $K_L^0$  was required within the decay volume of the KOTO detector,  
 626  $3000 \text{ mm} \leq Z_{vtx} \leq 5000 \text{ mm}$ .

627  **$K_L^0$  Mass**

628 In the reconstruction of  $K_L$ , the invariant mass of photons was required to be within  
 629  $\pm 15 \text{ MeV}/c^2$  of the nominal  $K_L$  mass of  $497.614 \text{ MeV}/c^2$ [22]. This criterion significantly  
 630 reduces event contamination from mispairing in both the  $K_L \rightarrow 3\pi^0$  analyses. It also  
 631 minimizes the interference of  $K_L \rightarrow 3\pi^0$  decays in the analysis.

632  **$K_L^0 P_T$**

633 In the normalization study,  $K_L^0$  should not have missing particles, so the reconstructed  
 634 transverse momentum ( $P_T$ ) of the  $K_L^0$  is expected to be small. The  $P_T$  of the  $K_L^0$  was  
 635 required to be less than  $50 \text{ MeV}/c$ .

636  **$\Delta\pi^0$  Mass**

637 The  $\Delta\pi^0$  mass is the difference between the reconstructed  $\pi^0$  mass and the nominal  $\pi^0$   
 638 mass of  $134.9766 \text{ MeV}/c^2$ [22]. The  $\pi^0$  mass was calculated by the reconstructed  $K_L^0$  de-  
 639 cay vertex. A large  $\Delta\pi^0$  mass indicates a bad pairing of the photon cluster, which may  
 640 come from the accidental hit. The reconstructed  $\Delta\pi^0$  mass was required to be within  
 641  $\pm 10 \text{ MeV}/c^2$  of the nominal  $\pi^0$  mass.

642 **5.2.4 Veto Cut**

643 All the veto cuts applied to the yield study are the same as the veto cuts used in the  
 644  $K_L^0 \rightarrow \pi^0\nu\bar{\nu}$  analysis[15]. The summary of the veto cut is shown in Table 5.2.

645 In the following section, a detailed explanation of the Veto Cut is shown.

646 **Isolated Crystal Veto**

647 An isolated crystal hit very close in time to the photon clusters are possibly comes from  
 648 the same  $K_L^0$  decay. To reject this kind of background, a timing window of  $\pm 10 \text{ ns}$  of the  
 649 nearest photon cluster timing is required in this veto. A multistep cut based on the hit  
 650 Energy(E) and Distance(D) from the closest cluster is applied, as the following equation:

$$\begin{cases} E > 10 \text{ [MeV]} & , \text{if } D < 200 \text{ [mm]} \\ E > 10 - \frac{7 \cdot (D - 200)}{400} \text{ [MeV]} & , \text{if } 200 \leq D \leq 600 \text{ [mm]} \\ E > 3 \text{ [MeV]} & , \text{if } D > 600 \text{ [mm]} \end{cases} \quad (5.2)$$

651 As shown in Figure 5.4, a higher energy threshold is required for the isolated crystal  
 652 to hit nearer to the cluster, to bypass the shower propagation effect.

TABLE 5.2: Summary of the veto cut

Veto Counter	Energy Threshold	Timing Window
FB	1 MeV	51ns
NCC and HINEMOS	1 MeV	40ns
MB	1 MeV	20ns
IB	1 MeV	20ns
MBCV	0.5 MeV	60ns
IBCV	0.5 MeV	60ns
CV	0.2 MeV	20ns
LCV	0.6 MeV	30ns
CSI (isolated crystal)	see Sec. 5.2.4	20ns
CSI (extra cluster)	see Sec. 5.2.4	20ns
OEV	1 MeV	20ns
CC03	3 MeV	30ns
CC04, CC05, CC06 (CSI crystal)	3 MeV	30ns
CC04, CC05, CC06 (plastic scintillator)	1 MeV	30ns
BPCV	1 MeV	24ns
BHCV <sup>1</sup>	221 eV	25ns
BHPV <sup>2</sup>	2.5 p.e.	15ns
BHGC <sup>3</sup>	2.5 p.e.	15ns

<sup>1</sup> BHCV requires hits in more than two modules.

<sup>2</sup> BHPV requires hits in more than three consecutive modules.

<sup>3</sup> BHGC veto accepts the number of equivalent photons instead of energy.

### 653 Extra Cluster Veto

654 A cluster hit in the CsI calorimeter that is not associated with the  $\pi^0 \rightarrow \gamma\gamma$  decay is considered  
 655 an extra cluster. If the timing of the extra cluster is within  $\pm 10$  ns of the reconstructed  $\pi^0$   
 656 vertex time, it is considered as a background and rejected.

## 657 5.3 Yield Estimation

658 The Yield of the  $K_L^0$  ( $Y$ ) in the data set is defined by the following equation:

$$Y = \frac{N_{mode}}{\mathcal{BR}_{mode} \times A_{mode}} \quad (5.3)$$

659 where  $N_{mode}$  is the number of events,  $\mathcal{BR}_{mode}$  is the branching ratio, and  $A_{mode}$  is the  
 660 acceptance. The mode could be any decay channel of the  $K_L^0$ . The acceptance( $A_{mode}$ ) can  
 661 be evaluated by the Monte Carlo simulation, as the following equation:

$$A_{mode} = \frac{N_{remaind}}{N_{gen}} \quad (5.4)$$

662 where  $N_{remaind}$  is the number of events that pass the event selection, and  $N_{gen}$  is the  
 663 number of generated  $K_L^0$  decays. And because the  $K_L^0$  yield is proportional to the number  
 664 of protons on target (POT), the  $K_L^0$  flux (F) can be defined as the yield per POT, as shown

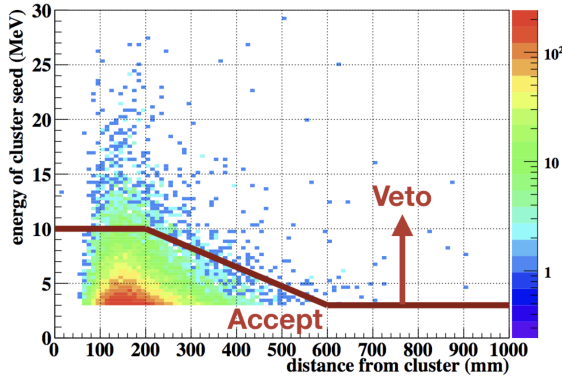


FIGURE 5.4: Distribution of isolated crystal hit energy( $E$ ) vs. its distance( $D$ ) from the nearest cluster. The red line shows the cut based on Equation 5.2. The sample was obtained from the  $K_L^0 \rightarrow \pi^0 \nu \bar{\nu}$  Monte Carlo simulation.[23]

665 in the following equation:

$$F = \frac{Y}{\text{POT}} \quad (5.5)$$

666 As mentioned in Section 5.1, the normalization trigger was used to be the data sample.  
 667 Because the normalization trigger was taken simultaneously with the physics trigger, the  
 668  $K_L^0$  yield is the same as the physics trigger. Therefore, the  $K_L^0$  yield evaluated by the  
 669 normalization trigger can be used directly in the physics analysis.

670 In this study, the  $K_L^0$  yield was estimated by the  $K_L^0 \rightarrow 3\pi^0$  decay. All the kinematic  
 671 cuts introduced in Section 5.2.2 and 5.2.3 and the veto cuts summarized in Table 5.2 were  
 672 imposed.

### 673 5.3.1 Estimation by $K_L^0 \rightarrow 3\pi^0$ Decays

674 Figure 5.6 and 5.7 show the distribution of the kinematic variables for the  $K_L^0 \rightarrow 3\pi^0$   
 675 decay after imposed all selection cuts referred in Section 5.2. The purity of the  $K_L^0 \rightarrow 3\pi^0$   
 676 decay is high because there is no other  $K_L^0$  decay mode that can mimic the six-cluster  
 677 signature on CSI. The most discrepancy comes from the statistics of the special physics  
 678 data is not enough to match the Monte Carlo simulation.

679 Figure 5.5 shows the beam shape of the x and y projection at the exit of the second  
 680 collimator. The beam core shows a good agreement between the data and the Monte  
 681 Carlo simulation.

## 682 5.4 Summary of $K_L^0$ Yield Estimation

683 The  $K_L^0$  yield of the special physics run was estimated to be  $1.29 \times 10^{10}$  by the  $K_L^0 \rightarrow 3\pi^0$   
 684 decay. The systematic uncertainty will be considered in the Single Event Sensitivity (SES)  
 685 study in Section 6.4.1.

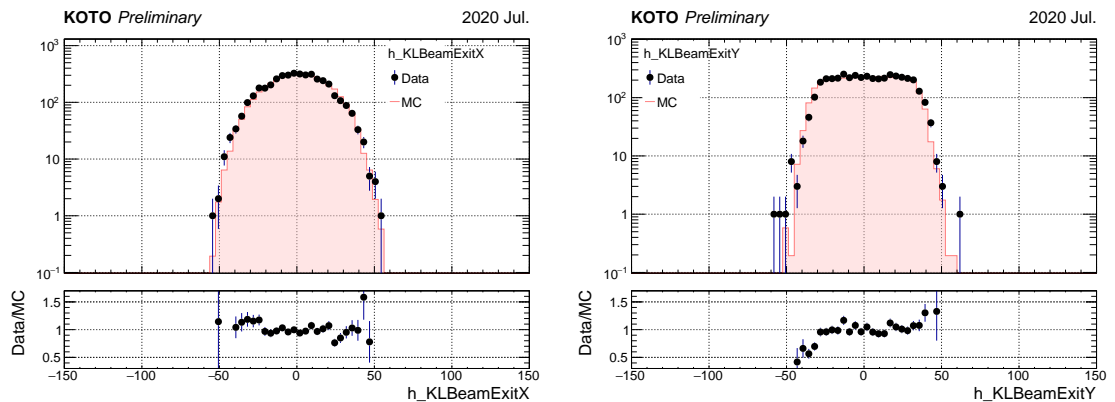


FIGURE 5.5: Beam profile at the exit of the second collimator via the  $K_L^0 \rightarrow 3\pi^0$  decay analysis. All the selection cuts are imposed. Filled histograms are predicted by the Monte Carlo simulation.

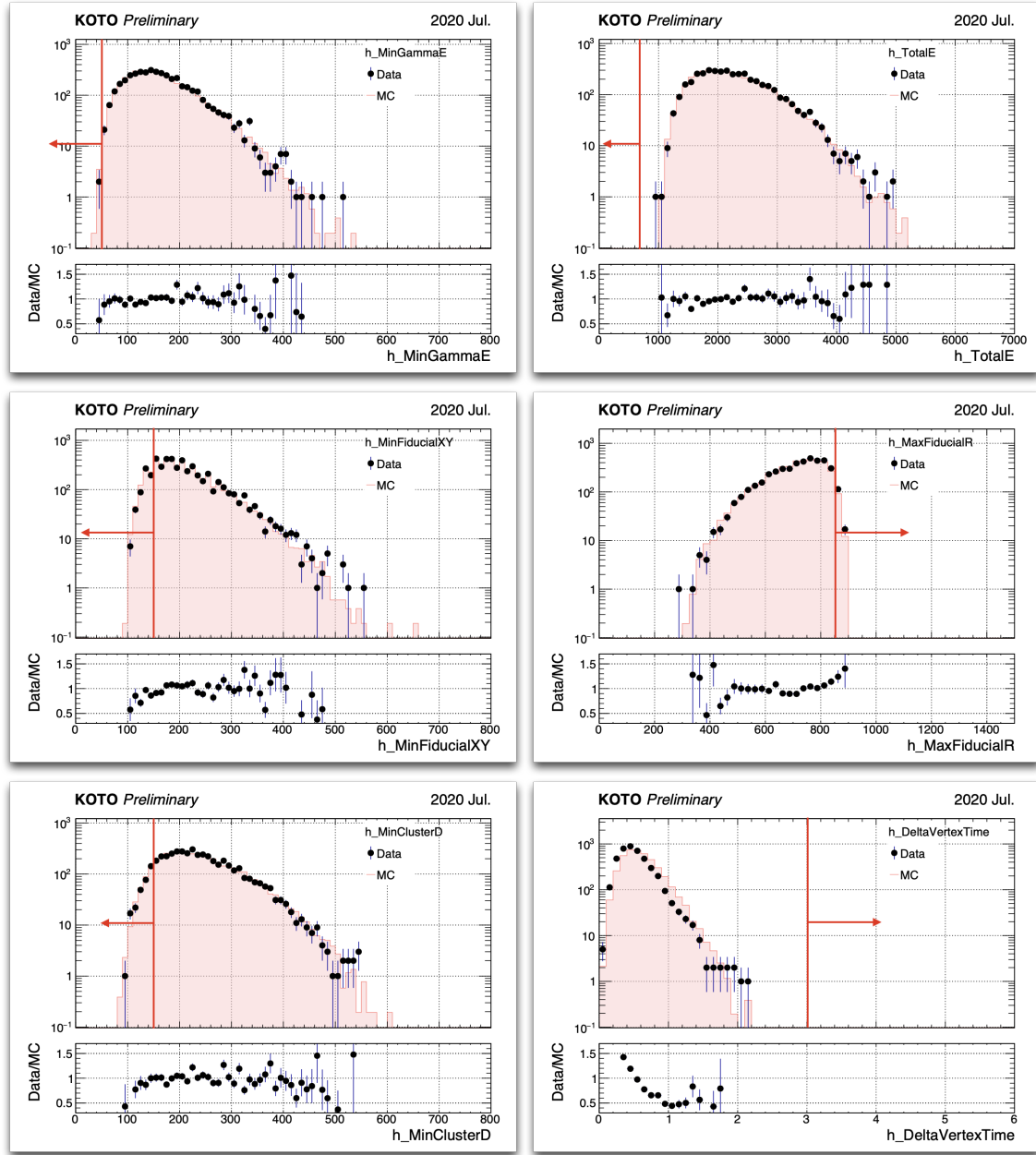


FIGURE 5.6: Distribution of the kinematic variables for the  $K_L^0 \rightarrow 3\pi^0$  decay. All the selections are applied except the variable shown in the plot. The black point shows the data, and the fill histogram shows the Monte Carlo simulation. The red arrow indicates the cut-off value of the variable.

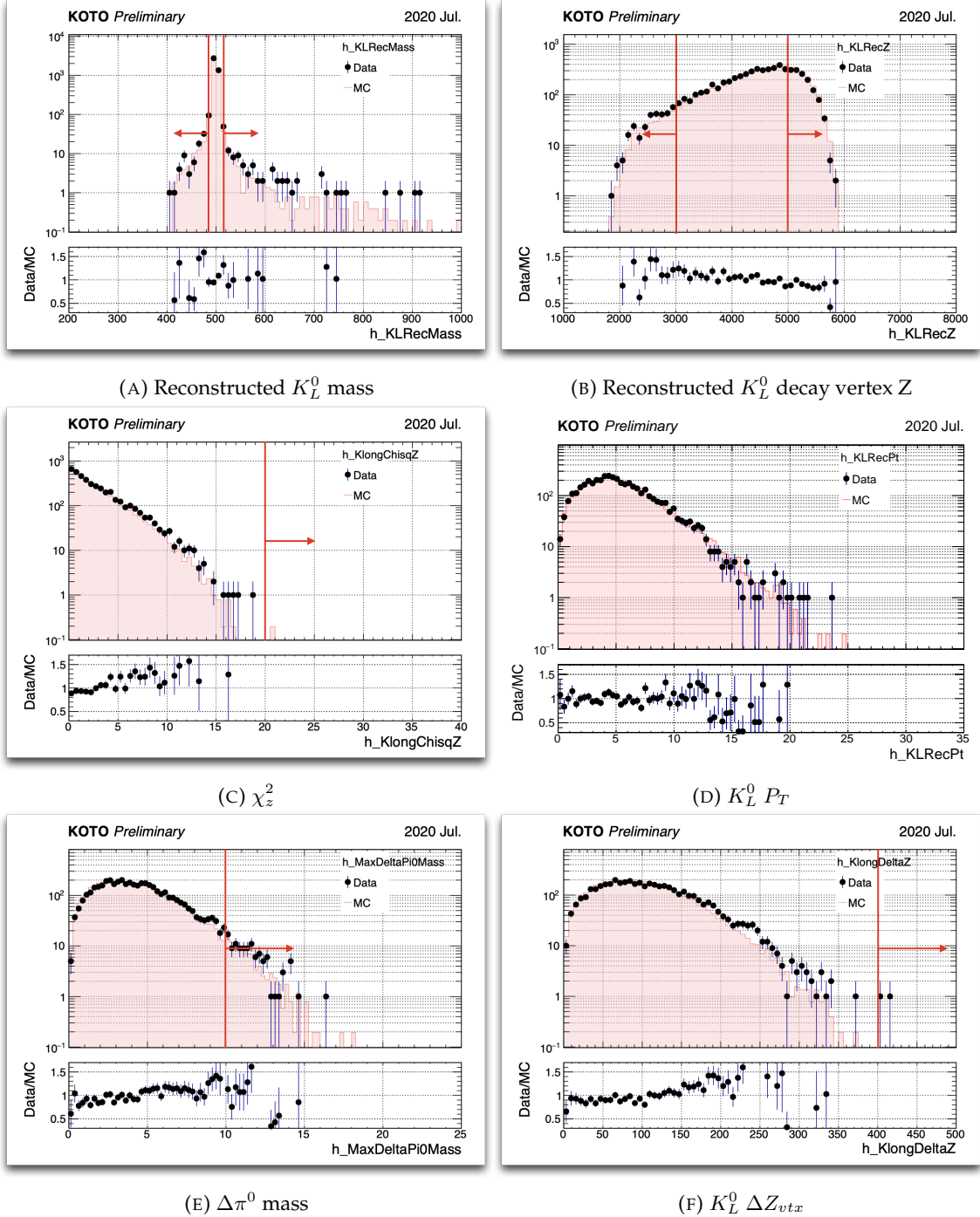


FIGURE 5.7: Distribution of the kinematic variables for the  $K_L^0 \rightarrow 3\pi^0$  decay. All the selections are applied except the variable shown in the plot. The black point shows the data, and the fill histogram shows the Monte Carlo simulation. The red arrow indicates the cut-off value of the variable.



686 **Chapter 6**

687 **Analysis of  $K_L \rightarrow \gamma\bar{\gamma}$**

688 The goal of the  $K_L^0 \rightarrow \gamma\bar{\gamma}$  analysis is to estimate the branching ratio ( $\mathcal{BR}$ ) of this decay,  
689 we took a 2-hour special run with a single cluster trigger in 2020. The distinctive signal  
690 signature of  $K_L^0 \rightarrow \gamma\bar{\gamma}$  manifests as a singular photon hit on the CsI calorimeter, devoid  
691 of any in-time hits on other detectors.

692 Employing a blind analysis method as explained in Section 1.3, we define a specific  
693 region, characterized by energy deposition  $800 \text{ MeV} < E_\gamma < 3000 \text{ MeV}$  and a spatial  
694 constraint of  $300 \text{ mm} < H_{XY} < 850 \text{ mm}$ , where  $H_{XY}$  denotes the maximum distance  
695 between the hit location and the center of the CsI crystal along the x and y axes. The  
696 signal region has to be within the blind region and has been optimized.

697 Our principal objective revolves around suppressing background noise and accentuating  
698 signal events through event selection. Subsequently, we estimate the residual back-  
699 ground events within the signal region post-selection. Under the assumption of negli-  
700 gible background noise, we calculate the Single Event Sensitivity (SES) to estimate the  
701 branching ratio upon observing signal events within the defined signal region. The SES,  
702 representing the reciprocal of the product of the total  $K_L^0$  yield and the acceptance of  
703 signal decays, is expressed mathematically as:

$$\text{SES} = \frac{1}{Y \times A_{sig}} \quad (6.1)$$

704 Here,  $Y$  represents the  $K_L^0$  yield, and  $A_{sig}$  signifies the signal acceptance. The branching  
705 ratio ( $\mathcal{BR}$ ) is then inferred from SES and the observed number of signal events ( $N_{sig}$ )  
706 within the signal region, as articulated by:

$$\mathcal{BR} = \text{SES} \times N_{sig} \quad (6.2)$$

707 However, when background contributions cannot be negligible, a statistical methodology  
708 becomes imperative to ascertain the upper and lower bounds of signal event counts.  
709 The background level ( $N_{bg}$ ) is estimated through two approaches in this study. For  $K_L$   
710 decay backgrounds, Monte Carlo simulations are employed to evaluate  $N_{bg}$ , defined by:

$$N_{bg} = Y \times \mathcal{BR}_{bg} \times A_{bg} \quad (6.3)$$

711 Where  $\mathcal{BR}_{bg}$  represents the branching ratio of specific background decays (e.g.,  $K_L \rightarrow$   
 712  $2\gamma$ ), and  $A_{bg}$  denotes the acceptance corresponding to this background decay. For neu-  
 713 tron backgrounds, a dedicated neutron data run is utilized, employing a data-driven  
 714 approach for background-level evaluation through normalization against the neutron-  
 715 dominant region between physics data and neutron data sample. Upon combining all  
 716 background sources, a prediction of the background level within the signal region is de-  
 717 termined. After an examination of reliability through the side-band region, uncover the  
 718 blind region.

719 This chapter unfolds with a presentation of the event selection criteria, followed by  
 720 a discussion on background suppression methodologies. Subsequently, the reliability  
 721 of our analysis is assessed through a comparison between physics data and simulation  
 722 results in the side-band region. The computation of background levels and SES is then  
 723 detailed. With the final estimation in hand, we will proceed to open the box and the  
 724 interpretation of the statistical result will be presented at the latest.

## 725 6.1 Data Set

726 As mentioned in the above section, for this analysis a special 2-hour run was taken in  
 727 June 2020 (RUN85). In this special run, a single cluster trigger was adopted as the physics  
 728 data, the energy threshold was set at 300 MeV with online veto and a pre-scale factor 1. To  
 729 normalize this run, a normalization trigger is also accepted, this trigger does not contain  
 730 the cluster number trigger, and only adopts CV as the online veto, with a pre-scale factor  
 731 of 13. The POT of the 2-hour special is around  $5.03 \times 10^{-6}$  with the total  $1.29 \times 10^{10}$   
 732 number of  $K_L^0$  enter KOTO detector, as shown in Chapter 5.

733 For the neutron background study, a neutron sample run was taken. As Section 4.7  
 734 mentions, the GEANT4 MC toolkits cannot simulate the neutron interaction correctly, so  
 735 the data-driven method was adopted to do the neutron background study. Ideally, for  
 736 the single cluster study, a single cluster trigger neutron should be used in the study. Fol-  
 737 lowing this thought, a special single cluster Z0-Al run was taken in RUN85. However,  
 738 after further study, we notice that the single cluster Z0-Al run cannot stand the neutron  
 739 sample. Because we don't have a good method to purify the neutron event from the Z0  
 740 data. Therefore, as a compromise, we use the 2-cluster trigger Z0 run in RUN85 which is  
 741 taken for the  $K_L^0 \rightarrow \pi^0 \nu\bar{\nu}$  decay study. The mechanism of the 2-cluster neutron event is  
 742 that a neutron hits the CsI calorimeter and generates a new hadron through the hadronic  
 743 interactions, as shown in Figure 6.1. Because there are two clusters on the CsI, the re-  
 744 construction was possible. Consequently, use the kinematic variable to select the neutron  
 745 event, then a pure neutron sample data set was obtained. For the single cluster study,  
 746 only the cluster with higher energy was selected because the primary neutron usually  
 747 has higher energy than the second one.

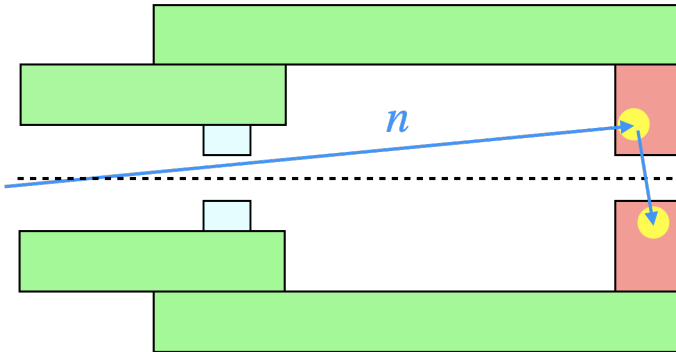


FIGURE 6.1: The mechanism of the 2-cluster neutron event in the Z0 run.

Because the neutron flux is unable to be obtained, the background was normalized by the number of events in the neutron-dominated region in the neutron study. In this study, we adopt all Z0 data in RUN85, and the scale factor obtained by the normalization was around 1.6. This means the statistic of the neutron sample is far away to compare with physics data, it will behave on the statistical uncertainty.

## 6.2 Single Cluster Event Selection

The event selection included trigger cuts, kinematic cuts, and veto cuts. The trigger cuts were designed to mimic the online trigger effect, while the kinematic cuts and veto cuts were implemented to suppress background noise. The kinematic cuts were based on the reconstruction quantities of the photon cluster, while the veto cuts were just the criteria of hit on the veto counters. In the single cluster study, the signal significance of  $K_L \rightarrow \gamma\bar{\gamma}$  is only one photon cluster hit on the CsI calorimeter. And other vetoes keep silent in time. Which means a very loose condition for hitting events. It is also a challenge for this study.

### 6.2.1 Trigger Selection

The online trigger effect is the source of the difference between the collected data and the Monte Carlo simulation. To mimic the online trigger effect and ensure the consistency of the data and MC simulation, two trigger selections were implemented: the trigger timing cut and the total energy cut.

- **Timing window**

The online trigger will reject all events with any on-time veto hit, thus a trigger timing window as shown in Figure 6.2 is required to eliminate the online trigger effect. In the real data taking, due to the 8-ns clock dead time, the real physics data timing distribution will be wider than the Monte Carlo simulation. A wide enough timing window is selected to cover the distribution inconsistency between the data and the MC simulation.

- **Total Energy**

The offline energy cut should be larger than the online ET threshold to eliminate the

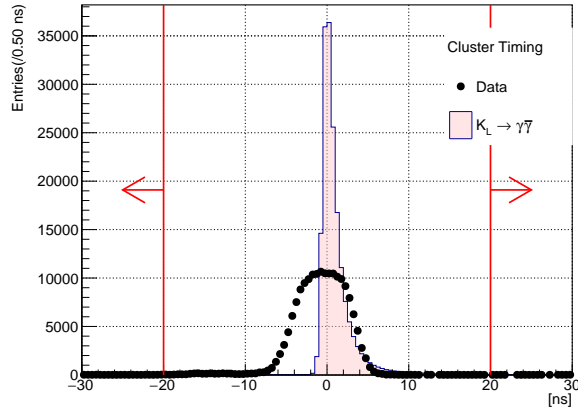


FIGURE 6.2: Distribution of cluster timing after relative timing correction. The dot is from real physics data, and the filled histogram is the MC simulation. The red arrow is the cut-off region.

776 online ET trigger effect. The online ET threshold of 300 MeV was required in the  
 777 special run, Thus, the offline energy cut is set as 500 MeV. As shown in the Figure  
 6.3, the signal acceptance is 91.0%

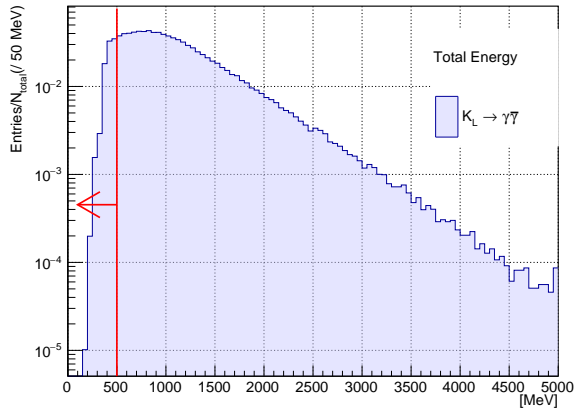


FIGURE 6.3: Distribution of total energy from Monte Carlo simulation. The histogram area is normalized to 1. The red arrow is the cut-off region.

778

## 779 6.2.2 Kinematic Cuts

780 The  $K_L \rightarrow \gamma\bar{\gamma}$  decays require only one photon cluster on the CsI calorimeter. Therefore,  
 781 the reconstruction of the mother particle is not possible, and also some variables based  
 782 on multiple photon clusters will be absent, such as the vertex position, cluster distance,  
 783 and KL kinematic quantities. As kinematic constraints are lacking, kinematic selection is  
 784 determined by only two variables: the photon hit position and photon energy.

- 785 • **Innermost and Outermost Photon Hit Position**

786 To prevent the edge of the calorimeter from affecting cluster reconstruction, any  
 787 event that hits the boundary will be removed. Based on the geometry of the calorime-  
 788 ter, the outer boundary is evaluated using a radius of hit position,  $R_\gamma$ , while the  
 789 inner boundary is evaluated using the maximum of the absolute values of x and y  
 790 of the photon hit position,  $\max\{|x_\gamma|, |y_\gamma|\}$ . The inner boundary is set as a  $300 \times 300$

791 mm<sup>2</sup> box, while the outer boundary is a circle with a radius of 850 mm, as shown  
in Figure 6.4.

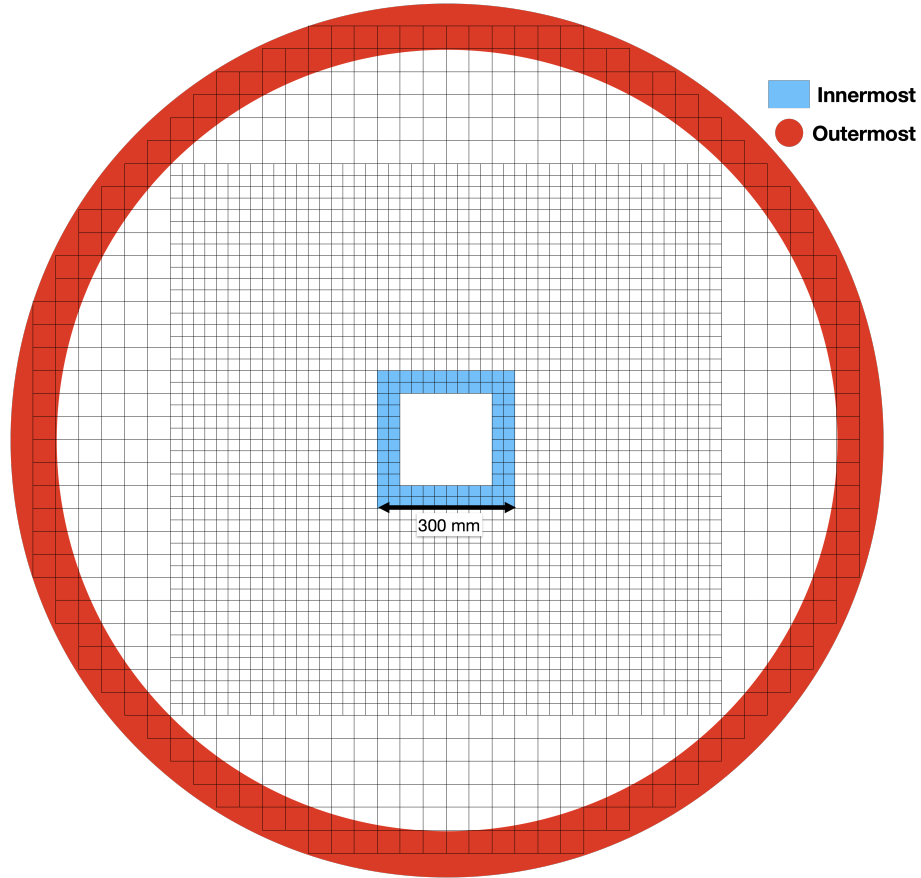


FIGURE 6.4: An upstream view of the CsI calorimeter. The red region is the outermost boundary, while the blue region is the innermost boundary.

792

793 • **Photon energy**

794

795

796

Because of the 1 cluster study, the photon energy is almost equivalent to the total energy. Therefore, simply required photon energy to be larger than 500 MeV, which is the same as the total energy cut.

797

### 6.2.3 Veto Cuts

798

799

800

801

802

803

804

805

806

Veto counters are the primary tool for Kaon decay background suppression in the KOTO experiment. The veto hits within the veto timing window and above the veto energy threshold will be tagged as an in-time veto hit. The event with any in-time veto hits will be treated as a background event and rejected. To determine a veto cut, the veto timing window and the energy threshold were required. The energy threshold was simply selected over the online veto and within the precision of the veto counter. The veto timing for veto hits is defined as talk in Section 3.4. To determine the reject window of the veto timing a timing study of each veto counter is required. First, the nominal timing should be determined, the hit close to the nominal timing should be considered as a background

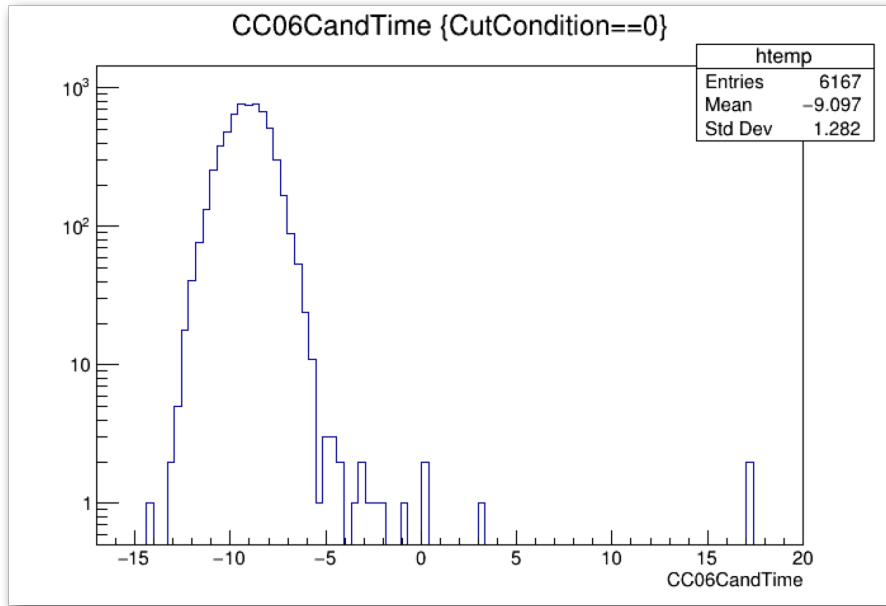


FIGURE 6.5: Distribution of veto timing of CC06.

807 hit. Then determined the exact reject window of this veto, because the hit could be pro-  
 808 duced by the accidental hit not from the  $K_L^0$  decay source. The window decision should  
 809 consider the signal loss from the accidental hits.

810 In some veto counters, the source of the veto is predominantly the  $K_L^0$  decay, which  
 811 results in a Gaussian-like timing distribution, as an example shown in Figure 6.5. For  
 812 these types of veto counters, the decision on the timing window is straightforward: it  
 813 involves selecting a range of  $\pm$  a few nanoseconds around the peak position. The width  
 814 of this window is determined based on the shape of the distribution.

815 However, in some veto counters especially for those surrounding the decay volume,  
 816 the accidental hits are mixed with the background hit. In the following subsection, the  
 817 veto study for these veto counters will be discussed.

### 818 FBAR and NCC

819 The veto timing is defined by the Equation 3.26 The FBAR and NCC are placed upstream  
 820 of the decay volume, the distribution of timing is shown in Figure 6.6. The mechanisms  
 821 of the hits can be categorized into these three types.

- 822 • **Upstream decays**

823 If a  $K_L^0$  decays inside the FBAR chamber, the photon product can hit the FBAR or  
 824 NCC, and the timing accumulated is the nominal time. In the Figure 6.6, is the event  
 825 in decay vertex Z less than 2719 mm region. For NCC the veto timing in this region  
 826 does not have a large variant which is because the  $K_L^0$  decay before the NCC and  
 827 the  $(\Delta z - D)$  in Equation 3.26 is almost a constant and equivalent to the distance  
 828 between NCC and CsI, regardless the decay position. However, because the  $K_L^0$

829 decays inside the FBAR, and it has a large volume, the  $(\Delta z - D)$  will variant in  
 830 a large range depending on the decay position.

831 In Figure 6.6, the veto timing of FBAR is broken into two peaks around the nominal  
 832 time, which is because the NCC covers a part of the FBAR detector. In the Figure  
 833 6.6a can show the agreement.

834 • **Backward hit**

835 When a  $K_L^0$  decay in the decay volume, the photon could fly backward and hit the  
 836 NCC and FBAR. Based on the Equation 3.26, the  $(\Delta z - D)/c$  term will be a variant  
 837 and the veto timing will depend on the decay vertex. However, the variate of this  
 838 term is controllable,

$$\Delta z - D \approx \Delta z - (L - \Delta z) = 2\Delta z - L \quad (6.4)$$

$$T_{veto}(\Delta z) \approx \frac{2}{c}\Delta z + T_{mod} - T_{CsI} - L/c \quad (6.5)$$

839 where  $L$  represents the distance between veto and CsI. Equation 3.26 could be seen  
 840 as a function to  $\Delta z$  with a slope  $2/c$ . Which explained the slope of the backward hit  
 841 distribution in Figure 6.6a and 6.6b

842 • **CsI backsplash**

843 As shown in Figure 6.6a and 6.6b, a set of events with a veto timing independent  
 844 of the decay vertex  $z$ . This phenomenon is called "backsplash" which is because the  
 845 calorimeter did not consume all the EM shower but splashed upstream. Because  
 846 the distance of the trajectory is constant, the veto timing will also be constant.

847 Based on these three mechanisms, only the CsI backsplash is the fake signal and the  
 848 other two are the backgrounds. Therefore, the veto timing window for NCC and FBAR  
 849 excludes the backsplash peak, as shown in Figure 6.6c and 6.6d.

## 850 6.3 Background Suppression

851 There are two main category background sources in this analysis:  $K_L$  decay events and  
 852 Hadronic cluster. Besides these two main background sources, we will also discuss the  
 853 other background sources that we study in this analysis, such as Charge Kaon decays,  
 854 NCC background, and Halo Kaon backgrounds. In the following section, we will talk  
 855 about the background suppression strategy for each category.

### 856 6.3.1 $K_L$ Decay Background

857 In this analysis, we have studied the major three  $K_L^0$  neutral decay channels, like  $K_L^0 \rightarrow$   
 858  $3\pi^0$ ,  $K_L^0 \rightarrow \pi^0\pi^0$ , and  $K_L^0 \rightarrow 2\gamma$ . And also the  $K_{e3}^0$ ,  $K_{\mu 3}^0$ , and  $K_L^0 \rightarrow \pi^+\pi^-\pi^0$ , which is the  
 859 charge decay channel with a large branching ratio.

860 There are 3 kinds of possible mechanisms from  $K_L^0$  decays were found:

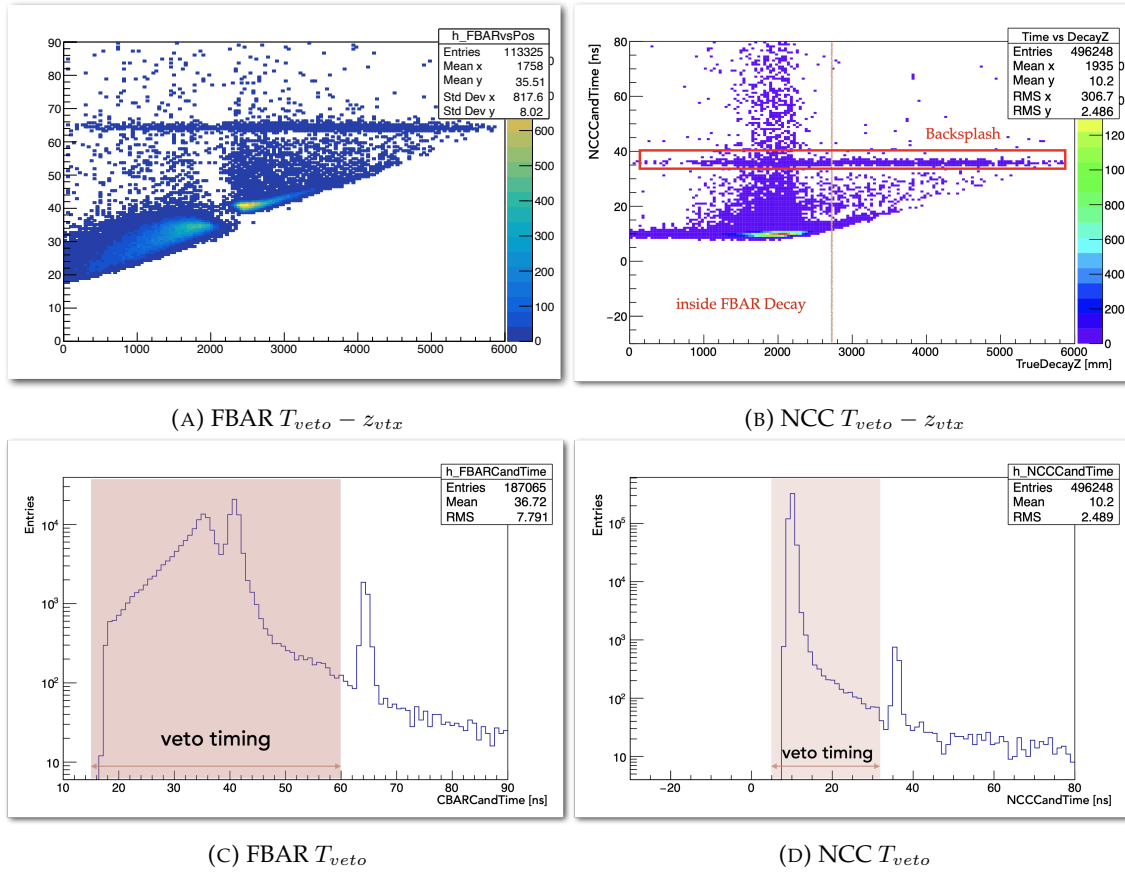


FIGURE 6.6: Temporary plots of FBAR and NCC

- **Missing photon**

One photon hits the CsI, but other particles hit the dead material of the KOTO detector or missing in the beam hole.

- **Upstream decay**

$K_L^0$  decay upstream of the FBAR, one photon hits the CsI, and the other photon missing outside the detector.

- **Fusion cluster**

The decay position along the Z-axis ( $Z_{vtx}$ ) is too close to the CsI, all decay products hit the nearby crystal and are noted as a single cluster by the clustering process. As shown in Figure 6.9

In this section, all the studied  $K_L^0$  backgrounds will be discussed. All the Monte Carlo simulations were applied the accidental overlay.

873     **$K_L^0 \rightarrow 2\gamma$  Background**

874    Because of the extreme hermetic of the KOTO detector, the possibility of missing multiple  
875    particles is very low. And with our powerful charge veto counter, it is also very difficult

876 to miss a charged particle. Therefore,  $K_L^0 \rightarrow 2\gamma$  decay with one missing photon will be  
 877 the primary  $K_L^0$  decay background in this study.

878  $K_L^0 \rightarrow 2\gamma$  background consists of two mechanisms, missing photon and upstream de-  
 879 cay.  $K_L^0 \rightarrow 2\gamma$  has very similar signature with the  $K_L^0 \rightarrow \gamma\bar{\gamma}$ , the only difference is another  
 880 photon is visible. This means if the other photon of  $K_L^0 \rightarrow 2\gamma$  is missing detecting, this  
 881 event will be an ineliminable background in this study. The upstream decay mechanism  
 882 is also having a missing photon. But its decay position is upstream of the FBAR, which  
 883 highly constrains the hit radius ( $H_{XY}$ ) of the cluster. Based on the geometry calculation  
 884 as shown in Figure 6.7, the maximum  $H_{XY}$  of the cluster of upstream decay is 265 mm,  
 885 which is outside the signal region.

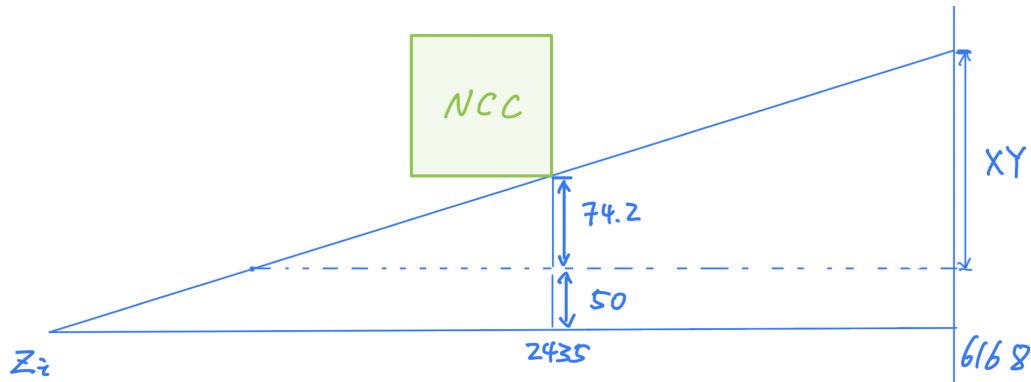


FIGURE 6.7: The schematic geometry diagram of the mechanism of the upstream decay back-  
ground.

886 Figure 6.8 shows the result of  $K_L^0$  selection. A background level of  $1.09 \pm 0.12$  is esti-  
 887 mated in the signal region.

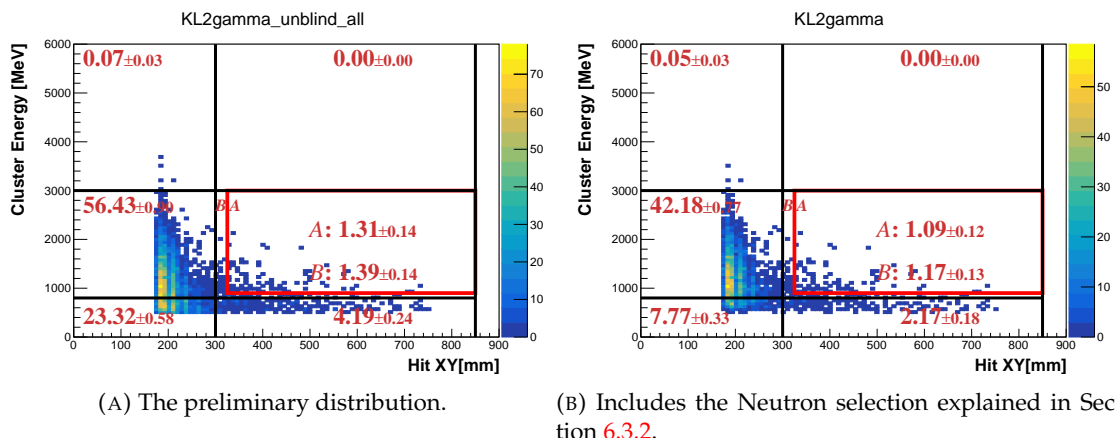


FIGURE 6.8:  $E_\gamma - H_{XY}$  distributions of scattered  $K_L^0 \rightarrow 2\gamma$  decays with various cut. The red frame indicates the signal region. The red number indicates the background level in each region.

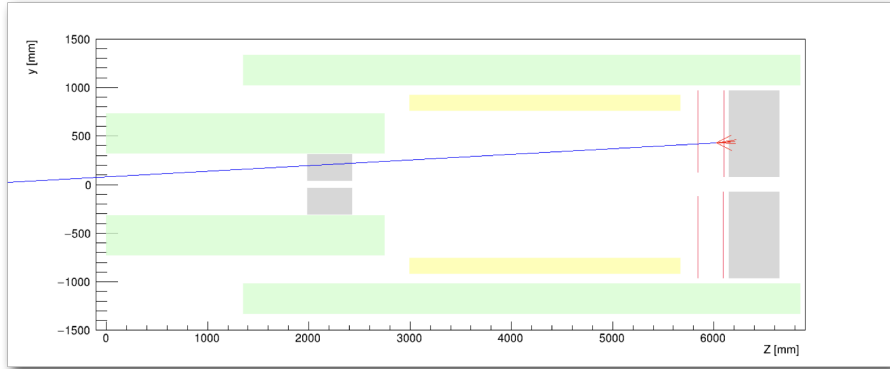


FIGURE 6.9: The schematic geometry diagram of the mechanism of the fusion cluster background.

### 888 Other $K_L^0$ decay Backgrounds

889 Besides the  $K_L^0 \rightarrow 2\gamma$  background, the other  $K_L^0$  decay backgrounds are also studied in  
 890 this analysis. Such as  $K_L^0 \rightarrow 3\pi^0$ ,  $K_L^0 \rightarrow \pi^0\pi^0$ ,  $K_{e3}^0$ ,  $K_{\mu 3}^0$  and  $K_L^0 \rightarrow \pi^+\pi^-\pi^0$ . After the  
 891 event selection explained in Section 6.2 and 6.3.2, the event inside the signal region of all  
 892 decays except  $K_L^0 \rightarrow 2\gamma$  is all rejected. All the three mechanisms mentioned above existed  
 893 in these decays. The missing photon is also an ineliminable background, but because the  
 894 decay products are much more than the  $K_L^0 \rightarrow 2\gamma$ , the missing photon background is  
 895 negligible. And the upstream decay background has the same geometry constraint as the  
 896  $K_L^0 \rightarrow 2\gamma$ .

897 The fusion cluster mechanism is the most challenging one because the usual method  
 898 to reject this kind of background is to restrict the decay vertex Z ( $Z_{vtx}$ ) position in a  
 899 reasonable region. However, in this study, the  $Z_{vtx}$  is not available due to the lack of  
 900 kinematic variables. Therefore, we have to distinguish the fusion cluster from the single  
 901 cluster by the cluster shape.

902 The fusion cluster will have a wider shape than the single cluster because the fusion  
 903 cluster is the combination of two clusters. Which is more likely to be a hadronic-like clus-  
 904 ter. Thus, cluster shape discrimination with deep learning (CSDDL), which is explained  
 905 in Section 6.3.2, is sensitive to distinguish the fusion cluster from the single cluster.

906 If we assume the BR to be  $\mathcal{O}(10^{-3})$ , the number of signal events inside the signal region  
 907 is  $\mathcal{O}(10^5)$ . That means the Kaon decay background is negligible in this study.

908 Figure 6.10 shows the background level of other  $K_L^0$  decays. The upper limit at 90%  
 909 confidence level is estimated in the signal region, as shown in Table 6.3.

### 910 6.3.2 Neutron Background

911 The in-beam neutron background is the dominant background in this study. The neutron  
 912 is generated by the hadronic interaction in the beamline, and it is called the "halo neutron"  
 913 also. The mechanism is that a neutron hits the CsI calorimeter with one cluster, and there

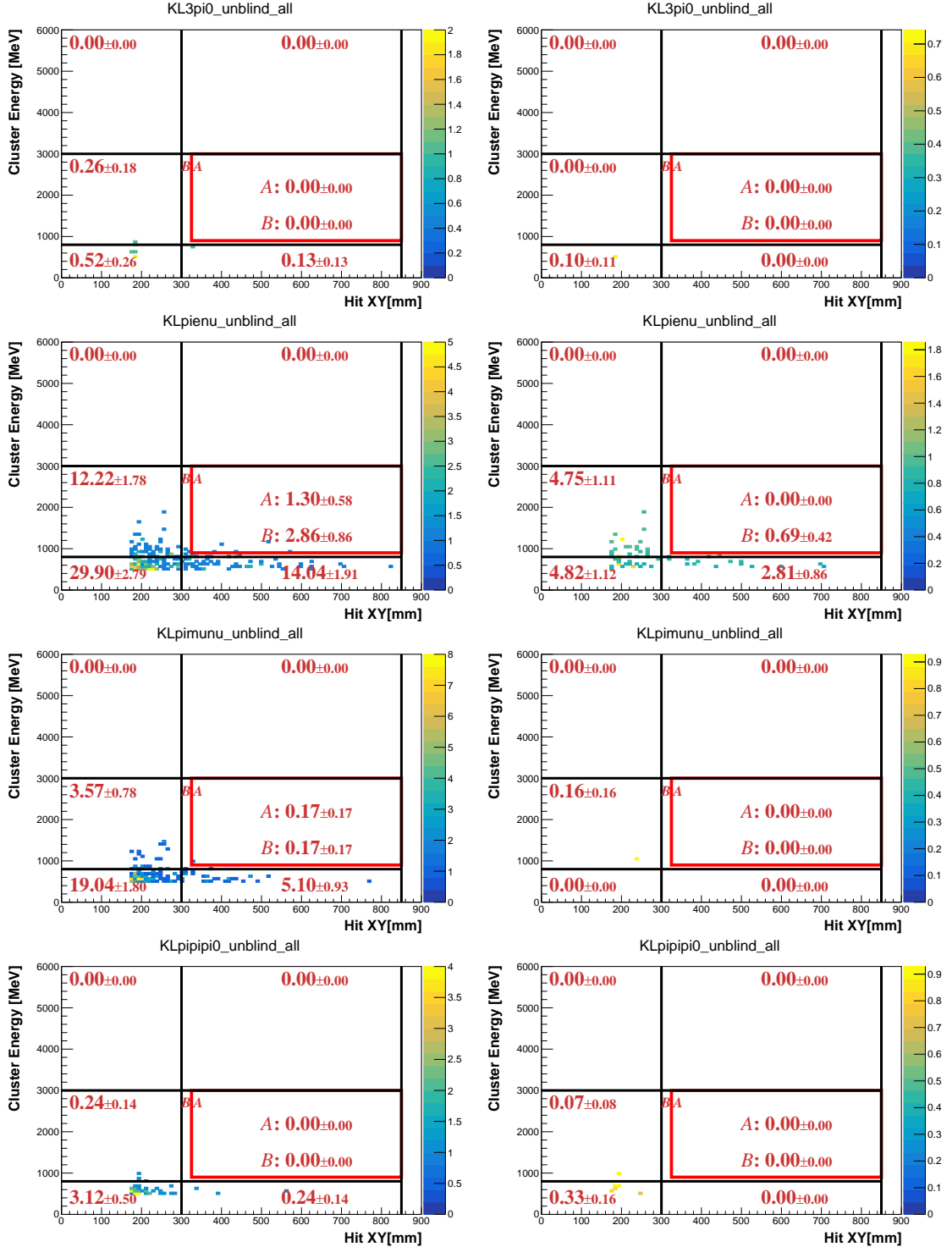


FIGURE 6.10:  $E_\gamma - H_{XY}$  distributions of various background sources after applying all selection cuts. Left-hand side plots exclude the neutron cuts and the right-hand side plots include it. The red frame indicates the signal region. The red number indicates the background level in each region. (Region A indicates the Signal Region and Region B indicates the Blind Region excluding the signal region.)

is no other in-time hit in the rest of the veto counters. Because the signature is the same as the signal event, the regular background reject method can not reduce this background, the neutron background is the most challenging in this study. Therefore, we developed three techniques based on the  $\gamma - n$  discrimination to suppress the neutron background. The first and most powerful method is to discriminate the neutron cluster by the cluster shape with deep learning. The second one is discriminating the neutron cluster by the pulse shape difference with Fourier transformation. The last one is to use the both-end readout system of CsI crystal to measure the shower depth of the cluster. These three methods are explained in the following sections.

### Cluster Shape Discrimination with Deep Learning(CSDDL)

The Cluster Shape Discrimination (CSD) method is based on the difference in the cluster shape between the neutron event and the photon event. Because of the shower depth difference, the neutron-like event will tend to be wider and shallower, and the photon-like event will be more narrow and depth, as shown in Figure 6.11. The difference is very easy to distinguish by the human eye, but it is very difficult to be quantified by the algorithm. Therefore, a neutral network model was developed to quantify the difference of the cluster shape difference.

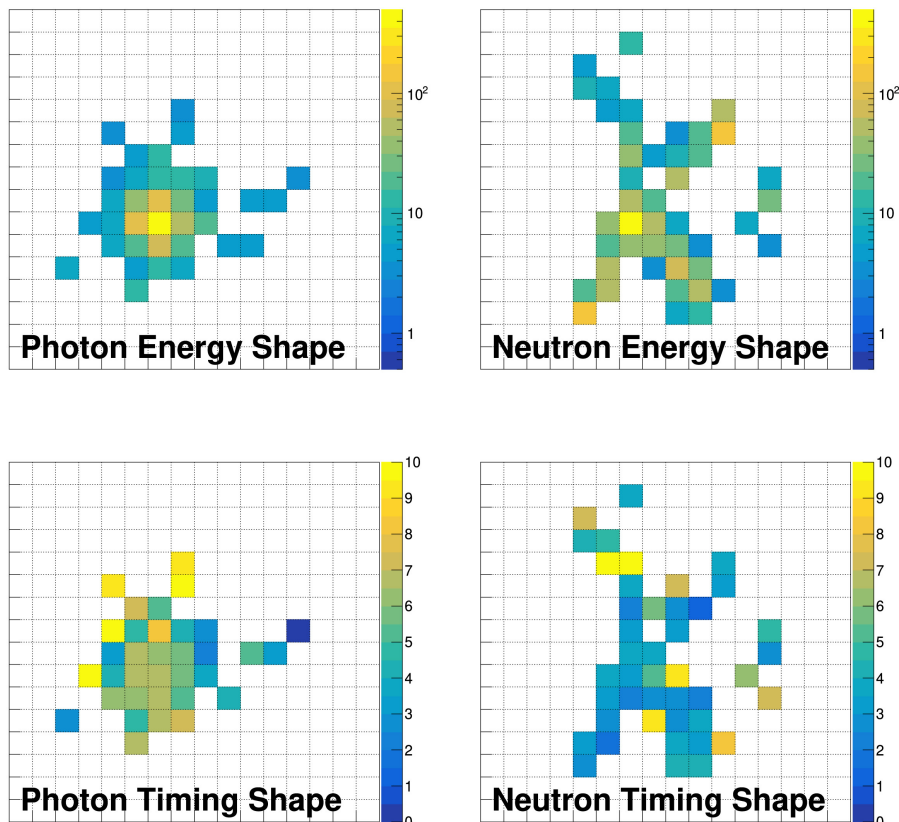


FIGURE 6.11: Example of the energy and timing shapes of photon cluster from the Monte Carlo simulation and neutron cluster from data. The color code represents the deposited energy in MeV and the timing in nanoseconds for each crystal in the cluster. [24]

In this study, the Convolutional Neural Network (CNN) architecture via TensorFlow was employed to classify the neutron and photon clusters by the energy and timing shapes [24]. We use the energy and timing for each crystal the cluster energy and the reconstructed angle on CsI ( $\phi$ ) as the input parameter of the model training. The architecture of the CNN training process is shown in Figure 6.12.

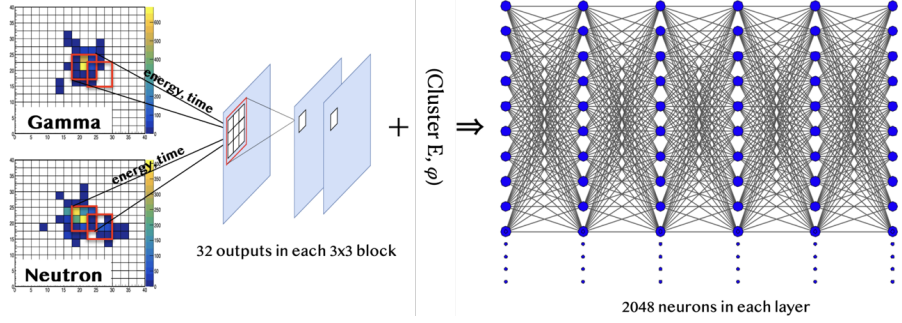


FIGURE 6.12: The architecture of CSD neural network training process.

The model was trained using a photon sample derived from Monte Carlo (MC) simulations and a neutron sample from actual experimental data. Specifically, the photon sample was sourced from the  $K_L^0 \rightarrow \gamma\bar{\gamma}$  decay MC simulation, which includes accidental overlays. The choice of MC for the photon sample is crucial, as the training process relies on the precise measurement of energy and angle of clusters on the CsI detector, which are highly dependent on the assumed decay model. Utilizing a pure photon sample from experimental data, such as the 6-cluster events from  $K_L^0 \rightarrow 3\pi^0$  decay, would risk overfitting the model to this specific decay configuration.

For the neutron sample, we used data from the Z0-Aluminum (Z0-Al) runs, discussed in Section 4.7. It is important to note that the available Z0-Al data were insufficient for both analysis and training purposes. Consequently, we opted for a pragmatic approach by using data from the last Z0-Al run, specifically RUN82 from 2019, as our training dataset. To validate the suitability of the RUN82 neutron sample, we compared it against a smaller test set of neutrons from RUN85. This comparison, depicted in Figure 6.13, demonstrated a satisfactory alignment between the test results and the training dataset.

The performance of the CSD training result is illustrated by the acceptance of photon clusters in comparison to the rejection of neutron clusters on the CSD score, as shown in Figure 6.13. This training result gives a very high neutron rejection with high photon acceptance. A selection cut point was decided at a CSDDL score larger than 0.984 based on the 90% signal acceptance. At this point, the inefficiency of the neutron sample is up to  $\mathcal{O}(-3)$

#### Fourier transforms for Pulse shape discrimination (FPSD)

The difference in shower development of neutron and photon particles also manifests in the pulse shape difference in the CsI. The neutron pulses have a longer tail than the

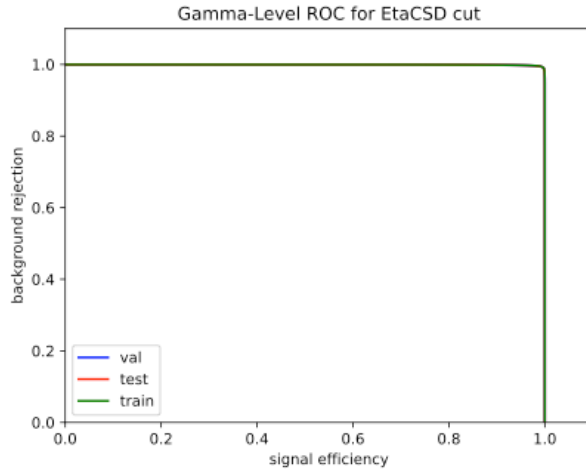


FIGURE 6.13: The ROC curve of the training model. The x-axis is the photon acceptance, and the y-axis is the neutron rejection.

960 photon sample because of the difference between the hadronic interaction and electro-  
961 magnetic interactions, as shown in Figure 6.14

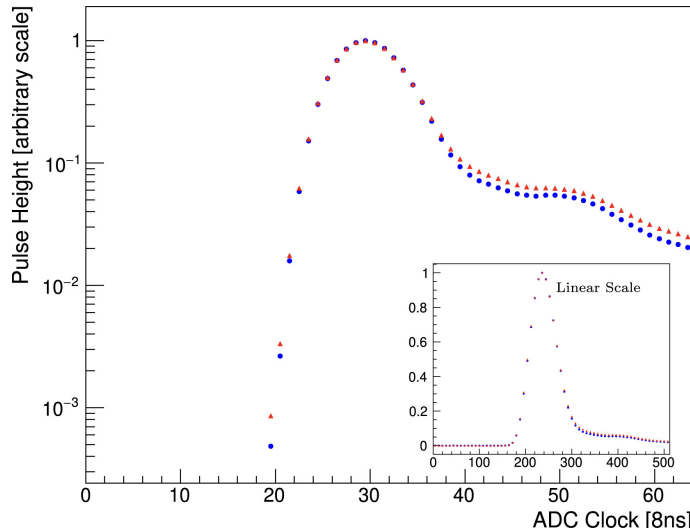


FIGURE 6.14: Average pulse shape of the neutron sample (blue dots) and photon sample (red dots) from one CsI crystal.[24]

962 The datasets for the neutron and photon samples were extracted from the data. The  
963 photon dataset is obtained from 6-cluster events, predominantly from the  $K_L^0 \rightarrow 3\pi^0$   
964 decay. The neutron sample, utilized in the CSDDL model testing, comes from the same  
965 dataset.

966 The FPSD technique is employed to differentiate between neutron and photon clusters  
967 by analyzing the shape of the ADC waveform. We applied the Discrete Fourier Trans-  
968 form (DFT) to the raw ADC pulses and subsequently identified distinguishing features  
969 between neutrons and photons in the frequency domain. Figure 6.15 illustrates the like-  
970 lihood ratio obtained from this analysis. By setting a threshold that achieves 90% signal  
971 acceptance, we attained a background rejection efficiency of 89.6% for neutron clusters.

972 It is important to highlight that the FPSD algorithm relies on the CsI pulse shape,  
973 which is not incorporated in the MC simulations. Consequently, to implement this cut

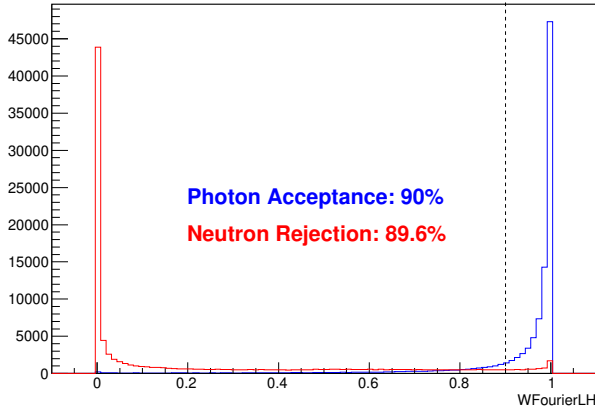


FIGURE 6.15: Distribution of the likelihood ratio for hadronic cluster events (red) and photon cluster events (blue). The photon cluster events are obtained through the  $K_L^0 \rightarrow 3\pi^0$  decay analysis of data. The neutron sample is obtained from neutron data.

within the MC simulations, we utilize a table that outlines the FPSD cut efficiency. This table is structured based on the cluster energy, its position on the CsI detector, and the specified cut value. When the FPSD is applied to an MC event, the algorithm searches for the corresponding cut efficiency in the table and applies this efficiency as a weighting factor to the event. This method ensures that the impact of the FPSD cut is accurately reflected in the simulation analysis.

### Shower-depth

The radiation length for photons is shorter than the interaction length for neutrons, resulting in different shower depths in the calorimeter for photons and neutrons. Multi-pixel photon counters (MPPC) were installed in front of the CsI calorimeter, to consist of the both-end readout system with PMT. As shown in Figure 6.16, because of the shower depth difference, the timing difference ( $\Delta T$ ) between the front-end (MPPC) and the back-end (PMT) is different for the neutron and photon events. The  $\Delta T$  (time difference) for photon events tends to be smaller than that for neutron events.

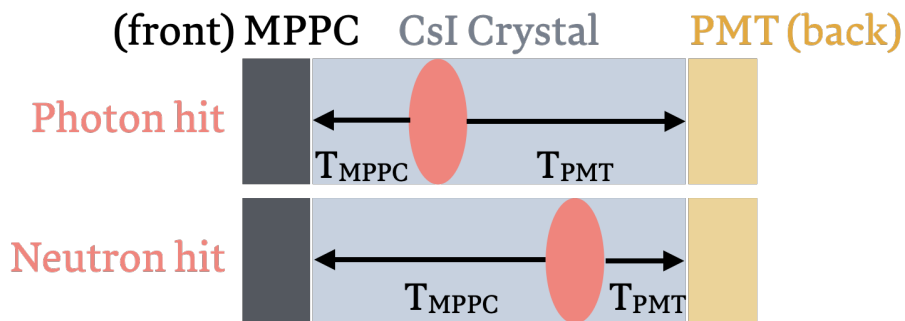


FIGURE 6.16: Illustration of shower depth means. An MPPC is installed on the upstream side. The time difference between the photon arriving upstream and downstream ( $\Delta T = T_{MPPC} - T_{PMT}$ ) is used to measure the depth of the reaction and distinguish between photon events (up) and neutron events (down).

The distribution of  $\Delta T$  is shown in figure 6.17. By requiring  $\Delta T$  to be less than 29.5 ns, the background rejection efficiency is 84% with a signal loss of 9%. The same data

described in Section 6.3.2 was used.

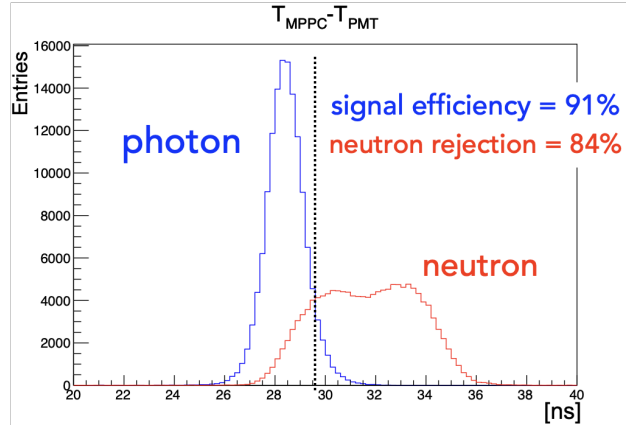


FIGURE 6.17: Distribution of the  $\Delta T$  for neutron events and photon events. The photon cluster events are obtained through the  $K_L^0 \rightarrow 3\pi^0$  decay analysis of data. The neutron sample is obtained by scattering neutrons in the beam with an Al plate.

## 6.4 Single Event Sensitivity

After considering the 175 mm cut for the low-radius background and all the selection cuts, the single event sensitivity (SES) is calculated by the equation 6.1. The SES is calculated by the  $K_L^0$  yield and the signal acceptance. For this study, The  $K_L^0$  yield is evaluated by the  $K_L^0 \rightarrow 3\pi^0$  decay, because the statistics of the 2-hour special physics data set are not enough to evaluate the yield by  $K_L^0 \rightarrow \pi^0\pi^0$  and  $K_L^0 \rightarrow 2\gamma$  decays. After the selection cuts in Section 5.2, no event will leave for the  $K_L^0 \rightarrow \pi^0\pi^0$  and  $K_L^0 \rightarrow 2\gamma$  decays. The signal acceptance is evaluated by the Monte Carlo simulation with accidental overlay. After applying all the selection cuts in Section 6.2, the signal acceptance is  $2.66 \times 10^{-3}$ . And the  $K_L^0$  yield is  $1.29 \times 10^{10}$ . The single event sensitivity (SES) is estimated to be  $(2.91 \pm 0.05_{stat.}) \times 10^{-8}$ .

$$SES = \frac{1}{Y \times A_{sig}} \quad (6.6)$$

$$= \frac{1}{1.29 \times 10^{10} \times 2.66 \times 10^{-3}} \quad (6.7)$$

$$= 2.91 \times 10^{-8} \quad (6.8)$$

### 6.4.1 Systematic Uncertainty of SES

Table 6.1 shows the summary of the systematic uncertainty from each source for the SES.

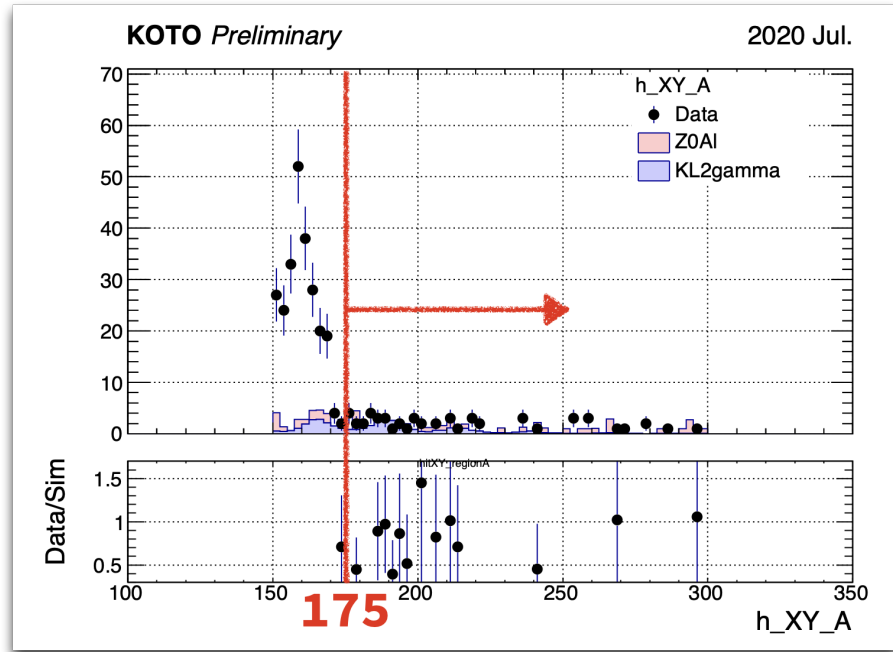
## 6.5 Additional Background Source Study

After the event selection, there is a large discrepancy between the data and the simulation in the low-radius region where  $H_{XY} < 175$  mm. As shown in Figure 6.18, the data has a

TABLE 6.1: Summary of Systematic Uncertainty for SES

Sources	Uncertainty
Veto Cuts	6.6%
Kinematic Cuts for $K_L^0 \rightarrow 3\pi^0$	3.3%
Kinematic Cuts for $K_L^0 \rightarrow \gamma\bar{\gamma}$	1.4%
Neutron Cuts for $K_L^0 \rightarrow \gamma\bar{\gamma}$	4.8%
$K_L^0$ momentum spectrum	0.9%
Trigger Effect	1.6%
Branching ratio of $K_L^0 \rightarrow 3\pi^0$	0.6%

higher level of background in the low-radius region than the simulation. To figure out the contribution of this discrepancy, we studied some extra background sources. However, all these sources cannot explain the discrepancy and are negligible, therefore they are not included in the background estimation. Anyway, in the following subsection, the description of these sources is shown.

FIGURE 6.18: The  $H_{XY}$  distribution of the region 2. The red line and arrow indicated the cutoff region

#### Very Upstream Decay from 2nd Collimator

The discrepancy is centered at the region  $H_{XY} < 175$  mm and the maximum  $H_{XY}$  of the cluster of upstream decay is 265 mm, as Section 6.3.1 discussed. This means the upstream decay is a very possible background source. Therefore, we extend the generated position in the Monte Carlo simulation to the start of the 2nd collimator to study the very upstream decay background. In the usual simulation, the decay position is generated at the end of the 2nd collimator, which is -1507 mm from the upstream of the FBAR. The

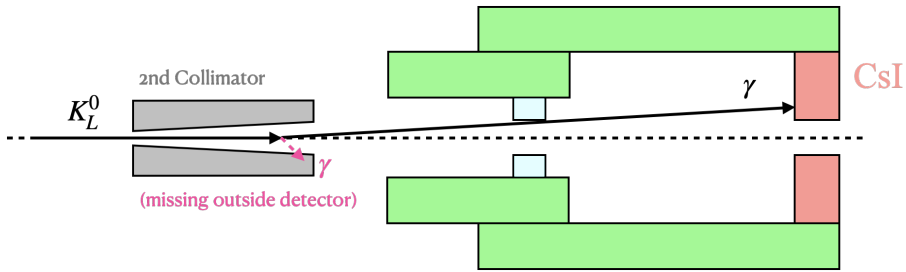


FIGURE 6.19: The schematic geometry diagram of the mechanism of the very upstream decay from the 2nd collimator.

1019 2nd collimator is 4 m long, which means the new decay position is -5507 mm from the  
 1020 upstream of the FBAR. Table 6.2 shows the result of geometry calculation in each decay  
 1021 position based on Figure 6.7. The maximum  $H_{XY}$  of the decay from the 2nd collimator is  
 1022 132.6 mm, which completely covers the discrepancy region.

TABLE 6.2: Geometry calculation of the maximum  $H_{XY}$  of the cluster of the upstream decay background

	$z_i$ [mm]	$\text{Max}(H_{XY})$ [mm]
Entrance of Detector	0	264.6
End of 2nd Collimator	-1507	191.8
Position $H_{XY} < 175$ mm	-2165	175.0
Position $H_{XY} < 150$ mm	-3680	150.0
Start of 2nd Collimator	-5507	132.6

1023 The  $K_L^0 \rightarrow 2\gamma$  and  $K_L^0 \rightarrow 3\pi^0$  decay were studied in this section. The normalization  
 1024 method is the same as the usual Monte Carlo simulation but uses the upstream  $K_L^0 \rightarrow$   
 1025  $3\pi^0$  decay ( $Z=-5507$  mm) to estimate the  $K_L^0$  yield. As shown in Figure 6.20, after all  
 1026 the selections, there is no obverse increment compared with the usual simulation decay  
 1027 position. Therefore, the very upstream decay from the 2nd collimator is not the source of  
 1028 the discrepancy.

### 1029 Upstream $\pi^0$ Background

1030 When a halo neutron hits NCC, a  $\pi^0$  might be produced by the hadronic interaction,  
 1031 this kind of background also called "NCC background". The mechanism of the NCC  
 1032 background is shown in Figure 6.21. The  $\pi^0$  will decay to two photons and if one of  
 1033 them missing due to the inefficiency of the detector, it will become a background source.  
 1034 The normalization method is borrowed from the  $K_L^0 \rightarrow \pi^0\nu\bar{\nu}$  analysis. As shown in  
 1035 Figure 6.22, we use the  $K_L^0 \rightarrow \pi^0\nu\bar{\nu}$  decay reconstruction and compare the number of  
 1036 events between data and the MC of the NCC background with the reconstructed decay  
 1037 vertex within the NCC region. And obtain the scaled factor from the ratio of the number  
 1038 of events between data and the MC. Additionally, because the special run data is not  
 1039 enough to do the  $K_L^0 \rightarrow \pi^0\nu\bar{\nu}$  reconstruction, the other run in RUN85 was utilized to do

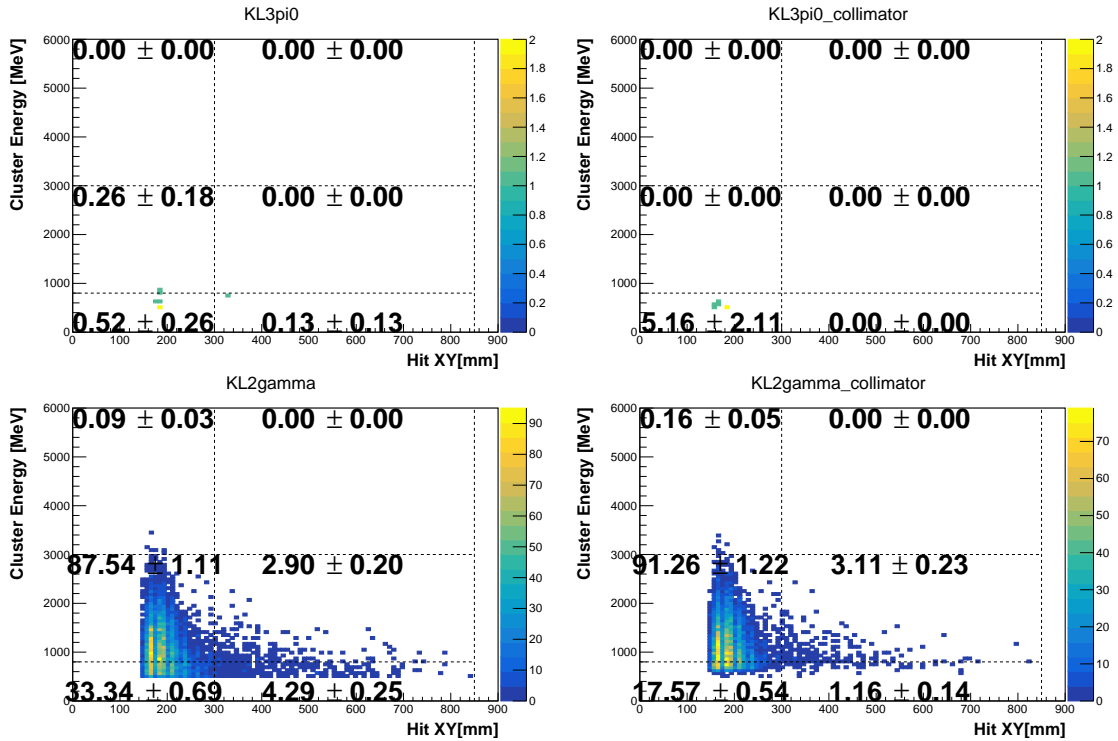


FIGURE 6.20:  $E_\gamma - H_{XY}$  distributions of  $K_L^0 \rightarrow 2\gamma$  and  $K_L^0 \rightarrow 3\pi^0$  decays after applying all selection cuts except  $H_{XY} > 175$ . Left-hand side plots decay at  $z=-1507$  mm and the right-hand side plots decay at  $z=-5507$  mm.

1040 the normalization. Then use the POT ratio between the special run and the other run to  
1041 scale the number of events in the special run.

1042 The result of the NCC background estimation is shown in Figure 6.23. As shown in  
1043 the figure, the NCC background is negligible in the single cluster analysis.

#### 1044 Charge Kaon Decay

1045 As shown in Figure 4.1, though it is not a large amount, the charge Kaon remains in  
1046 the beamline. A beamline simulation seed was used in the Monte Carlo simulation to  
1047 simulate all the charge Kaon decay. The normalization method simply used the POT

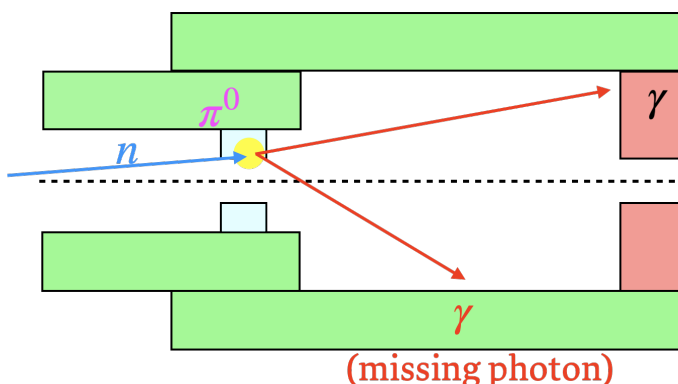


FIGURE 6.21: A schematic diagram of the mechanism of the NCC background.

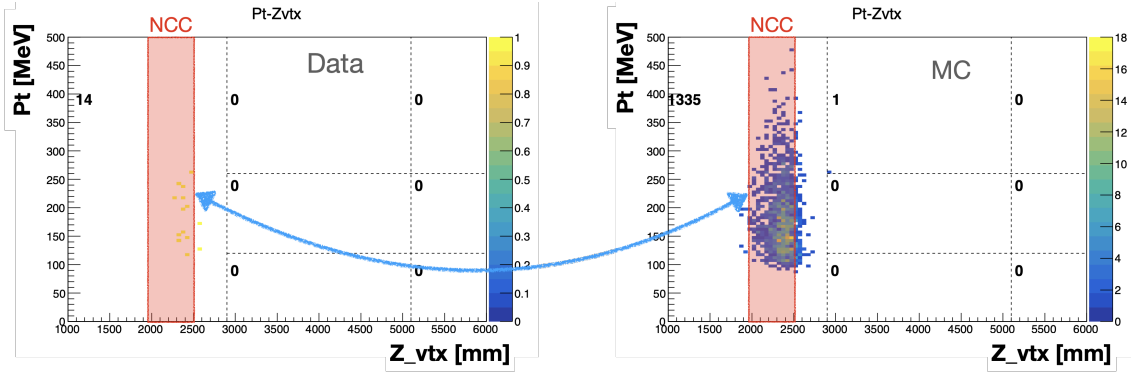


FIGURE 6.22:  $P_T - z_{vtx}$  distribution of the NCC background with  $K_L^0 \rightarrow \pi^0 \nu \bar{\nu}$  reconstruction. The left plot is from the data the right plot is the MC of the NCC background. The red frame indicates the NCC region.

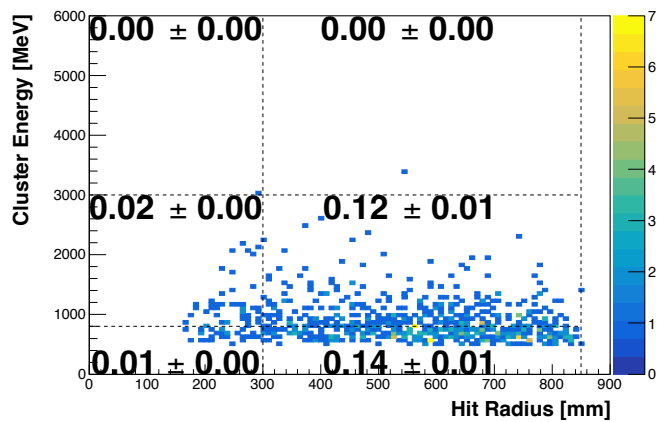


FIGURE 6.23:  $E_\gamma - H_{XY}$  distribution of the NCC background after applying all selection cuts.

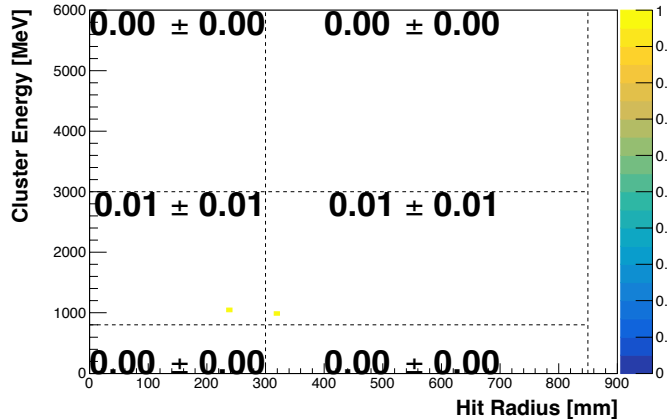


FIGURE 6.24:  $E_\gamma - H_{XY}$  distribution of the charge Kaon decay after applying all selection cuts.

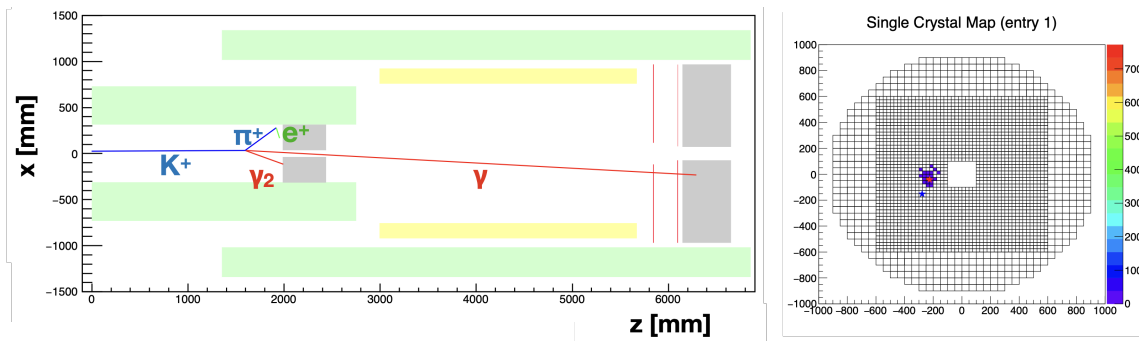


FIGURE 6.25: Event display of the charge Kaon decay.

ratio between the data and the MC. The result of the charge Kaon decay is shown in Figure 6.24. Obviously, the charge Kaon decay is negligible in this study.

### 1050 Halo $K_L^0$ Background

1051 Halo  $K_L^0$  is the  $K_L^0$  particles that are in the periphery of the beam core. As mentioned in  
 1052 Section 4.4.2, the empirical  $K_L^0$  spectrum does not consider the halo  $K_L^0$ . The beamline  
 1053 simulation was required to simulate the halo  $K_L^0$ . However, currently, we don't have the  
 1054 suitable method to normalize the halo  $K_L^0$ .

### 1055 Summary of the Study

1056 After the above extra background source study, the discrepancy in the low radius region  
 1057 still exists. Currently, there are no further ideas for the search strategy. It is also possible  
 1058 that just from upstream accidentally hit which is almost impossible to prob because the  
 1059 sources are unknown and unclear. To handle is problem, we simply enlarge the inner-  
 1060 most fiducial cut from 150 mm to 175 mm.

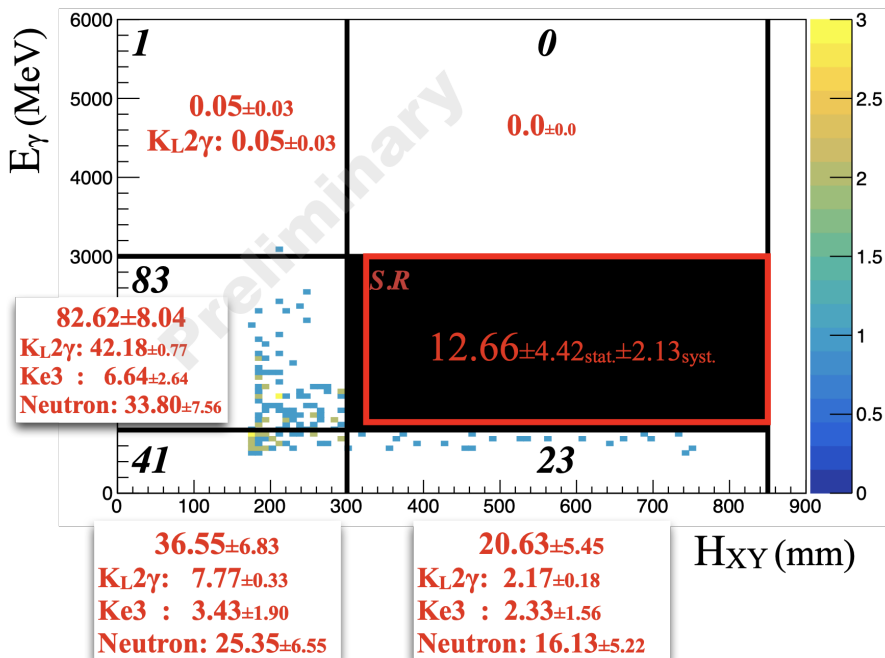
## 1061 6.6 Background Level Estimation

1062 Table 6.3 shows the background level of each background source in the signal region. The  
 1063 upper limit at 90% confidence level is estimated in the signal region.

TABLE 6.3: Background Level predicted for each source inside the signal region

Type	Source	Background Level
$K_L$ decay	$K_L \rightarrow 2\gamma$	$1.09 \pm 0.12$
	$K_L \rightarrow 3\pi^0$	$< 0.18$ (90% C.L.)
	$K_L \rightarrow 2\pi^0$	$< 0.51$ (90% C.L.)
	$K_L \rightarrow \pi^\pm e^\mp \nu_e$	$< 0.27$ (90% C.L.)
	$K_L \rightarrow \pi^\pm \mu^\mp \nu_\mu$	$< 0.25$ (90% C.L.)
	$K_L \rightarrow \pi^+ \pi^- \pi^0$	$< 0.17$ (90% C.L.)
Neutron		$11.57 \pm 4.42$
Total (exclude sources without central value)		$12.66 \pm 4.42$

1064      Figure 6.26 shows the  $E_\gamma$ -  $H_{XY}$  distribution of physics data for each region. In the  
 1065      side-band region, the expected number shows agreement with the observations. The  
 1066      background level in the signal region is  $12.66 \pm 4.42$ .

FIGURE 6.26:  $E_\gamma$ -  $H_{XY}$  distribution of physics data after applying all the selection cuts. The black box is the blind region the red frame is the signal region. The black (red) number is the observed (expected) number of events.

## 1067 6.7 Unbind the Signal Region

1068      After all the studies, we decided to open the box. The observed result is 13 events inside  
 1069      the signal region, as shown in Figure 6.27, which agrees with the expected number of  
 1070      events. To estimate the Branching ratio of the  $K_L^0 \rightarrow \gamma\bar{\gamma}$ , the Feldman-Cousins method  
 1071      was adopted, because we still have numerous expected backgrounds in the signal region.

<sup>1072</sup> After the calculation, an upper limit of branching ratio was obtained at 90% C.L.,

$$\mathcal{BR}(K_L^0 \rightarrow \gamma\bar{\gamma}) < 11.9 \times SES(K_L^0 \rightarrow \gamma\bar{\gamma}) \quad (6.9)$$

$$= 3.47 \times 10^{-7} (90\% \text{ C.L.}) \quad (6.10)$$

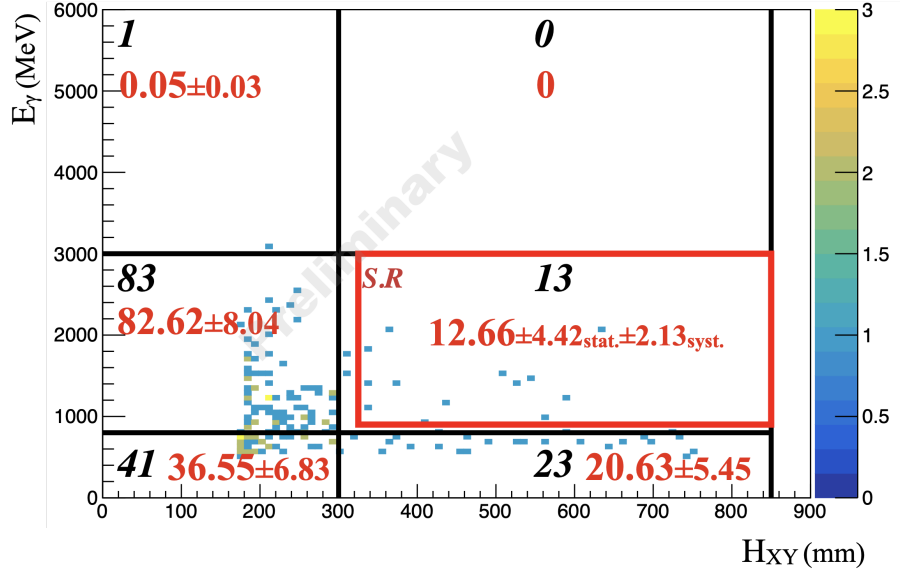


FIGURE 6.27:  $E_\gamma$ -  $H_{XY}$  distribution of physics data after open the blind box. The black (red) number is the observed (expected) number of events.



<sup>1073</sup> **Chapter 7**

<sup>1074</sup> **Conclusion and Discussion**

<sup>1075</sup> We present the study of  $K_L^0 \rightarrow \gamma\bar{\gamma}$  search in this thesis. The  $K_L^0 \rightarrow \gamma\bar{\gamma}$  analysis is based  
<sup>1076</sup> on the 2-hour spacial run taken in 2020. The total number of  $K_L^0$  decays is  $1.29 \times 10^{10}$ ,  
<sup>1077</sup> which is estimated by the  $K_L^0 \rightarrow 3\pi^0$  decay. Two kinds of backgrounds are major in  
<sup>1078</sup> this analysis, the  $K_L^0$  decay background and the in-beam neutron background. We use  
<sup>1079</sup> different methods to suppress these two backgrounds.

<sup>1080</sup> To suppress the  $K_L^0$  decay source background, we use the veto system of the KOTO  
<sup>1081</sup> detector. Because the one cluster signal signature is a pretty strict criterion to reject most  
<sup>1082</sup> of the  $K_L^0$  decay channel with multiple products in the final state. The only background  
<sup>1083</sup> that can pass the veto system is the  $K_L^0 \rightarrow 2\gamma$  channel. With one photon missing due to  
<sup>1084</sup> detection inefficiency, the  $K_L^0 \rightarrow 2\gamma$  background cannot be rejected. Thanks to the her-  
<sup>1085</sup> metric veto system of the KOTO Experiment, the  $K_L^0 \rightarrow 2\gamma$  background is well suppressed  
<sup>1086</sup> by the veto system with only  $1.09 \pm 0.12_{stat.} \pm 0.05_{syst.}$  events estimated remaining in the  
<sup>1087</sup> signal region.

<sup>1088</sup> To suppress the in-beam neutron background, we use three techniques based on the  
<sup>1089</sup>  $n - \gamma$  discrimination to suppress the neutron background. The first one is cluster shape  
<sup>1090</sup> discrimination based on deep learning, which is the most powerful technique to classify  
<sup>1091</sup> neutrons and photons. The other two are the pulse shape discrimination based on the  
<sup>1092</sup> Fourier Transform and the show-depth measure by the CsI both-end readout system.  
<sup>1093</sup> These two techniques also provide a good rejection power on the neutron background.  
<sup>1094</sup> Combining these three techniques, rejected the neutron background by  $\mathcal{O}(10^{-3})$  for the  
<sup>1095</sup> single cluster with 83.9% signal acceptance. After all the selections, the total neutron  
<sup>1096</sup> background is estimated to be  $11.57 \pm 4.42_{stat.} \pm 2.13_{syst.}$  events in the signal region.

<sup>1097</sup> Combining all the background sources we have studied, the total background is esti-  
<sup>1098</sup> mated to be  $12.66 \pm 4.42_{stat.} \pm 2.13_{syst.}$  events in the signal region. After the background  
<sup>1099</sup> suppression study, we open the blind region box. The observed events in the signal re-  
<sup>1100</sup> gion are 13 events, which is consistent with the background estimation. Because we still  
<sup>1101</sup> have a large estimation of the background in the signal region, we decided to use the  
<sup>1102</sup> Feldman-Cousins method to evaluate the upper limit on the  $K_L^0 \rightarrow \gamma\bar{\gamma}$  branching ratio.  
<sup>1103</sup> At 90% C.L., the upper limit on the  $K_L^0 \rightarrow \gamma\bar{\gamma}$  branching ratio is  $3.47 \times 10^{-7}$ .

## 1104 7.1 Discussion for Next Step

1105 To advance the  $K_L^0 \rightarrow \gamma\bar{\gamma}$  search, the next crucial step is to enhance the sensitivity of  
 1106 the analysis. Given the large number of background events within the signal region,  
 1107 collecting more physics data is not an immediate priority. In the current study, the pri-  
 1108 mary background source is beam neutrons. Despite employing three techniques to sup-  
 1109 press this background, the neutron background remains significantly estimated in the  
 1110 signal region. Thus, increasing the effectiveness of neutron background suppression is  
 1111 paramount. Additionally, enhancing the statistical power of the analysis is vital. At  
 1112 present, the neutron background estimation is plagued by considerable statistical uncer-  
 1113 tainty.

1114 For the next step, I suggest utilizing previously collected data to enhance the statistics.  
 1115 Since we do not use or need the single-cluster Z0-Al data in the analysis, we can repur-  
 1116 pose the data we have already collected. Specifically, data taken before the 2020 RUN85,  
 1117 which includes both physics and Z0-Al data, can be utilized. For single-cluster physics  
 1118 data, we can use the normalization trigger in the physics data, which does not filter based  
 1119 on the number of clusters. For Z0-Al data, we can continue using the two-cluster Z0-Al  
 1120 data, consistent with our current strategy.

## 1121 7.2 Massive Dark Photon Search

1122 We finished the massless dark photon study, the massive dark photon should be also an  
 1123 interesting topic to study. In this study, the search strategy is not strict with the mass of  
 1124 the dark photon. Therefore, the massive dark photon search will use the same strategy as  
 1125 the massless dark photon search. The only need to change is the mass of the dark photon  
 1126 in the MC simulation. Figure 7.1 shows the Upper limit and signal acceptance of each  
 1127 mass of the dark photon.

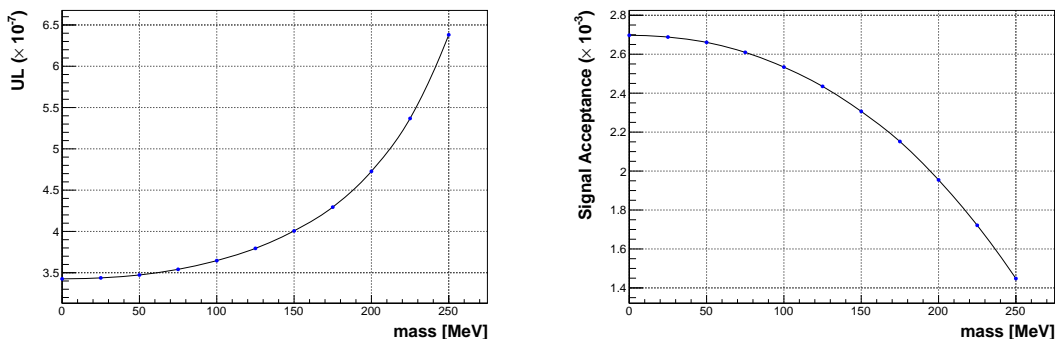


FIGURE 7.1: Upper limit (left) and signal acceptance (right) for each mass dark photon from 0 MeV to 250 MeV, step 25 MeV

# 1128 Bibliography

- 1129 [1] Particle Data Group et al. "Review of Particle Physics". In: *Progress of Theoretical*  
 1130 *and Experimental Physics* 2022.8 (Aug. 2022), p. 083C01. ISSN: 2050-3911. DOI: [10.1093/ptep/ptac097](https://doi.org/10.1093/ptep/ptac097).
- 1132 [2] Marco Fabbrichesi, Emidio Gabrielli, and Gaia Lanfranchi. *The Physics of the Dark*  
 1133 *Photon: A Primer*. Springer International Publishing, 2021. ISBN: 9783030625191.  
 1134 DOI: [10.1007/978-3-030-62519-1](https://doi.org/10.1007/978-3-030-62519-1).
- 1135 [3] Jhih-Ying Su and Jusak Tandean. "Kaon decays shedding light on massless dark  
 1136 photons". In: *The European Physical Journal C* 80.9 (2020), p. 824. DOI: [10.1140/epjc/s10052-020-8338-3](https://doi.org/10.1140/epjc/s10052-020-8338-3).
- 1138 [4] Andrzej J. Buras et al. " $K^+ \rightarrow \pi^+ \nu \bar{\nu}$  and  $K_L \rightarrow \pi^0 \nu \bar{\nu}$  in the Standard Model: status  
 1139 and perspectives". In: *Journal of High Energy Physics* 2015.11 (2015). DOI: [10.1007/jhep11\(2015\)033](https://doi.org/10.1007/jhep11(2015)033).
- 1141 [5] Shoji Nagamiya. "Introduction to J-PARC". In: *Progress of Theoretical and Experi-  
 1142 mental Physics* 2012.1 (Oct. 2012). 02B001. ISSN: 2050-3911. DOI: [10.1093/ptep/pts025](https://doi.org/10.1093/ptep/pts025).
- 1144 [6] Masanori Ikegami. "Beam commissioning and operation of the J-PARC linac". In:  
 1145 *Progress of Theoretical and Experimental Physics* 2012.1 (Sept. 2012). 02B002. ISSN:  
 1146 2050-3911. DOI: [10.1093/ptep/pts019](https://doi.org/10.1093/ptep/pts019).
- 1147 [7] Hideaki Hotchi et al. "Beam commissioning and operation of the Japan Proton Ac-  
 1148 celerator Research Complex 3-GeV rapid cycling synchrotron". In: *Progress of The-  
 1149 oretical and Experimental Physics* 2012.1 (Sept. 2012). 02B003. ISSN: 2050-3911. DOI:  
 1150 [10.1093/ptep/pts021](https://doi.org/10.1093/ptep/pts021).
- 1151 [8] Tadashi Koseki et al. "Beam commissioning and operation of the J-PARC main ring  
 1152 synchrotron". In: *Progress of Theoretical and Experimental Physics* 2012.1 (Dec. 2012).  
 1153 02B004. ISSN: 2050-3911. DOI: [10.1093/ptep/pts071](https://doi.org/10.1093/ptep/pts071).
- 1154 [9] Shunzo Kumano. "J-PARC Hadron Physics and Future Possibilities on Color Trans-  
 1155 parency". In: *Physics* 4 (May 2022), pp. 565–577. DOI: [10.3390/physics4020037](https://doi.org/10.3390/physics4020037).
- 1156 [10] K. Takahashi H.and Agari et al. "Indirectly water-cooled production target at J-  
 1157 PARC hadron facility". In: *Journal of Radioanalytical and Nuclear Chemistry* 305.3  
 1158 (2015), pp. 803–809. ISSN: 1588-2780. DOI: [10.1007/s10967-015-3940-9](https://doi.org/10.1007/s10967-015-3940-9).
- 1159 [11] T. Shimogawa. "Design of the neutral K0L beamline for the KOTO experiment". In:  
 1160 *Nuclear Instruments and Methods in Physics Research Section A: Accelerators, Spectrome-  
 1161 ters, Detectors and Associated Equipment* 623.1 (2010). 1st International Conference on  
 1162 Technology and Instrumentation in Particle Physics, pp. 585–587. ISSN: 0168-9002.  
 1163 DOI: <https://doi.org/10.1016/j.nima.2010.03.078>.

- 1164 [12] D. Naito et al. "Development of a low-mass and high-efficiency charged-particle  
 1165 detector". In: *Progress of Theoretical and Experimental Physics* 2016.2 (Feb. 2016). 023C01.  
 1166 ISSN: 2050-3911. DOI: [10.1093/ptep/ptv191](https://doi.org/10.1093/ptep/ptv191).
- 1167 [13] Yosuke Maeda. *Charged-particle veto detector for the  $K_L \rightarrow \pi^0\nu\bar{\nu}$  study in the J-PARC  
 1168  $K^0$ TO experiment.* 2012.
- 1169 [14] Daichi Naito et al. "Evaluation of the Inefficiency of a Charged Particle Detector  
 1170 for the KOTO Experiment". In: *JPS Conf. Proc.* 8 (2015), p. 024003. DOI: [10.7566/JPSCP.8.024003](https://doi.org/10.7566/JPSCP.8.024003).
- 1172 [15] C. Lin. "Study of  $K_L^0 \rightarrow \pi^0\nu\bar{\nu}$  and  $K_L^0 \rightarrow \pi^0\gamma\gamma$  with the Cluster-Finding Trigger at  
 1173 KOTO". National Taiwan University, 2021. DOI: [10.6342/NTU202102308](https://doi.org/10.6342/NTU202102308).
- 1174 [16] Chieh Lin. "Data-Acquisition System Upgrade for the KOTO Experiment". In: *PoS  
 1175 ICHEP2022* (2022), p. 242. DOI: [10.22323/1.414.0242](https://doi.org/10.22323/1.414.0242).
- 1176 [17] E. Iwai et al. "Performance study of a prototype pure CsI calorimeter for the KOTO  
 1177 experiment". In: *Nuclear Instruments and Methods in Physics Research Section A: Ac-  
 1178 celerators, Spectrometers, Detectors and Associated Equipment* 786 (2015), pp. 135–141.  
 1179 ISSN: 0168-9002. DOI: <https://doi.org/10.1016/j.nima.2015.02.046>.
- 1180 [18] J. Allison et al. "Geant4 developments and applications". In: *IEEE Transactions on  
 1181 Nuclear Science* 53.1 (2006), pp. 270–278. DOI: [10.1109/TNS.2006.869826](https://doi.org/10.1109/TNS.2006.869826).
- 1182 [19] S. Agostinelli et al. "Geant4—a simulation toolkit". In: *Nuclear Instruments and Meth-  
 1183 ods in Physics Research Section A: Accelerators, Spectrometers, Detectors and Associated  
 1184 Equipment* 506.3 (2003), pp. 250–303. ISSN: 0168-9002. DOI: [https://doi.org/10.1016/S0168-9002\(03\)01368-8](https://doi.org/10.1016/S0168-9002(03)01368-8).
- 1186 [20] J. Allison et al. "Recent developments in Geant4". In: *Nuclear Instruments and Meth-  
 1187 ods in Physics Research Section A: Accelerators, Spectrometers, Detectors and Associated  
 1188 Equipment* 835 (2016), pp. 186–225. ISSN: 0168-9002. DOI: <https://doi.org/10.1016/j.nima.2016.06.125>.
- 1190 [21] Kazufumi Sato. "Measurement of the CsI calorimeter performance and KL momen-  
 1191 tum spectrum for the J-PARC KOTO experiment". Ph.D. thesis. Osaka University,  
 1192 2015.
- 1193 [22] Particle Data Group et al. "Review of Particle Physics". In: *Progress of Theoretical and  
 1194 Experimental Physics* 2020.8 (Aug. 2020). 083C01. ISSN: 2050-3911. DOI: [10.1093/ptep/ptaa104](https://doi.org/10.1093/ptep/ptaa104).
- 1196 [23] Kota Nakagiri. "Search for the Decay  $K_L^0 \rightarrow \pi^0\nu\bar{\nu}$  at the J-PARC KOTO Experi-  
 1197 ment". Ph.D. thesis. Kyoto University, 2019. DOI: [10.14989/doctor.k21564](https://doi.org/10.14989/doctor.k21564).
- 1198 [24] Y. C. Tung et al. "Suppression of neutron background using deep neural network  
 1199 and Fourier frequency analysis at the KOTO experiment". In: *Nucl. Instrum. Meth.  
 1200 A* 1059 (2024), p. 169010. DOI: [10.1016/j.nima.2023.169010](https://doi.org/10.1016/j.nima.2023.169010).